2011

# Evanescent wave assist features for optical projection lithography

Neal Lafferty

# EVANESCENT WAVE ASSIST FEATURES FOR OPTICAL PROJECTION LITHOGRAPHY

by

NEAL VINCENT LAFFERTY

A DISSERTATION

Submitted in partial fulfillment of the requirements
for the degree of Doctor of Philosophy
in
Microsystems Engineering
at the
Rochester Institute of Technology

June 2011

Author: _____
Microsystems Engineering Program

Certified by: _____
Prof. Bruce W. Smith, Ph.D.
Director of Microsystems Engineering Program

Approved by: _____
Prof. Bruce W. Smith, Ph.D.
Director of Microsystems Engineering Program

Certified by: _____
Harvey J. Palmer, Ph.D.
Dean, Kate Gleason College of Engineering

# NOTICE OF COPYRIGHT



**REPRODUCTION PERMISSION STATEMENT**

Permission Granted

**TITLE:**

**"EVANESCENT WAVE ASSIST FEATURES FOR OPTICAL PROJECTION LITHOGRAPHY"**

I, Neal V. Lafferty, hereby grant permission to the Wallace Library of the Rochester Institute of Technology to reproduce my dissertation in whole of in part. Any reproduction will not be for commercial use or profit.

Signature of Author:_____ Date: _____

# Evanescent Wave Assist Features for Optical Projection Lithography

by

Neal V. Lafferty

Submitted by Neal V. Lafferty in partial fulfillment of the requirements for the degree of Doctor of Philosophy in Microsystems Engineering and accepted on behalf of the Rochester Institute of Technology by the dissertation committee.

We, the undersigned members of the Faculty of the Rochester Institute of Technology, certify that we have advised and/or supervised the candidate on the work described in this dissertation. We further certify that we have reviewed the dissertation manuscript and approve it in partial fulfillment of the requirements of the degree of Doctor of Philosophy in Microsystems Engineering.

**Approved by:**

Dr. Bruce W. Smith _____
(Committee Chair and Dissertation Advisor) Date

Dr. Thomas G. Brown _____
Date

Dr. Karl D. Hirschman _____
Date

Dr. Zhaolin Lu _____
Date

MICROSYSTEMS ENGINEERING PROGRAM
ROCHESTER INSTITUTE OF TECHNOLOGY

June 2011

# ABSTRACT

Kate Gleason College of Engineering
Rochester Institute of Technology

**Degree:** Doctor of Philosophy **Program:** Microsystems Engineering

Name of Candidate: Neal V. Lafferty

Title: Evanescent Wave Assist Features for Optical Projection Lithography

Evanescent Wave Assist Features (EWAFs) are features that are sensitive to near-field radiation that modify diffracted order intensities from photomask patterns. In implementations studied in this thesis, the EWAFs increase a transmitting feature's image contrast and Normalized Image Log Slope (NILS). In this way, the EWAFs are a way to improve image fidelity for high-resolution features. The assist features consist of local, buried grooves located around transmitting mask regions. These grooves reside in otherwise unused areas, since they are located under or on top of opaque mask absorber regions. In these "buried" locations, they are not optically visible to the lithographic system in a traditional sense. Designs are explored for both top-surface and bottom-surface EWAFs on 1-D and 2-D layouts. Using EWAFs, 27% image contrast improvements have been shown on contact layouts, as well as best-case image contrast improvements of over 2X on 1-D slot-type mask layouts. Dependence of EWAF effect on mask absorber material and bottom-surface relief shape is studied, as well as polarization sensitivity and the role of Surface Plasmon Polaritons (SPP). TM polarized light creates a normal-component field enhancement that amplifies surface waves across suitably conductive absorbers. These waves can then interact with bottom-surface EWAF grooves, and convert to propagating based on grating action. The converted orders may then interact with standard transmitted orders from a transmission feature, resulting in enhancement or suppression, depending on EWAF tone, pitch regime, and illumination angle. A demonstration EWAF sample, as well as a reference sample with no grooves, was fabricated at the RIT SMFL and tested using a Variable Angle Spectroscopic Ellipsometer (VASE). Accounting for pitch deviations during fabrication, as well as lateral inter-layer alignment offsets gives diffracted order responses that agree with SPP resonances observed in the samples at normal incidence and diffracted order enhancement factors that agree with simulation.

Abstract Approval: Committee Chair: _____

Program Director: _____

Dean, KGCOE: _____

*This thesis is dedicated to my mother*
*and father, Jane and Charles Lafferty.*
*Thank you for your love and support.*

## ACKNOWLDEDGMENTS

This thesis is the product of many years of work and has been influence by a number of people. I would like to acknowledge them here.

My advisor and mentor, Professor Bruce Smith deserves many thanks. I feel very fortunate to have been a member of his nanolithography research group. I have been given many immensely rewarding opportunities during my time at RIT, and I will be forever grateful to Dr. Smith. I would also like to thank my committee members for their guidance throughout the duration of this thesis, Professors Brown, Hirschman, and Lu.

Over the years, I have worked alongside a number of talented lithography group members. I learned so much from Anatoly Bourov, Lena Zavyalova, and Yongfa Fan. Jianming Zhou and Peng Xie were great listeners and advisors. It was a pleasure to work and share cubicle space (and coffee) with Andrew Estroff, Germain Fenger, Monica Sears, Burak Baylav, and Steve Smith. Beyond the support of each other's work, I value their friendship.

Jennifer Kerr has been one of my greatest sources of encouragement and an excellent sounding board during my most difficult and complicated problems. Throughout these years she has reminded me that there is more to life than work. Due to her excellent listening skills, she is now well versed in lithography. I cannot possibly thank her enough for her love and patience.

I will be forever grateful to my parents and sister for a lifetime of love and support. I sincerely appreciated them as a source of encouragement during my studies.

This research was supported through the Semiconductor Research Corporation (SRC) via Research Ids 1083 (Immersion Optical Lithography) and 1459 (Evanescent Wave and Solid Immersion Lithography for sub-32 nm Imaging).

## TABLE OF CONTENTS

## LIST OF FIGURES

## LIST OF TABLES

## LIST OF ACRONYMS

APM.....Ammonia/Peroxide Mix

APSM.....Attenuated Phase Shift Mask

BARC.....Bottom Anti-Reflective Coating

BW .....Bloch Wave

CD .....Critical Dimension

CDEW.....Composite Diffracted Evanescent Wave

CTF .....Coherent Transfer Function

DoE .....Degree of Enhancement

DI .....De-Ionized [Water]

DRAM.....Dynamic Random Access Memory

EL.....Exposure Latitude

EWAF .....Evanescent Wave Assist Features

FDTD .....Finite-Difference Time-Domain

FTIR.....Frustrated Total Internal Reflection

HPM.....Hydrochloric acid/Peroxide Mix

IC.....Integrated Circuit

ILS.....Image Log Slope

ITRS.....International Technology Roadmap for Semiconductors

MPU.....MicroProcessor Unit

NA.....Numerical Aperture

NILS.....Normalized Image Log Slope

OPC.....Optical Proximity Correction

OTF.....Optical Transfer Function

PGMEA.....Propylene Glycol Monomethyl Ether Acetate

PML .....Perfectly Matched Layer

POI .....Plane of Incidence

RCWA.....Rigorous Coupled Waveguide Analysis

RET.....Resolution Enhancement Techniques

RF.....Radio Frequency

RIE .....Reactive Ion Etching

RPM .....Revolutions per Minute

SEM .....Scanning Electron Microscope

SPP.....Surface Plasmon Polariton

TE.....Transverse Electric (s polarized)

TIR .....Total Internal Reflection

TM.....Transverse Magnetic (p polarized)

UV.....Ultra-Violet

VASE .....Variable Angle Spectroscopic Ellipsometer

# I. INTRODUCTION

Integrated circuits (ICs) are found in nearly all modern electronics. They are responsible for reducing the cost of electronics while increasing their reliability. The result is affordable computers and other electronic devices. The IC has undergone several evolutionary changes since its inception in 1959, when it was invented at Texas Instruments by Jack Kilby [1]. The original IC was fabricated on a germanium substrate and consisted of five components. It was not a planar architecture however, as is standard today. Robert Noyce further evolved state of the art by fabricating ICs on silicon. Using naturally forming $SiO_2$, he was able to give transistors a planar architecture and connect devices with evaporated aluminum [2]. These early devices used only a handful of transistors and other basic electronic components to perform simple operations, but they planted the seeds for the industry today.

In 1964, based on his observations of the early semiconductor industry, Gordon Moore predicted that the number of transistors that could be placed inexpensively on an IC would double every two years [3]. This became known as "Moore's Law", and the industry has used it ever since in order to drive the pace of the IC's evolution. This trend is illustrated in Figure I.1. For example, the first Intel 4004 processor contained 2300 transistors on a 12 $mm^2$ area. The Intel Pentium 4 Processor has 55 million transistors covering an area of 145 $mm^2$. Circuit density has increased 2000 times compared to that of the 4004 processor. Optical lithography is the tool of choice for patterning these ever-shrinking microelectronic devices because of its low cost, historic scaling capability, and high throughput [4].

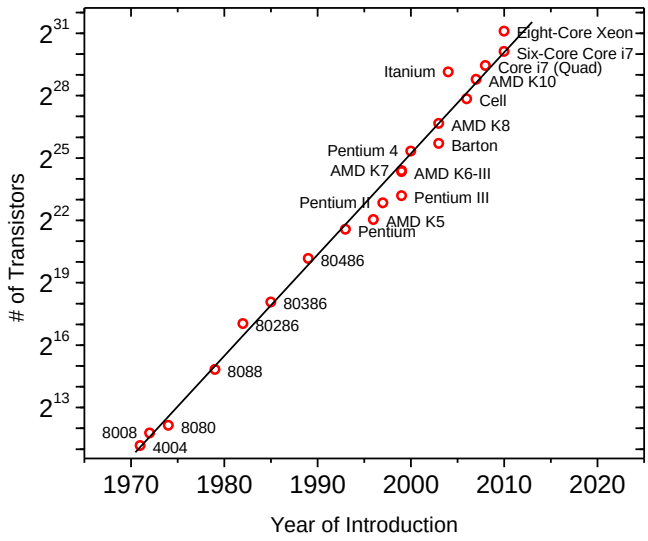


**Figure I.1: The number of transistors in selected processors vs. production year [5].**

Because of the tight schedule imposed by Moore's Law, semiconductor devices are often patterned at or near the resolution limit of current generation optical lithography tools and processes. These limits are constantly being challenged, as industry roadmaps are refined to require smaller device geometries and higher packing densities.

Lithography itself has undergone evolutionary changes as the number of transistors has scaled. In early years, from 1970-1980, the dominant pattern transfer technique was contact or proximity printing [6]. These printers exposed a unity magnification photomask that contained all die in a single wafer layout. The entire wafer was exposed at once. As CD shrank further, these systems became challenged by the presence of an unavoidable gap between the photomask and wafer. The imaging resolution scales with this gap as:

$$w \approx 0.7\sqrt{\lambda s} \tag{1.1}$$

where $w$ is the resolvable space width, $\lambda$ is the illumination wavelength, and $s$ is the separation distance [7]. Because of the square root dependence on separation distance, and the difficulty in controlling the gap, it is difficult in practice to resolve patterns past 5 μm CD over topography (using a 365 nm filtered source). Alignment at these gaps is also very difficult due to inevitable shifts between wafer and mask that occur during exposure contact. There is also an issue of defects being exposed on the wafer; since the photomask is in contact with the resist-coated wafer it is hard to control debris. From 1980 through 1990, unity magnification steppers were used for pattern transfer [6]. In these systems, an entire wafer's mask was scanned over the entire wafer. This kept the optical system complexity under control, since a smaller lens pupil was required. These had the advantage of mask/wafer separation, which eliminated the defect problems of contact litho. However, masks were still difficult to make, since there was no pattern reduction. An example of this type of system is the Perkin Elmer Micralign. These systems were capable of resolving down to 0.7 μm [6]. In the late 1980s step and repeat systems were introduced [6]. These tools imaged only a single field at a time, and typically used 5x reduction optics, making mask fabrication easier. The wafer was then "stepped" under the lens, printing a single die at time. Although these systems featured increasingly larger and more complicated lenses as Numerical Aperture (NA) scaled, they were capable of printing down to the 0.25 μm limit. The last tool evolution was the move from step and repeat systems to step and scan systems. In this approach, a single die is exposed, but the image is scanned through a slit, and the wafer and mask move in synchronized, opposite directions [6]. This is still the current state of the art in optical lithography, although many advances have taken place to improve layer alignment

capability, wavelength and NA scaling have allowed increased resolution to keep pace with the demands of Moore's law, and recently, immersion lithography has allowed a further increase in NA.

Several strategies can be employed to extend resolution capabilities of existing step and scan equipment and processes beyond coherent imaging limits. Two such strategies are off-axis illumination and partially coherent imaging. Off-axis imaging uses non-normal plane waves to illuminate a photomask. The oblique light allows collection of diffracted orders by an objective lens in cases where normal illumination produces no image. Partially coherent imaging uses a collection of plane waves with a range of incident angles, broadening diffraction orders, which the objective lens collects [8]. In both cases, oblique plane waves illuminate the reticle.

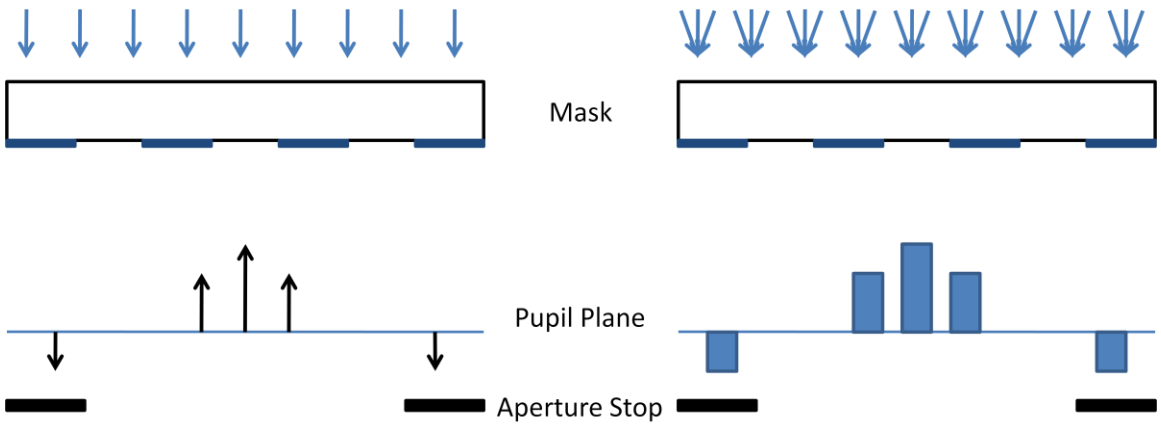


**Figure I.2: Diffraction Patterns from coherent illumination (left) and partially coherent illumination (right).**

Figure I.2 shows the discrete coherent diffraction orders and the broadening of the orders that occurs when partially coherent illumination is used. The diffraction orders have the width of the lens pupil when incoherent illumination is used.

The coherent illumination resolution limit is defined by Equation (1.2), which is known as the Rayleigh Criterion [9].

$$R = 0.5\frac{\lambda}{\mathrm{NA}} \tag{1.2}$$

Here $R$ is the half-pitch Critical Dimension (CD) of a line, $\lambda$ is the illumination wavelength in vacuum, and NA defines the numerical aperture of the exposure system. For fully incoherent illumination, resolution increases by a factor of two:

$$R = 0.25\frac{\lambda}{\mathrm{NA}} \tag{1.3}$$

The quantities 0.5 and 0.25 in Equations (1.2) and (1.3) are values for the process dependent factor $k_1$, which represents all imaging factors for a process that are not wavelength or NA [7].

$$k_1 = \frac{1}{2(\sigma+1)} \tag{1.4}$$

Here, $\sigma$ is the degree of partial coherence, which is a ratio of the effective source size to the full objective aperture size of the imaging system. Although incoherent illumination facilitates an increase in resolution, there is also an accompanying reduction in modulation. The Optical Transfer Function (OTF) describes the frequency response of incoherent imaging systems by relating the image modulation to an input of a given spatial frequency [10]. Modulation is defined as the ratio of the difference to the sum of the intensity extremes.

$$M = \frac{I_{\max} - I_{\min}}{I_{\max} + I_{\min}} \tag{1.5}$$

As an example, Figure I.3 shows a normalized OTF and Coherent Transfer Function (CTF) for two imaging systems. Using partially coherent and incoherent illumination, spatial frequencies (pitches) beyond coherent resolution limits can be printed, although with lower contrast. For these lower fidelity images, nonlinear imaging properties caused by the logarithmic response of the photoresist can be used to improve image quality [11]. Improving the modulation delivered to a resist system has the benefit of increasing a feature's process window and can be achieved using several techniques.

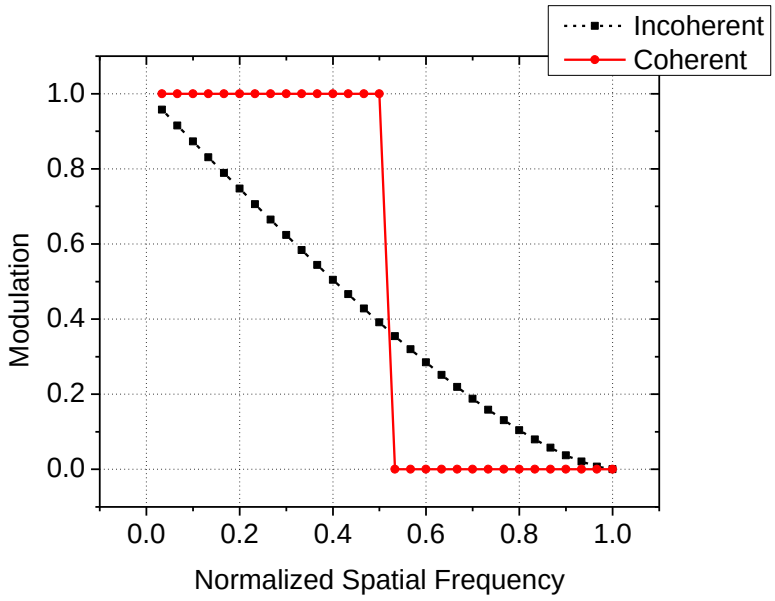


**Figure I.3: Transfer functions of coherent (solid) and incoherent (dash) imaging systems.**

This thesis explores, in part, the use of Evanescent Wave Assist Features for projection lithography as a way to increase the modulation delivered to the resist system. Since immersion lithography will likely be used until at least the 32 nm node, innovative techniques will be required which can maximize pattern fidelity over the full exposure field. Furthermore, these techniques must be outside of the usual scaling mechanisms of

wavelength and NA. Evanescent Wave Assist Features (EWAFs) are sub-wavelength grooves or notches, which are located between mask absorber and substrate or on the bottom surface of the mask absorber, as shown schematically in Figure I.5. They are small enough that they have only evanescent (surface wave) and zero order components. Since these features are blocked by the photomask's absorber layer, they are not optically visible to the propagating light traveling through the imaging system, and therefore pose no risk of printing. An added benefit is that since they are included on or beneath the mask absorber, they require no additional mask space. The assist features are also local, so their spacing and size can be optimized simultaneously for multiple features in a design. Adding EWAFs to a typical transmitting feature on a photomask can further increase contrast and NILS to values not possible through global illumination settings and Optical Proximity Correction (OPC) alone. A lithographic perspective of Figure I.1 is shown in Figure I.4. Lithographic shrinks in both gate length and pitch have enabled the density scaling presented in Figure I.1. As optical lithography must deliver solutions to scale ICs to the 22 nm node, evanescent wave assist features represent a one new tool to deliver the higher fidelity images that will be required at this ultimate limit.

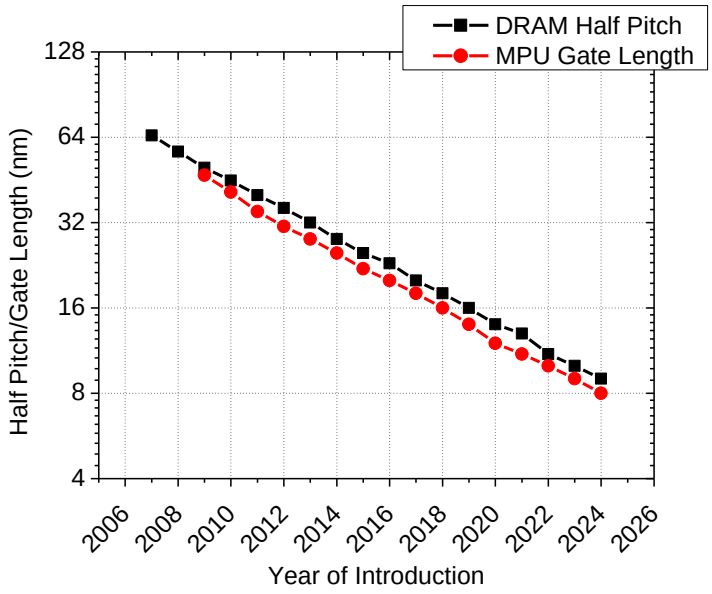


**Figure I.4: ITRS lithographic requirements for DRAM half pitch and MPU gate length in resist [12].**

Although EWAFs resemble traditional scatter bars, it is important to note that a primary function of scatter bars is the attenuation of the isofocal intensity bias across pitch. This variation is due to differences in the transmitted zero order for the assortment of pitches that may be present in a die. Since this bias changes the process window for each pitch, the common process window is reduced [13].

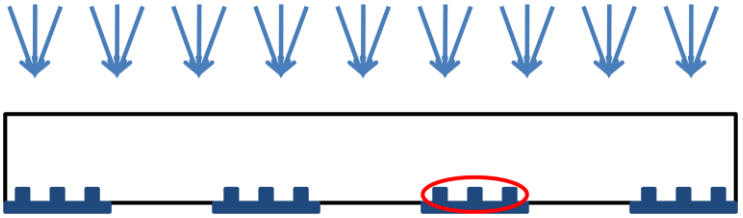

**Figure I.5: Mask Schematic illustrating inclusion of EWAF features.**

The surface wave created by the buried EWAFs can interact with propagating modes transmitted through a mask pattern. The interaction of this engineered surface wave

component with propagating radiation allows image contrast modulation. Further, EWAFs may be used with traditional anti-reflective chromium absorbers, requiring no material change from a mask making perspective. Contrast improvements of up to 2.39x have been observed with rigorous models using Finite-Difference Time-Domain (FDTD) methods and aluminum absorbers [14]. Surface waves generated by EWAFs may also be amplified by Surface Plasmon Polaritons (SPPs) when conductive materials such as aluminum are used. Plasmons are an oscillation of the electron cloud of a conducting material, and have an interesting ability to reduce the attenuation of surface waves in lateral directions. These will be presented in more detail in Chapter II. Using these amplified surface modes results in an increase in the contrast enhancement delivered by an EWAF structure.

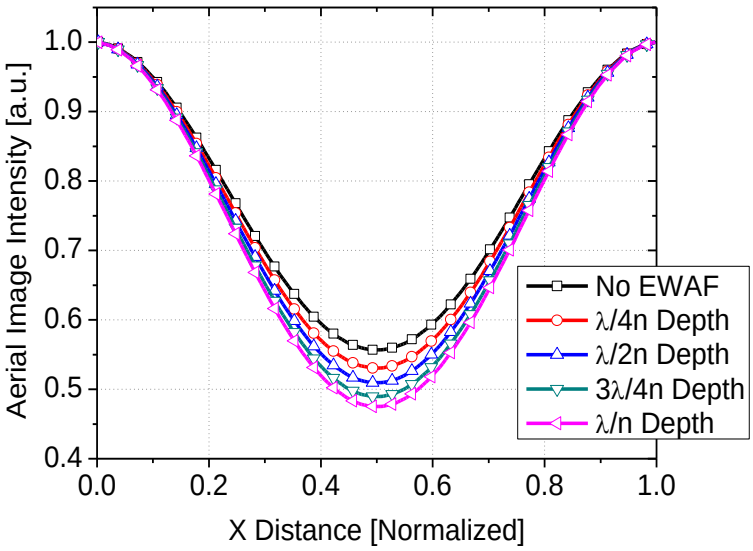


**Figure I.6: Aerial Images of 45 nm spaces at 215 nm pitch. As EWAF depth is increased, contrast improves. Best case contrast increase in this case is 27% [15].**

Figure I.6 shows the aerial images of 45 nm transmitting spaces with 215 nm pitch imaged using unpolarized illumination and a 0.93 NA exposure tool with $\sigma$ of 0.3 [15]. EWAFs, and in turn image contrast, can be optimized for many pitches simultaneously within the exposure field. In this example, EWAFs are responsible for a 27% increase in contrast over the binary mask case.

# II. BACKGROUND

In this chapter, background concepts related to EWAFs are introduced. Evanescent waves are discussed, including their relation to total internal reflection and generation by light traveling through apertures. Evanescence and reciprocity are introduced via a study with microwaves and sub-wavelength slits. Surface plasmons are discussed as a special case of evanescent waves which couple to plasma waves of a conductive surface. Applications of these plasmons are introduced such as transmission enhancement through sub-wavelength apertures. Finally, a summary of key studies involving plasmon transmission enhancement is presented.

## A. Evanescent Waves and Total Internal Reflection

Sir Isaac Newton experimented with evanescent waves in the early 18$^{th}$ century [16]. Newton placed two prisms against each other, and observed that one prism's face was slightly curved, as shown in Figure II.1. This gave a small contact patch between the two when the prisms were pressed into contact with each other. When illuminated, the prism face, bounded by air, satisfied conditions for Total Internal Reflection (TIR). In this case, the beam entering the prism reflected out through the bottom face. The area of the curved prism in contact with the flat prism allowed light to travel straight through, since that area was not bounded by air and conditions for TIR were no longer met. Newton discovered that the spot of light transmitted through the prisms was larger than the contact point and enlarged with applied pressure [16]. Newton was observing

evanescent waves on the surface of the first prism being frustrated to propagation by the second prism over a small gap.

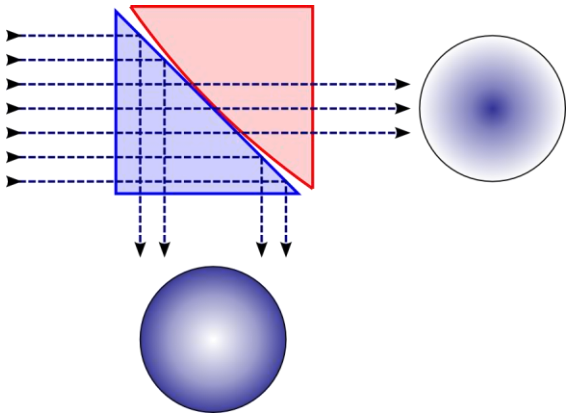

**Figure II.1: Newton's Total Internal Reflection (TIR) experiment, the first observation of evanescent waves [17].**

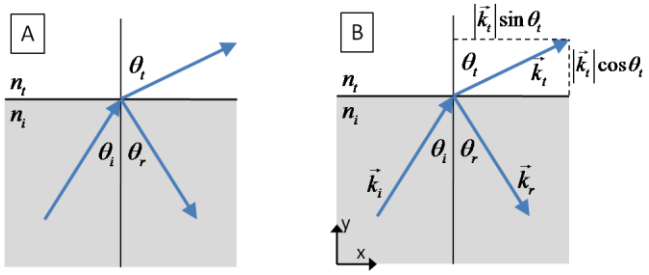


**Figure II.2: A) Plane of Incidence (POI), containing incident, reflected, and transmitted light rays. B) Illustration showing propagation vectors and components.**

To understand evanescent waves and some of their important properties, we consider in more detail the process of TIR. Snell's law, which governs the angle of rays transmitted into non-absorbing media of different refractive indices, is given by [18]:

$$n_i \sin\theta_i = n_t \sin\theta_t \tag{2.1}$$

The subscripts *i* and *t* reference Figure II.2a and indicate incident and transmitting rays, respectively, traveling from a high to low index material. As $\theta_i$ is increased, the critical

angle occurs, defined as $\theta_c$. TIR occurs and all energy from the incident ray is reflected at the interface when $\theta_i$ equals or exceeds $\theta_c$ as:

$$\sin\theta_c = \frac{n_t}{n_i} \tag{2.2}$$

To understand the role of critical angle in transmission and reflection at the interface, consider the reflection coefficient for TE polarized light defined by the Fresnel equations:

$$r_{\mathrm{TE}} = \frac{n_i\cos\theta_i - n_t\cos\theta_t}{n_i\cos\theta_i + n_t\cos\theta_t} \tag{2.3}$$

$$t_{\mathrm{TE}} = \frac{2n_i\cos\theta_i}{n_i\cos\theta_i + n_t\cos\theta_t} \tag{2.4}$$

Using a trigonometric identity, Equation (2.3) can be recast as:

$$r_{\mathrm{TE}} = \frac{\cos\theta_i - \sqrt{\left(\frac{n_t}{n_i}\right)^2 - \sin^2\theta_i}}{\cos\theta_i + \sqrt{\left(\frac{n_t}{n_i}\right)^2 - \sin^2\theta_i}} \tag{2.5}$$

$$t_{\mathrm{TE}} = \frac{2\cos\theta_i}{\cos\theta_i + \sqrt{\left(\frac{n_t}{n_i}\right)^2 - \sin^2\theta_i}} \tag{2.6}$$

$$\begin{aligned} R_{\mathrm{TE}} &= r_{\mathrm{TE}} r_{\mathrm{TE}}^* \\ T_{\mathrm{TE}} &= \left(\frac{n_t\cos\theta_t}{n_i\cos\theta_i}\right) t_{\mathrm{TE}} t_{\mathrm{TE}}^* \end{aligned} \tag{2.7}$$

Similarly, for TM polarized light, the Fresnel equations are defined as:

$$r_{\mathrm{TM}} = \frac{n_t\cos\theta_i - n_i\cos\theta_t}{n_i\cos\theta_t + n_t\cos\theta_i} \tag{2.8}$$

$$t_{\mathrm{TM}} = \frac{2n_i \cos\theta_i}{n_i \cos\theta_t + n_t \cos\theta_i} \tag{2.9}$$

Similarly, Equations (2.8) and (2.9) can be recast in terms of incidence angle only:

$$r_{\mathrm{TM}} = \left(\frac{n_t}{n_i}\right)^2 \frac{\cos\theta_i - \sqrt{\left(\frac{n_t}{n_i}\right)^2 - \sin^2\theta_i}}{\cos\theta_i + \sqrt{\left(\frac{n_t}{n_i}\right)^2 - \sin^2\theta_i}} \tag{2.10}$$

$$t_{\mathrm{TM}} = \frac{2\frac{n_t}{n_i}\cos\theta_i}{\left(\frac{n_t}{n_i}\right)^2 \cos\theta_i + \sqrt{\left(\frac{n_t}{n_i}\right)^2 - \sin^2\theta_i}} \tag{2.11}$$

Equation (2.7) remains unchanged for TM polarized reflectance and transmittance:

$$\begin{aligned} R_{\mathrm{TM}} &= r_{\mathrm{TM}} r_{\mathrm{TM}}^* \\ T_{\mathrm{TM}} &= \left(\frac{n_t \cos\theta_t}{n_i \cos\theta_i}\right) t_{\mathrm{TM}} t_{\mathrm{TM}}^* \end{aligned} \tag{2.12}$$

Equations (2.5) and (2.10) will have a negative root beyond the critical angle, when $\theta_i > \theta_c$, and therefore a complex valued amplitude reflection coefficient. Because of the complex valued amplitude reflection coefficients in Equations (2.5) and (2.10) and the complex amplitude transmission coefficients in Equations (2.6) and (2.11), the complex conjugates of the amplitude coefficients $r^*_{\mathrm{TE,TM}}$ and $t^*_{\mathrm{TE,TM}}$ must be used when calculating reflectance and transmission. Although the reflection coefficient is not unity beyond the critical angle, the reflectance, *R*, defined by Equations (2.7) and (2.12), converges to one. The transmission coefficient also becomes complex beyond the critical angle. This suggests that a field is transmitted across the interface, but the transmittance, *T*, remains

zero since by definition the angle of transmission, $\theta_t$ in Equations (2.7) and (2.12), must always be at 90°, even though the field is complex. In other words, the field traverses the boundary but cannot carry energy over it, eliminating transmission and satisfying the TIR condition [18]. Figure II.2b illustrates the propagation vectors of the plane wave at the interface of two materials. The transmitted propagation vector has two components, $k_{tx}$ and $k_{ty}$, defined as:

$$\begin{aligned} k_{tx} &= \left|\vec{k}_t\right| \sin\theta_t \\ k_{ty} &= \left|\vec{k}_t\right| \cos\theta_t \end{aligned} \tag{2.13}$$

The *y*-component of the propagation vector can be recast into an expression involving incident angle:

$$k_{ty} = \pm\left|\vec{k}_t\right| \sqrt{1 - \frac{\sin^2\theta_i}{\left(\frac{n_t}{n_i}\right)^2}} = \pm i\left|\vec{k}_t\right| \sqrt{\frac{\sin^2\theta_i}{\left(\frac{n_t}{n_i}\right)^2} - 1} = \pm i\beta \tag{2.14}$$

$$k_{tx} = \frac{\left|\vec{k}_t\right|}{\left(\frac{n_t}{n_i}\right)} \sin\theta_i \tag{2.15}$$

As the incident angle increases beyond the critical angle, the *y*-component of the propagation vector becomes purely imaginary. The positive root is physically impossible and must be neglected as it represents a wave whose amplitude increases in the propagating *y* direction. This is also dictated by the principles of conservation of energy. The negative root explains the exponential decay of the field with increasing *y* distance from the high/low index material interface in Figure II.2b [18]. When these wave vector components are inserted into the complex representation of a wave, the result is:

$$\vec{E}_t = \vec{E}_{0t} e^{\mp \beta y} e^{i\left(\left|\vec{k}_t\right| x \sin\theta_i / n_{ti}\right)} \tag{2.16}$$

In Equation (2.16), $\vec{E}_{0t}$ represents the electric field transmitted immediately across the boundary of high and low index materials, and $n_{ti}$ is a simplification for the sine of the critical angle, $n_t/n_i$. Evanescent waves are also known as inhomogeneous waves, since their surfaces of constant phase are perpendicular to their surfaces of constant amplitude. In a propagating wave, the surfaces of constant phase and amplitude are parallel. In summary, a field incident upon a high to low index interface beyond critical angle does transmit a field across the boundary, however, it is exponentially damped in the *y* direction, and does not carry any energy into the lower index medium [18].

An important property of evanescent waves, which should be noted, is that although they cannot transmit energy into the second medium, they can transfer energy laterally along the high/low index material interface. The Poynting vector, named after British physicist John Henry Poynting, defined in Equation (2.17), describes the direction of the flow of energy of a wave (in CGS units):

$$\vec{S} = \frac{c}{4\pi}\left(\vec{E} \times \vec{H}\right) \tag{2.17}$$

Referencing Figure II.2, the time average of $\left\langle S_{ty} \right\rangle$ can be proven equal to zero, however $\left\langle S_{tx} \right\rangle$ is generally finite [19]. Therefore, the evanescent wave bound to the interface can carry energy in lateral directions. Chapter VI contains a more detailed explanation of the power flow across the interface.

There is a special condition which Newton discovered known as Frustrated Total Internal Reflection (FTIR). In this case, another high index material is brought suitably

close (usually within a few wavelengths) to the interface with TIR. Although no direct contact is made, the exponentially decaying portion of the *y* direction electric field enters the second high index media and "frustrates" back to propagation. The strength of the transmitted field is highly dependent on the physical gap between the two high index materials. This effect is used extensively in touch screens and couplers in integrated photonics, as shown in Figure II.3 [20], [21].

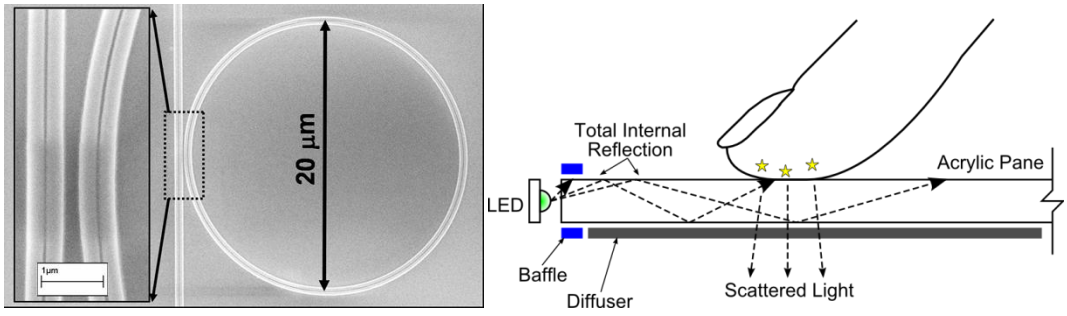


**Figure II.3: Left: A ring resonator uses FTIR to couple a field traveling in the straight waveguide to the ring [21]. Right: FTIR touch screen sensor [20].**

### B. Evanescent Waves and Apertures

Passing light through an aperture in a screen also generates evanescent waves. If a plane wave illuminates an aperture of arbitrary size, a propagating component and an evanescent surface-bound component exist, as shown in Figure II.4.

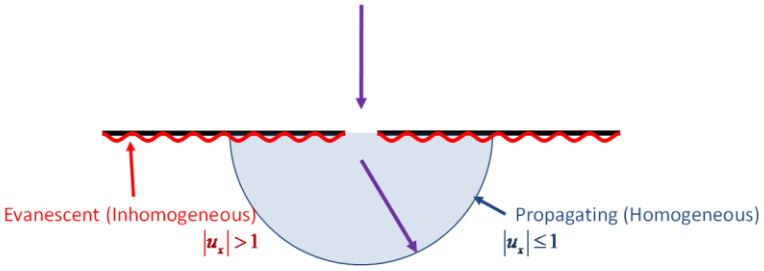


**Figure II.4: A plane wave illuminating an aperture in an opaque screen.**

Kowarz describes this relationship using scalar fields from a single slot or hole and a superposition of plane waves in the angular spectrum representation [22]:

$$U(x,z) = U_h(x,z) + U_i(x,z) \tag{2.18}$$

$$U_h(x,z) = \int_{|u_x|\le 1} a(u_x) e^{iku_x} e^{ikz\sqrt{1-u_x^2}} du_x \tag{2.19}$$

$$U_i(x,z) = \int_{|u_x|>1} a(u_x) e^{iku_x} e^{-kz\sqrt{u_x^2-1}} du_x \tag{2.20}$$

In Equations (2.18) through (2.20), *U(x,z)* represents the superposition of plane waves that form the electric field of the one dimensional diffracting aperture along the *x* direction, $u_x$ represents the direction cosine of these plane waves, and $a(u_x)$ is the amplitude of each plane wave component. By including evanescent waves, any number of angular frequencies can be included in *U(x,z)* and therefore there is no fundamental diffraction resolution limit. The evanescent field component, $U_i(x,z)$, is confined to the *z* plane of the diffracting aperture. This component is attenuated with increasing *z* direction such that at large *z* distances it contributes negligibly to the total field [23]. Propagating, evanescent, and total electric fields can be seen at various *z* distances from a $5\lambda$ slot in Figure II.5. The resolution of conventional optical systems is fundamentally limited by the by the propagating components of a field, therefore the evanescent wave is a plausible physical explanation to the diffraction limit in optics. This explains why contact or near-field evanescent lithography is able to exceed classical resolution limits [24].

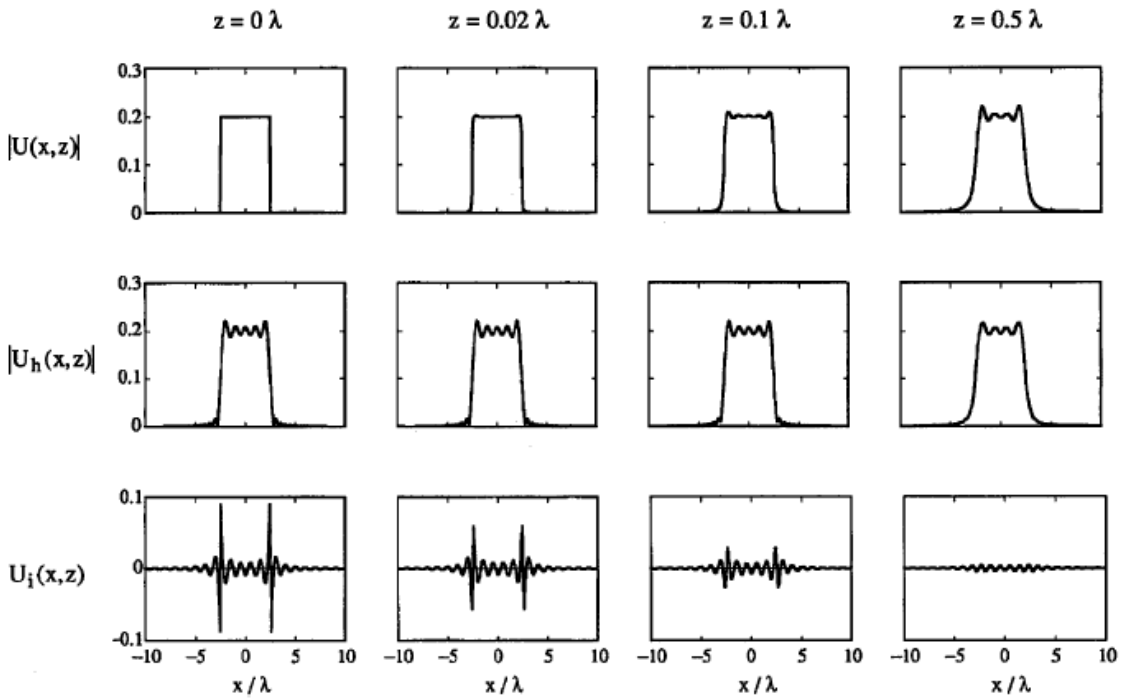


**Figure II.5: Contributions of the propagating and evanescent field to near-field images of a transmitting slot. The slot is width $d$=5$\lambda$ [22].**

### C. Diffraction Gratings and Evanescent Orders

Diffraction gratings also create evanescent modes. The grating equation below describes the property of gratings to direct light into clearly distinguished directions [25]. The discrete diffracted beams are known as diffraction orders.

$$\sin\theta_m = \sin\theta_i + m\frac{\lambda}{d},\ m = 0, \pm1, \pm2, \ldots \tag{2.21}$$

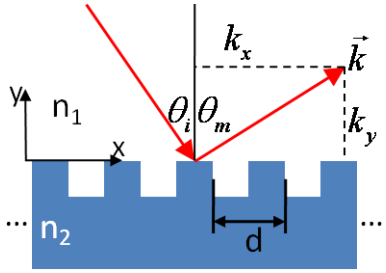


**Figure II.6: Light diffracting from a reflective grating and related terms.**

In the grating equation, the subscript *m* defines the particular order that is reflected from the grating, while $\lambda$ and *d* are the wavelength and grating pitch, respectively. The grating equation will only yield a real solution when the diffracted orders emerge at an angle less than 90 degrees.

$$\left|\sin\theta_m\right| < 1 \tag{2.22}$$

The wave vectors for these propagating orders are given by Equation (2.23) and illustrated in Figure II.6 and Figure II.7. Although a reflective grating is shown, transmission gratings operate similarly.

$$\begin{aligned} k_{mx} &= k_{ix} + m\frac{2\pi}{d} \\ k_{mz} &\equiv k_{iz} \end{aligned} \tag{2.23}$$

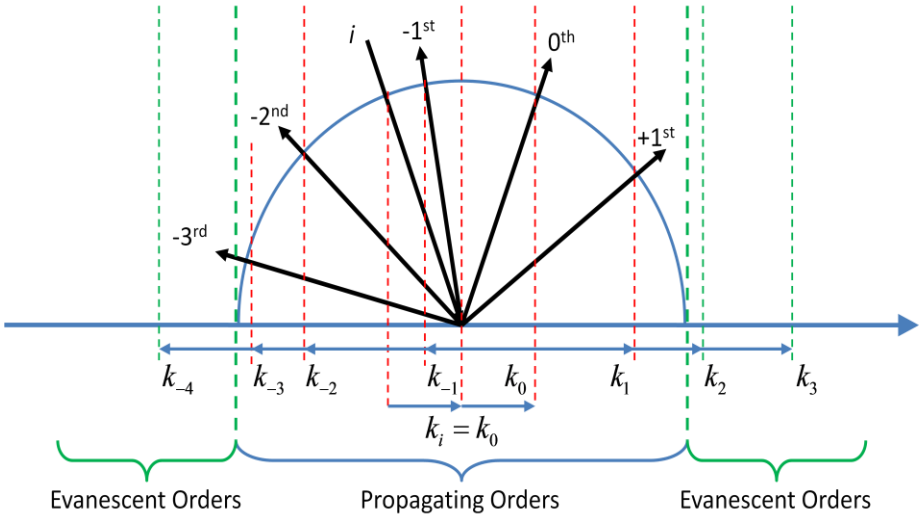


**Figure II.7: Grating under oblique incidence showing *x*-direction wave vector components from *m*=-3 through *m*=1 [25].**

Evanescent orders, shown in Figure II.7 as $k_4$, $k_2$, and $k_3$, are generated along with propagating orders. The wave equation relates the *x* and *y* components of the wave vector

to each other. This is given in Equation (2.24), where $\lambda$ is the wavelength of illumination in vacuum, and $n$ represents the index of refraction of the half-space above the grating (for reflection mode gratings).

$$k_x^2 + k_y^2 = \left(\frac{2\pi}{\lambda} n\right)^2 \tag{2.24}$$

This can be recast in a form where the $y$ component of the wave vector may be determined from the $x$ component. When the $x$ component of the wave vector grows larger than the wave number, it forces the $y$ component to become imaginary, resulting in an evanescent, or bound mode, which is confined to the grating surface.

$$k_{my} = \pm i \sqrt{k_{mx}^2 - \left(\frac{2\pi}{\lambda} n\right)^2} \tag{2.25}$$

This yields Equation (2.25), which describes the $y$ component of the diffracted orders, given the $x$ component of the incident radiation is larger than the wave number. Solving Equation (2.24) for $k_{mx}$ and inserting into Equation (2.23) gives the grating equation in terms of the output $y$ component when the input $x$ component is given. When $k_{ix}$ is larger than the wave number, $k_{my}$ becomes imaginary as in Equation (2.26):

$$k_{my} = \pm i \sqrt{k_{ix}^2 + \left(m\frac{2\pi}{d}\right)^2 + m\frac{4\pi}{d} k_{ix} - \left(\frac{2\pi}{\lambda} n\right)^2} \tag{2.26}$$

Just as in TIR, the imaginary $y$ component of the output wave vector indicates that the field decays exponentially with increasing distance from the grating surface. As the grating pitch is reduced, its orders will have increased angular spread. In the limit, when $d \leq \lambda$, all diffraction orders, except for the zeroth, will be evanescent (assuming normal

incidence). This type of grating is known as a zero-order grating. When the wave vector components are inserted into complex notation for electric fields, the imaginary *y* component will have an identical effect to that in Equation (2.16). Gratings may also be patterned and used to convert existing evanescent waves back to propagating light. In fact, this is one way to couple into surface plasmons. In most analysis, sinusoidal gratings are considered, which have only one frequency component [26]. Using Fourier series techniques to decompose square gratings into components of relative strengths, these gratings may also be easily considered [27].

### D. Evanescent Waves and Reciprocity

In the same way a nearby high-index material can frustrate an evanescent wave to propagation, a nearby slot may also perturb an evanescent field. Leviatan conducted simulations using microwave radiation and two sub-wavelength slots in a perfectly opaque screen. The first slot was placed at $x=z=0$, with a slot width of $0.05\lambda$. The second slot was $0.01\lambda$ wide and was varied in both lateral and transverse positions relative to the first [28]. The geometry of the experiment can be seen in Figure II.8.

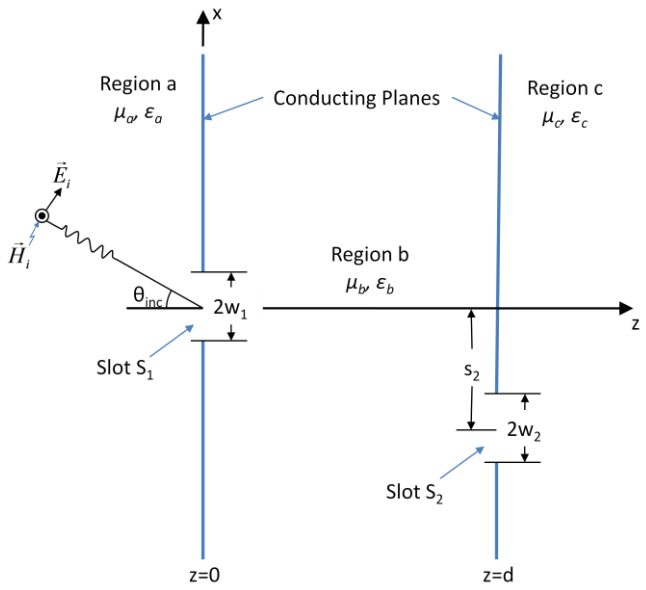


**Figure II.8: The layout and relevant quantities of Leviatan's parallel slot coupling experiment [28].**

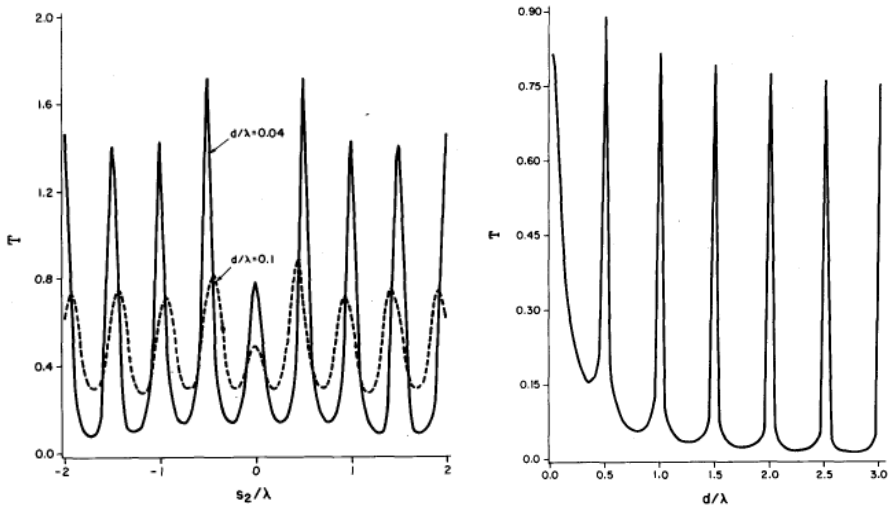


**Figure II.9: Transmission coefficient as a function of *x* shift of slot $s_2$ (left). Transmission coefficient as a function of *z* shift of slot $s_2$ (right) [28].**

In these simulations, the transmission coefficient, *T*, is defined as the power transmitted through the second aperture to region *c*, normalized by the power incident on the first aperture from region *a*.

$$T = \frac{P_{\text{trans}}}{P_{\text{inc}}} \tag{2.27}$$

Figure II.9 (left) shows the transmission as slot $s_2$ is swept from -2$\lambda$ to 2$\lambda$ in the $x$ direction. Peaks are located at $\lambda/2$ multiples of position, and have lower transmission coefficient and broader peaks as the $z$ spacing between slots is increased. Similar $\lambda/2$ resonances were also observed with $s_2$ $x$ spacing constant at zero while adjusting $z$ spacing [28]. Leviatan noted that the appearance of the multiple peaks "cast a severe drawback for scanning ultra microscopy and photolithography." The ability of the slot $s_2$ to interact with an evanescent field, however, was a major contribution because it proves the concept of reciprocity. The pitch of transmission peaks (and troughs) at $\lambda/2$ clearly shows characteristics of the evanescent field along the perfect conductor, while the central peak at $s_2/\lambda$=0 which decreases and broadens significantly with increasing vertical distance shows the properties of direct transmission of light. Since the small dimensions of the slots confine the zero order light to a rapidly expanding hemisphere, if no other phenomena were present, the function would decay monotonically with lateral movement as less light travels through the second slot. The earlier point of evanescent fields needing to be perturbed to propagation in order to be detected is also reinforced. Without the second slot, the detected transmission would only be due to forward propagating zero order light from the first aperture.

### E. Guided Evanescent Waves: Surface Plasmon Polaritons

Surface plasmon polaritons (SPPs) are the quanta of charge oscillations of the "electron gas" present along the surface of conductors. Using the proper in-plane electric field, the "electron gas" can be influenced and SPPs are induced. SPPs are evanescently

confined to an interface between a conductor and an insulator, propagating in lateral directions [29]. Figure II.10 illustrates two particular interfaces meeting this criterion: a plane interface and a periodically structured (grating) interface.

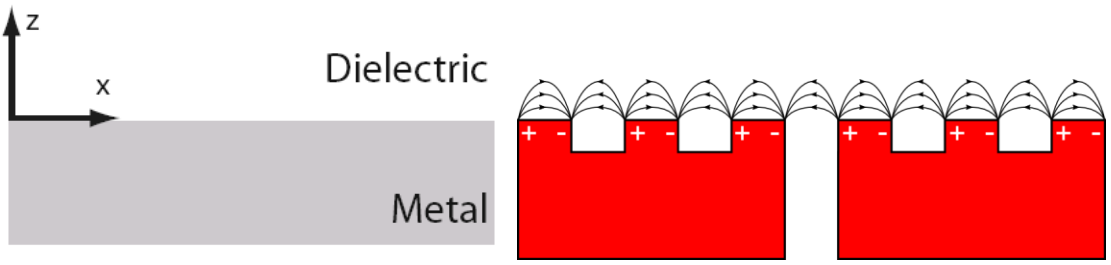


**Figure II.10: Left: Schematic and coordinate system used for plasmonic excitation at a metal/dielectric interface [29]. Right: A corrugated surface can act as a grating, coupling incoming light to surface plasmon polaritons [30].**

Plasmons are useful in a variety of applications because their dispersion allows SPPs to have frequency characteristics that depart significantly from light traveling through dielectric materials. For instance, Figure II.11 illustrates a plasmon dispersion relation for a generic conductor using the plasma model to define its dielectric function, $\varepsilon(\omega)$ [29]. Equation (2.28) shows the plasma model for the metal's dielectric function.

$$\varepsilon(\omega) = 1 - \frac{\omega_p^2}{\omega^2 + i\gamma\omega} \tag{2.28}$$

Here, the metal's bulk plasma frequency is $\omega_p$, the angular temporal frequency of input radiation is $\omega$, and $\gamma$ is defined as the relaxation frequency, $1/\tau$. Although most materials do not follow this model exactly, it illustrates the role of the free electron gas in observed plasmon dispersions. Since the SPP dispersion curve lies to the right of the dielectric light line, SPPs can only be excited by an appropriate evanescent wave. In practice, this

evanescent wave is usually provided using a evanescent modes from a grating or from a prism using an Attenuated Total Reflection (ATR) technique.

Figure II.11 is known as a dispersion diagram and has several interesting features that are characteristic of SPP systems. The diagram relates the in-plane angular temporal frequency of radiation above the interface at $z>0$ in Figure II.10 (input to the system, $y$-axis) to the in-plane wave vector component (or in this case the angular temporal frequency) just over the interface $z=0$ (output from the system, $x$-axis). First, the two straight lines marked as air and silica represent the light lines of two separate dielectric materials used with an ideal conductor. The light lines illustrate the case of light travelling through the dielectric material systems with no metal present. In other words, it is replaced by free space. The air case, with $n\approx1$, has identical input and output frequencies. The radiation in the fused silica case increases angle via Snell's law upon going from high index to low index material. This results in the more tilted light line for the fused silica example, proportional to the refractive index of dielectric. The in-plane angular temporal frequency in silica that is input to the system becomes larger after the beam refracts in air. Replacing free space with metal gives the unique dispersion described by the blue and red curves. This relationship will be derived later, but quantitatively, when a given angular temporal frequency near the surface plasmon frequency, $\omega_{sp}$, is used as an input to the system, the angular temporal frequency along the interface departs significantly from the linear relationship of dielectric light lines. The asymptote in Figure II.11 represents the surface plasmon; for a certain frequency of light used to excite the plasmon mode, the plasmon frequency is much higher. At the surface plasmon frequency for these theoretical materials, the plasmon takes on a standing wave

character, and $\lambda \rightarrow 0$. With real materials, even though the limit is not reached, the plasmon frequency is generally much larger than the excitation frequency.

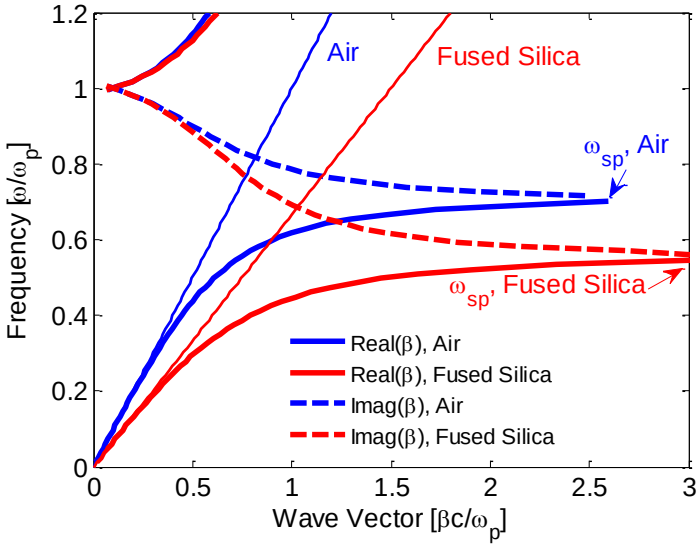


**Figure II.11: Plasmon dispersion for a generic metal represented by a plasma model.**

Because comparatively larger wavelengths of light can be used to excite plasmons of very short wavelength, plasmons are a unique way of squeezing light into smaller areas and "amplifying" electric fields, as will be discussed shortly. The main quantity describing surface plasmons is $\beta$, the $x$-direction wave vector of the surface plasmon. The dispersion relationship of SPPs at a planar surface, such as that in Figure II.10, may be derived by finding the solution of Maxwell's equations on each side of the material boundary, and applying boundary conditions that equate the tangential components of the magnetic and electric fields, similar to [29], [31]. The starting point is the classical wave equation assuming no external stimuli to the system:

$$\nabla^2 \vec{E} = \frac{\varepsilon}{c^2} \frac{\partial^2 E}{\partial t^2} \tag{2.29}$$

Here $c$ is the speed of light and $\varepsilon$ represents the permittivity of the propagation medium. Harmonic time dependence is assumed, $\vec{E}(\vec{r},t)=\vec{E}(\vec{r})e^{-i\omega t}$, which then leads to the Helmholtz Equation:

$$\nabla^2\vec{E}+k_0^2\varepsilon\vec{E}=0 \tag{2.30}$$

Since $k_0=\omega/c=\omega\sqrt{\mu_0\varepsilon_0}$, the substitution can be made after the second derivative. In the planar geometry of Figure II.10 (left) the dielectric function only depends on the $z$ location, so the problem can be simplified by casting $\varepsilon$ as $\varepsilon(z)$ and placing the interface at the $z$=0 plane. The 1-D problem also assumes that waves are only propagating in the $x$ direction. In other words, we are only concerned with solutions of waves that are propagating in the lateral directions along the interface, with no $z$ or $y$ propagation component; these waves are bound. The propagating waves can now be described as (where $\beta=k_x$):

$$\vec{E}(x,y,z)=\vec{E}(z)e^{i\beta x} \tag{2.31}$$

Combining Equations (2.30) and (2.31), the desired form of the wave equation for this problem geometry results:

$$\frac{\partial^2\vec{E}(z)}{\partial z^2}+\left(k_0^2\varepsilon-\beta^2\right)\vec{E}=0 \tag{2.32}$$

$$\frac{\partial^2\vec{B}(z)}{\partial z^2}+\left(k_0^2\varepsilon-\beta^2\right)\vec{B}=0 \tag{2.33}$$

Next, the field profiles for both $\vec{E}$ and $\vec{H}$ can be determined by expanding Maxwell's Curl Equations and using the constitutive relation in non-magnetic media, $\vec{B} = \mu_0 \vec{H}$ and $\vec{D} = \varepsilon_0 \vec{E}$ [29].

$$\nabla \times \vec{E} = \left( \frac{\partial E_z}{\partial y} - \frac{\partial E_y}{\partial z} \right) \hat{x} + \left( \frac{\partial E_x}{\partial z} - \frac{\partial E_z}{\partial x} \right) \hat{y} + \left( \frac{\partial E_y}{\partial x} - \frac{\partial E_x}{\partial y} \right) \hat{z} = -\frac{\partial \vec{B}}{\partial t} \tag{2.34}$$

$$\nabla \times \vec{H} = \left( \frac{\partial H_z}{\partial y} - \frac{\partial H_y}{\partial z} \right) \hat{x} + \left( \frac{\partial H_x}{\partial z} - \frac{\partial H_z}{\partial x} \right) \hat{y} + \left( \frac{\partial H_y}{\partial x} - \frac{\partial H_x}{\partial y} \right) \hat{z} = \frac{\partial \vec{D}}{\partial t} \tag{2.35}$$

Equation (2.34) yields the 3 $\vec{H}$ field components, while Equation (2.35) yields the 3 $\vec{E}$ field components:

$$\begin{aligned} \frac{\partial E_z}{\partial y} - \frac{\partial E_y}{\partial z} &= i\omega\mu_0 H_x \\ \frac{\partial E_x}{\partial z} - \frac{\partial E_z}{\partial x} &= i\omega\mu_0 H_y \\ \frac{\partial E_y}{\partial x} - \frac{\partial E_x}{\partial y} &= i\omega\mu_0 H_z \end{aligned} \tag{2.36}$$

$$\begin{aligned} \frac{\partial H_z}{\partial y} - \frac{\partial H_y}{\partial z} &= -i\omega\varepsilon_0 \varepsilon E_x \\ \frac{\partial H_x}{\partial z} - \frac{\partial H_z}{\partial x} &= -i\omega\varepsilon_0 \varepsilon E_y \\ \frac{\partial H_y}{\partial x} - \frac{\partial H_x}{\partial y} &= -i\omega\varepsilon_0 \varepsilon E_z \end{aligned} \tag{2.37}$$

These equations further simplify to:

$$\begin{aligned}
&\frac{\partial E_y}{\partial z} = -i\omega\mu_0 H_x \\
&\frac{\partial E_x}{\partial z} - i\beta E_z = i\omega\mu_0 H_y \\
&i\beta E_y = i\omega\mu_0 H_z
\end{aligned} \tag{2.38}$$

$$\begin{aligned}
&\frac{\partial H_y}{\partial z} = i\omega\varepsilon_0\varepsilon E_x \\
&\frac{\partial H_x}{\partial z} - i\beta H_z = -i\omega\varepsilon_0\varepsilon E_y \\
&i\beta H_y = -i\omega\varepsilon_0\varepsilon E_z
\end{aligned} \tag{2.39}$$

Equations (2.38) and (2.39) provide two sets of solutions, depending on whether TE or TM polarization is considered. In other words, the solution can have $H_x$, $E_y$, and $H_z$ components that are non-zero (TE) or $E_x$, $H_y$, and $E_z$ components that are non-zero (TM). For TM polarization, the $H_x$, $E_y$, and $H_z$ components are all zero, reducing Equations (2.38) and (2.39) to:

$$\begin{aligned}
&\frac{\partial E_x}{\partial z} - i\beta E_z = i\omega\mu_0 H_y \\
&E_x = \frac{-i}{\omega\varepsilon_0\varepsilon}\frac{\partial H_y}{\partial z} \\
&E_z = \frac{-\beta}{\omega\varepsilon_0\varepsilon} H_y
\end{aligned} \tag{2.40}$$

The latter two equations can be substituted back into the top, yielding the wave equation for this particular guided surface mode under TM polarization.

$$\frac{\partial^2 H_y}{\partial z^2} + \left(k_0^2\varepsilon - \beta^2\right) H_y = 0 \tag{2.41}$$

Since Equation (2.41) is in terms of $H_y$, a generic wave of that component (with evanescent decay in the *z* direction) is first assumed for both the dielectric and conducting

media. The decay implies an imaginary wave vector component, similar to Equation (2.16).

$$H_y(z) = A_2 e^{i(k_x x + i k_z z)} = A_2 e^{i\beta x} e^{-k_2 z} \tag{2.42}$$

In (2.42) the $z>0$ half-space solution is shown; $k_x=\beta$ and $k_z$ is simplified to $k_2$, since it is the $z$ component wavevector in medium 2, the dielectric. Further, the other two permitted field components for TM polarization in the $z>0$ half-space can be determined via substitution of Equation (2.42) into the last two equations in Equation (2.40):

$$E_x(z) = \frac{ik_2}{\omega\varepsilon_0\varepsilon_2} A_2 e^{i\beta x} e^{-k_2 z} \tag{2.43}$$

$$E_z(z) = \frac{-\beta}{\omega\varepsilon_0\varepsilon_2} A_2 e^{i\beta x} e^{-k_2 z} \tag{2.44}$$

Three more solutions can be found for the field components on the opposite side of the material interface, $z<0$. The key difference is in the sign of the $k_1$ superscript due to the negative $z$ quantity, and the $\varepsilon_1$ quantity to represent the dielectric function of the conductor.

$$H_y(z) = A_1 e^{i\beta x} e^{k_1 z} \tag{2.45}$$

$$E_x(z) = \frac{-ik_1}{\omega\varepsilon_0\varepsilon_1} A_1 e^{i\beta x} e^{k_1 z} \tag{2.46}$$

$$E_z(z) = \frac{-\beta}{\omega\varepsilon_0\varepsilon_1} A_1 e^{i\beta x} e^{k_1 z} \tag{2.47}$$

Using Equations (2.42) through (2.47), the boundary conditions can be applied which equate the tangential field components across the interface. First, $H_y$ must be continuous

at $z$=0, which yields $A_1$=$A_2$. Second, $\varepsilon_i E_x$ ($i$=1,2) must be continuous at $z$=0 which yields (since $A_1$=$A_2$):

$$\begin{aligned} A_2 \frac{1}{\varepsilon_2} k_2 &= -A_1 \frac{1}{\varepsilon_1} k_1 \\ \frac{k_2}{k_1} &= \frac{-\varepsilon_2}{\varepsilon_1} \end{aligned} \tag{2.48}$$

A consequence of Equation (2.48) is that confinement of the surface waves demands that the real part of $\varepsilon_1$ be less than zero and the real part of $\varepsilon_2$ be greater than zero. In other words, the surface plasmons can only exist at the interface between a conductor and insulator. The wave vector components must also obey the wave equation. If the partial second derivative (with respect to $z$) of Equation (2.42) is substituted back into the wave equation for the guided surface modes, Equation (2.41), the wave vector components are related as follows:

$$k_1^2 = \beta^2 - k_0^2 \varepsilon_1 \tag{2.49}$$

$$k_2^2 = \beta^2 - k_0^2 \varepsilon_2 \tag{2.50}$$

Using the dielectric functions of the insulator/metal system under analysis, a dispersion relationship may be obtained. Using Equation (2.48) to relate the wave vector $z$ components to each other finally gives Equation (2.51). The dispersion relation for surface plasmon polaritons at the interface becomes:

$$\beta = k_0 \sqrt{\frac{\varepsilon_1 \varepsilon_2}{\varepsilon_1 + \varepsilon_2}} \tag{2.51}$$

Here $k_0$ represents the free space wave number of incident radiation on the metal surface, and the subscripts of the dielectric function $\varepsilon$ refer to the insulator (2), and the conductor

(1) from Figure II.10. The dielectric functions can be determined from the more familiar refractive index, *n*, and extinction coefficient, *k*, by using:

$$\mathrm{Re}(\varepsilon) = n^2 - k^2 \tag{2.52}$$

$$\mathrm{Im}(\varepsilon) = 2nk \tag{2.53}$$

It is important to note that $\mathrm{Re}\{\varepsilon_1\}$ is negative, which guarantees that $\beta$ will be larger than $k_0$. In other words, the plasmon will have a shorter wavelength than its excitation source. The large field enhancement that takes place along the metal surface when resonance conditions are met is therefore due to the allowed field discontinuities between the *z* direction electric field of the two half spaces. From an intuitive standpoint, with TE illumination, there is always continuity of the $\vec{E}$ field across the boundary, so no enhancement can take place. The boundary conditions also make it impossible to find a TE guided wave solution.

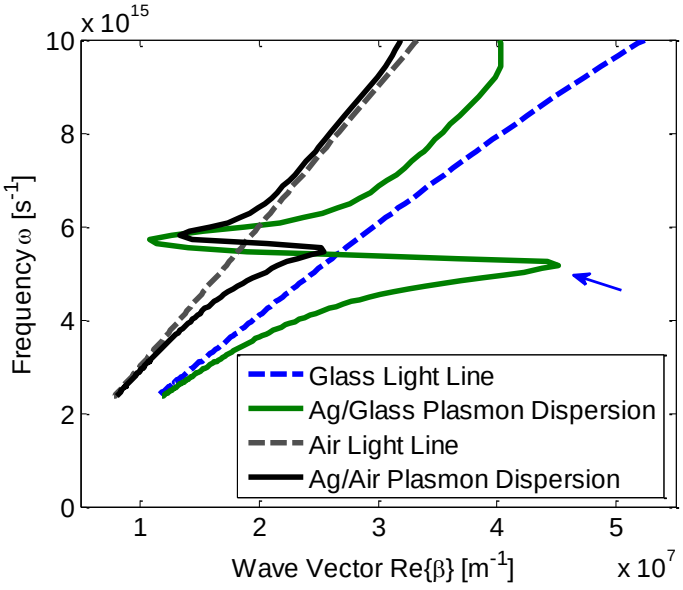


**Figure II.12: SPP dispersion relation for both Ag/air and Ag/silica interfaces [29].**

A special case of SPPs known as Surface Plasmons can be identified at a metal's plasma frequency, $\omega_p$, given by Equation (2.54). This is seen in Figure II.12 at the kink point for the plasmon dispersion, where:

$$\omega_{sp} = \frac{\omega_p}{\sqrt{1+\varepsilon_2}} \tag{2.54}$$

In a lossless conductor, where there is no damping of electronic oscillations in the metal, the wave vector $\beta$ goes to infinity, meaning the plasmon wavelength tends to zero, and its group velocity, $v_g$, goes to zero, becoming a standing wave. Traveling SPPs are attenuated in lateral directions when real materials are used, and their characteristic propagation length is defined as:

$$L = \frac{1}{2\,\mathrm{Im}[\beta]} \tag{2.55}$$

### F. Sub-Wavelength Apertures and Transmission Enhancement

A decade or so following Leviatan's work, Ebbesen and coworkers at NEC began experimenting with arrays of small holes etched in metal films. The original purpose of the films was for use as a sample holder for single molecule spectroscopy. These hole arrays demonstrated very high transmission under visible light, far greater than calculated for the hole sizes involved since transmission through sub-wavelength holes scales as [32]:

$$T \propto \left(\frac{d}{\lambda}\right)^4 \tag{2.56}$$

In Equation (2.56) the quantity $d$ is the diameter of the circular hole, while $\lambda$ is the wavelength of light. The original microscopy experiments were abandoned and the study

of this unique hole array became a primary interest. The investigation of the physical principles responsible for the enhanced transmission has led several research groups in different directions [33].

In reporting anomalous transmission through a hole array, Ebbesen cited SPPs as the probable mechanism for enhanced zero order transmission due to the observance of faint band splitting, evidence of Umklapp processes and SP standing waves [34], [26]. Separate films of Ag, Au, Cr, and Ge were patterned with 150 nm diameter holes on a 0.9 μm pitch and tested from UV through infrared. The enhancement of zero order transmission through the holes did not occur when Ge was used as a substrate, supporting the hypothesis that SPPs were responsible since germanium does not behave as a metal in this wavelength regime. In addition, the enhancement peaks shown in Figure II.13 were highly sensitive to illumination angle. In fact, the angular dependence of the transmission peaks was similar to well-known behavior when light couples to SPPs in reflection gratings [34]. Based on this study, the mechanism behind the observed large transmission gain was thought to be purely plasmon related.

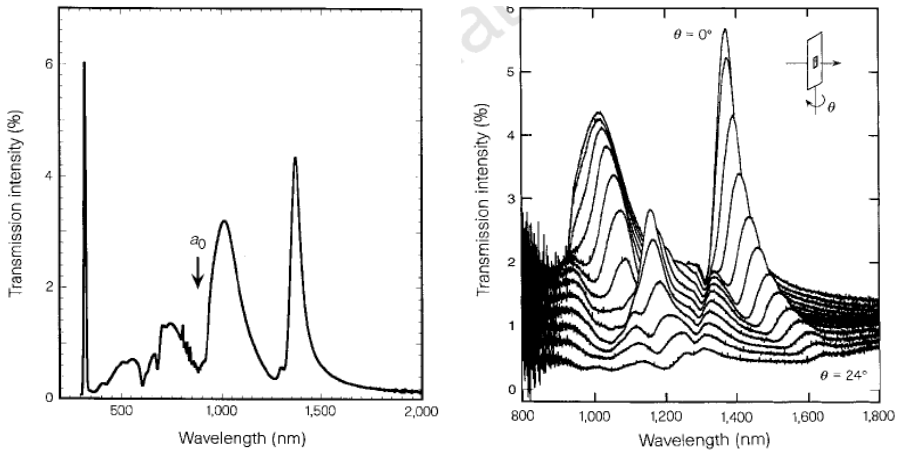


**Figure II.13: Transmission through sub-wavelength holes patterned in Ag as a function of wavelength (left) and illumination angle and wavelength (right) [34].**

Ebbesen, et al. later revisited these structures and found that in addition to transmission maxima due to SPPs, there was also a transmission minima related to a Wood's Anomaly [35].

Wood's Anomalies are named after their first observer, American physicist R. W. Wood. While observing reflection gratings, Wood noticed that when a grating's pitch was equal to integral multiples of illuminating wavelength, "there was a sort of destructive interference along the plane of the grating" [36]. Hessel and Oliner, further elaborating on the origins of Wood's Anomalies, have suggested both a Rayleigh wavelength anomaly (new emerging orders) and a guided complex wave supported by the grating (SPPs), which agrees with the findings of the NEC group [37].

In fact, other studies performed by the same group were able to generate detailed zero order transmission spectra over a full spectrum of angles and wavelengths, and were used to create dispersion diagrams, as seen in Figure II.14. These figures illustrate more clearly the transmission dependence on wavelength and angle but also $k_x$, the $x$

component of the wave vector. The wavelengths were varied from 200 nm to 3300 nm, while angles studies ranged up to 50°. These studies indicated that both Wood's Anomalies and SPP coupling caused by the repeated corrugations both played a role in the significant transmission enhancements.

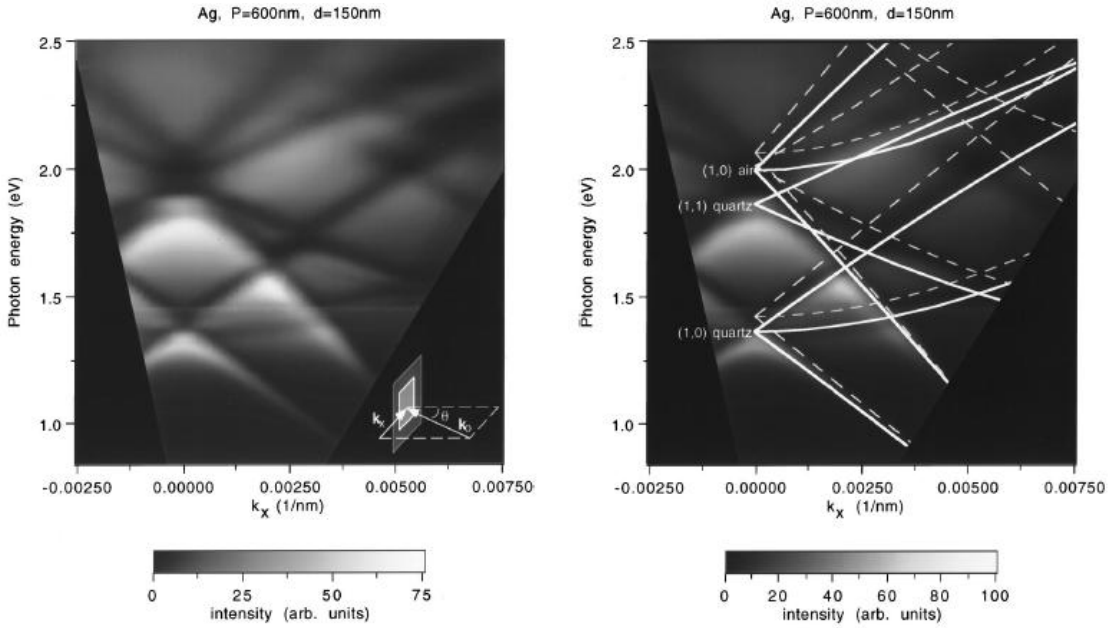


**Figure II.14: Dispersion relations generated for 150 nm diameter circular holes with a pitch of 600 nm, fabricated on a 200 nm thick Ag film. The right side diagram is identical, showing also overlaid curves for Wood's Anomalies (dashed lines) and SPPs (solid lines) [38].**

### (i) Composite Diffracted Evanescent Wave Model

Following the work of Ebbesen on the anomalous transmission on hole arrays, Lezec and Thio re-analyzed their previous theories on the role of SPPs in transmission and presented some revisions [39]. First the original perforated metal films were destructively analyzed and hole diameters measured larger than originally thought. New measurements were taken to relate power transmitted through the holes and collected in an objective to the total power incident on the opening of each hole. The power incident

on the opening of each hole of diameter $d$ is defined as $Q_0$. The power transmitted through the apertures and collected by an objective lens is defined as $Q_c(\lambda)$. The ratio of power transmitted through a single hole to the total power incident at the opening of that hole is defined as:

$$T = \frac{Q_c}{Q_0} \tag{2.57}$$

Considering an $N \times N$ array of holes, the ratio of the total collected power to the total incident power is then $\frac{T}{N^2}$. Using Fourier methods, the total power radiated from the array was calculated and defined as $Q_r(\lambda)$. This allows for the collection efficiency to be calculated as:

$$\gamma(\lambda) = \frac{Q_c(\lambda)}{Q_r(\lambda)} \tag{2.58}$$

Finally, the collection efficiency of the hole arrays could be used to calculate the transmission coefficient, defined as $T_{R,N}(\lambda)$.

$$T_{R,N}(\lambda) = \frac{1}{N^2}\frac{1}{\gamma_N(\lambda)}T \tag{2.59}$$

These new measurements gave enhancement factors for the hole arrays that were on the order of 7, much smaller than other reported enhancement factors. Re-considering existing claims, transmission enhancement and suppression seemed to occur around a baseline transmission spectra of a single isolated hole. Further, the case of transmission modulation in non-metallic systems was investigated. Reduced transmission was not linked to SPP modes, since only enhancement was predicted by the SPP resonant

coupling [39]. Hole arrays were fabricated in tungsten and $\alpha$-silicon substrates to test whether plasmons were necessary for enhancement, since in the visible regime, W is non-metallic and unable to support plasmons. Lezec discovered that the spectral dependence of the transmission coefficient was identical (to a multiplicative factor) to hole arrays fabricated in Ag, a well known plasmon-supporting material. The common transmission characteristics independent of material types suggested that plasmons were not central to enhancement.

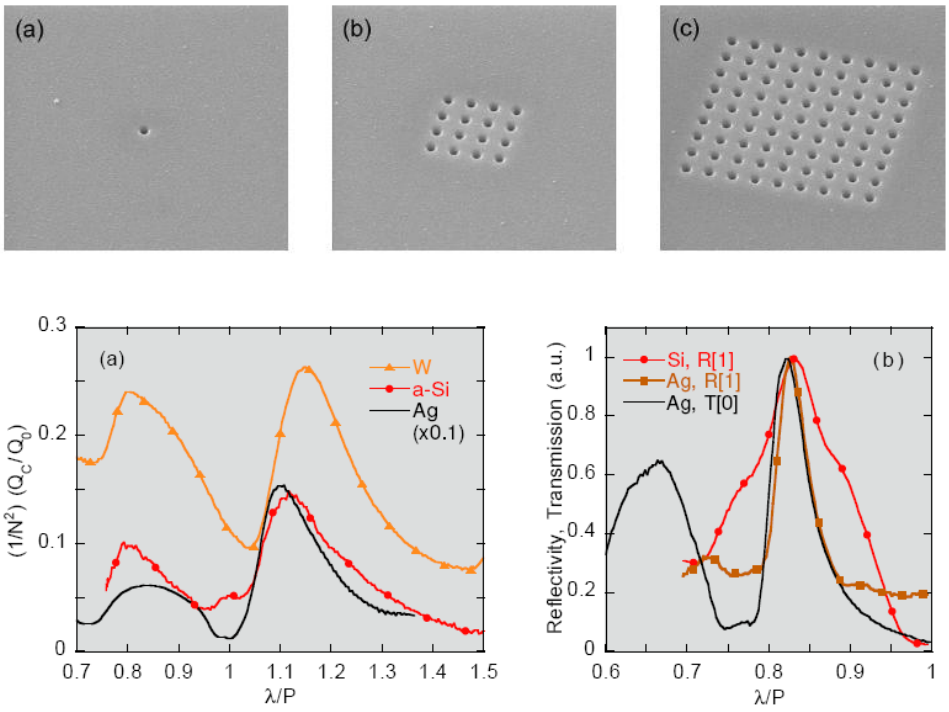


**Figure II.15: (Top Row) Hole arrays used for transmission measurements. Hole diameter is 300 nm, hole pitch is 600 nm. (Bottom Row) Collected normalized transmission spectra from hole arrays in different material systems [39].**

Considering these observations, Lezec and Thio proposed the Composite Diffracted Evanescent Wave (CDEW) model to explain the observed transmission enhancement. The CDEW model is based on interference of diffracted light, allowing for enhancement

and suppression in the same model. It models transmission as a multiplicative function including two modulation functions representing interference of evanescent waves and other effects on the front and back surfaces of the substrate. These front and back surface modulation functions are defined as $A_1(\lambda)$ and $A_2(\lambda)$, respectively. The total collected transmission coefficient of the hole arrays may then be calculated as:

$$T_c(\lambda) = A_1(\lambda) T_H(\lambda) A_2(\lambda) f_c(\lambda) \tag{2.60}$$

In Equation (2.60), $T_H(\lambda)$ explicitly takes into account the total intrinsic transmitted power of a single hole by including the evanescent mode. Also, $f_c(\lambda)$ is the fraction of the total transmitted power that is collected by the lens. The multiplicative form of the model dictates that when either the front of back surface modulation function is at a maximum, the transmission is also at a peak. Further, each modulation function can be defined as:

$$A_1(\lambda) = \left(1 + 2\sum_{j=1}^{N} \frac{\alpha d}{jP} \cos\left(\frac{2\pi}{\lambda} n_{\text{eff}}\, jP + \frac{\pi}{2}\right)\right)^2 \tag{2.61}$$

Both modulation functions take into account the number of holes, $N$, the effective refractive index experienced by the surface waves, $n_{eff}$, hole pitch, $P$, hold diameter, $d$, and a fitting parameter, $\alpha$, which adjusts amplitude. The effective refractive index is used here to adjust the refractive index from bulk values. This is necessary because the substrate is patterned with arrays of sub-wavelength holes which shift its refractive index slightly. The CDEW model was validated against a single 1-D slit surrounded by ion-milled grooves as shown in Figure II.16. The CDEW model better indicates the features observed in the collected power transmission spectrum, Figure II.16.

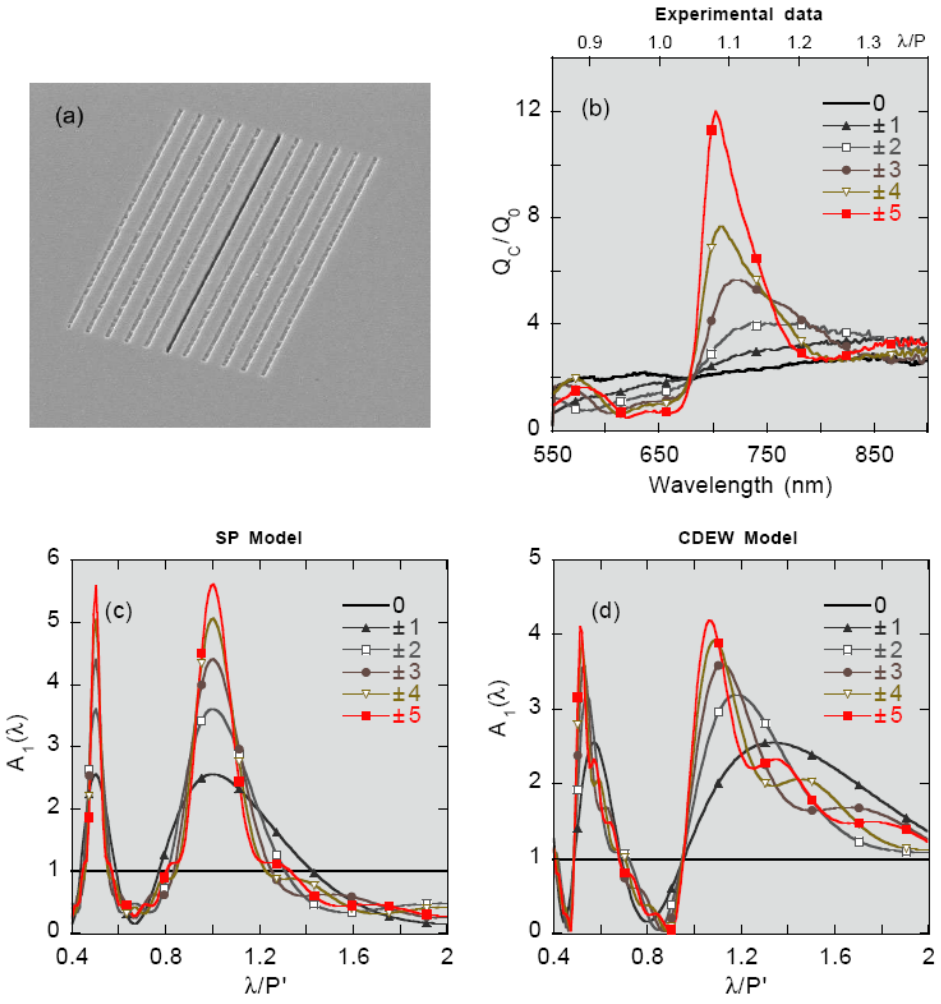


**Figure II.16: Experimental validation of the CDEW model vs. SPP model for amplitude modulation function and collected power efficiency [39].**

The CDEW model is not a complete description of the modulation phenomena, but rather a first order approximation, which tends to over-predict certain features of the curve. For instance, TM polarized light shows excellent agreement, while TE light does not [40-42]. Despite these questions, the model does highlight the role that evanescent waves and optical phenomena play in modulating slit transmission. Further work indicates the possibility of a two component model, both optical and plasmonic based [43], [44]. The optical component decays according to $1/\sqrt{x}$, while the SPP term decays typically much

slower, depending on the system under study, and is given by Equation (2.55). In this scenario, the measured electric field of the groove is considered with respect to the groove size and distance from the scattering site. The reasons for initial confusion of the two phenomena are many. If large length scales are used, for instance, the SPP term will dominate, however for small distances or less conductive substrates, the creeping wave (optical) terms will prevail, leading to different conclusions. By including both terms, the behavior in certain systems can be modeled more accurately. In general, the materials, wavelengths used, and layout of the structures plays an important role in the enhancement phenomena observed.

### G. Survey of Enhancement through Sub-Wavelength Apertures

Since Ebbesen's work on transmission enhancement through small holes [34], there has been a healthy debate in the scientific community over the phenomena responsible for such enhancement. The debate mainly involves the role of SPPs and the role of optical phenomenon in the observed transmission. These roles are related to the size and shape of the geometry studied, the wavelength ranges used and their relation to the hole sizes, and the materials used. The following is a review of some of the more significant studies to date, and their relationship to the phenomena discussed in previous sections.

Ebbesen's first report indicated a maximum transmission enhancement at 1.37 μm, using a 2-D array of holes milled in 200 nm thick Aluminum, Chromium, and Gold. Geometries studied varied but typically consisted of hole diameters from 150 nm to 1 μm, while hole pitches ranged from 600 nm to 1.8 μm [34]. One main conclusion of the work was that hole transmission at the peak exhibited transmission efficiencies that

exceeded theory by several orders of magnitude. Shortly after this pioneering work, Ghaemi, et al. performed a more detailed analysis of the Ag system with hole diameters and pitches of 150 nm and 600 nm, respectively [38]. They were able to perform a more detailed analysis of the physics behind the enhancement and found not only was the transmission efficiency approximately 1000 times higher than expected for the sub-wavelength holes, but they were able to map Wood's anomalies and SPP resonance conditions back to measured dispersion relations of zero order light (see Figure II.14). They found that the bright bands in the dispersion relation corresponded to locations on the SPP dispersion diagram for the Ag input surface. [38]. These views were further underscored in a separate study by Barnes, et al. [45]. A novel experiment that further emphasizes the role of SPPs in the transmission enhancement of hole arrays was performed by Devaux. Two arrays of holes were used, one as a detector of plasmons and another directly illuminated by light, as in Figure II.20.

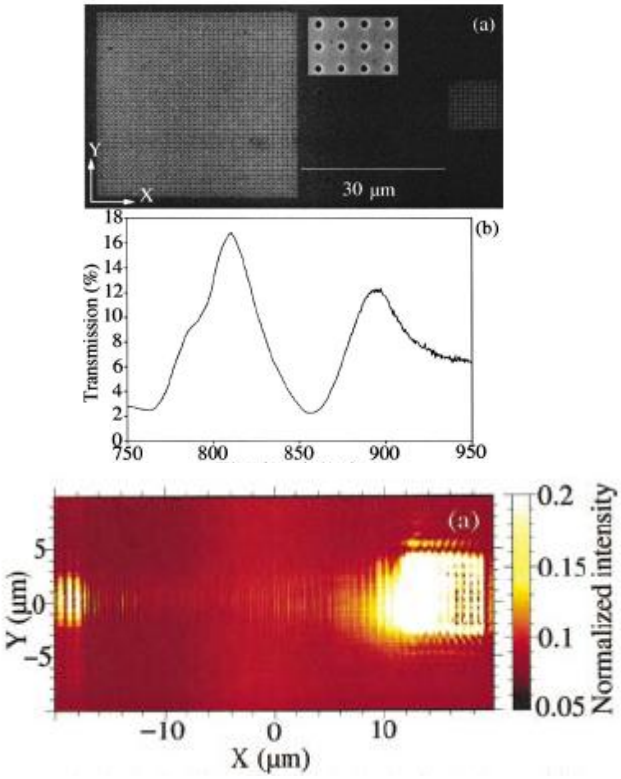


**Figure II.17: Surface plasmons are generated from incoming light using the smaller array on the right hand side, where they propagate across the metal and are re-converted to propagating light by the larger array on the left [46].**

Shortly after these results were published, new research conducted by Porto et al. used slightly different structures of a higher aspect ratio [47]. Their results agreed with Ebbesen and Ghaemi, however they were also able to show that for high aspect ratio slots it is possible to couple the incoming light to resonances in the slots themselves. The study revealed the importance of considering the specifics of the structure under test, since different physics may be occurring. The electric field for two such structures is shown in Figure II.18. Although the locations of the enhancement peaks shift depending on the type of resonance, similar transmission levels are achieved with either method.

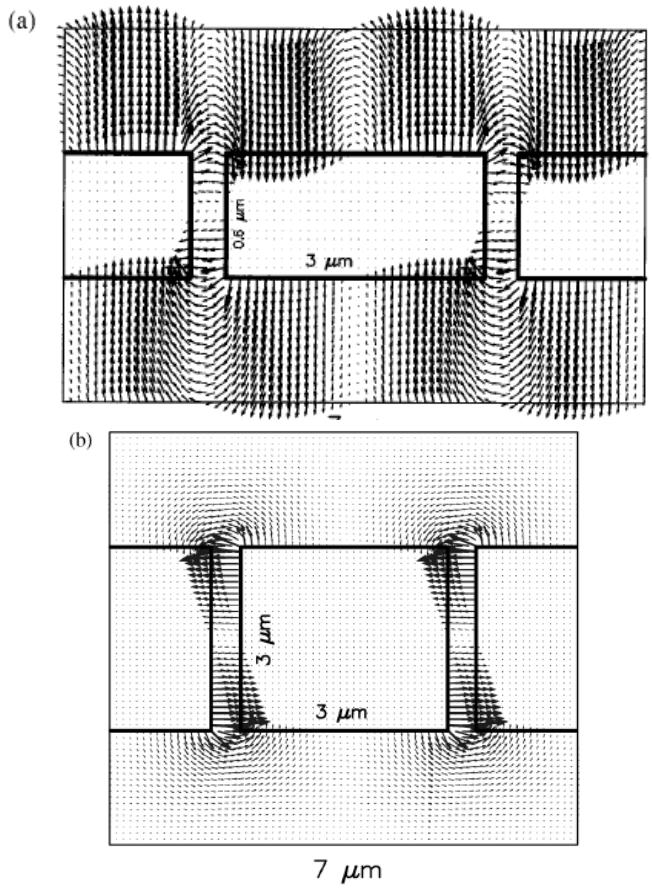


**Figure II.18: Electric field for two aspect ratio slot configurations. (a) shows that the surface modes dominate, while (b) demonstrates coupling to slot modes [47]. Pitch is 3.5 μm, slot width is 500 nm, and metal thickness is 600 nm and 3 μm.**

This type of enhancement mechanism was also observed by Cao and Lalanne, who re-examined the structure used by Porto, this time using Rigorous Coupled Waveguide Analysis (RCWA) [48], [47]. Their new investigation showed evidence that, for the case of high aspect ratio slots, the SPPs play a negative role in these systems.

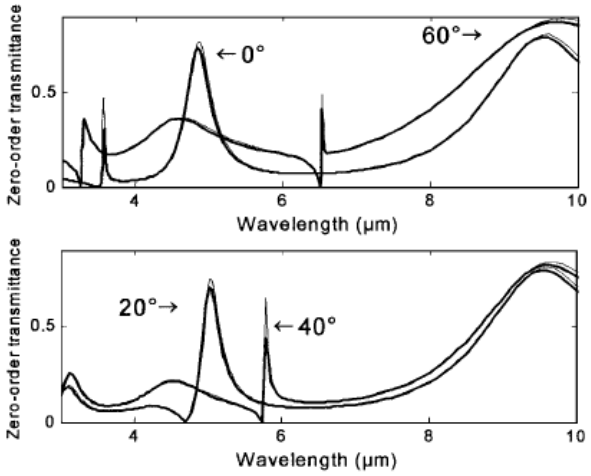


**Figure II.19: Zero order transmission spectra observed by Cao and Lalanne using an Au grating [48].**

In the gold case shown in Figure II.19, the transmission spectra is shown across several angles. By viewing the results across angles, Cao concluded that the sharp resonances correspond to so-called Rayleigh anomalies [48]. These are also known as Wood's Anomalies as described above, and correspond to conditions where $\sin\theta_m = \pm 1$ in Equation (2.21) [25], [48]. In fact, since the Rayleigh anomaly and SPP often lie close together, it is easy to confuse the two. Figure II.20 also shows zeros to the left of the sharp Wood's Anomalies that exactly match with SPP locations, evidence that the SPPs contribute to lack of transmission in this particular system [48].

Thio et al. performed a study where only a single transmitting hole was used in conjunction with surface relief patterns: circular bull's eye type structures, or square arrays of non-transmitting dimples [30]. Although these structures were slightly different than the transmitting features studied in 1998, their behavior with respect to wavelength was similar. They were also able to conclude that the maximum transmission corresponded to the coupling of incident light to an SPP mode, while minima correlated

with Wood's anomalies, in agreement with previous work on similar scale and aspect ratio structures.

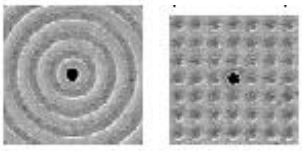

**Figure II.20: Single apertures surrounded by rings and arrays of dimples [30].**

A further elaboration into the nature of the surface plasmon polaritons arising from these structured surfaces is that they are in fact SPP Bloch Waves or SPP-BW. These SPP-BWs are created as a standing wave pattern and arise because of the plasmon's interaction with the periodic substrate.

Another interesting phenomenon is observed altogether when the length scale of features under study approaches $d<a<<\lambda_0$, where $d$ is the hole diameter, $a$ is the hole pitch and $\lambda_0$ is the vacuum wavelength of light used. When the holes and their pitch are much smaller than the wavelength of light, the material can be viewed using the Effective Media Approximation (EMA) [49], [50]. Using this approximation, even perfectly conducting materials can support spoof plasmons as long as holes or grooves exist, since it sufficiently modifies the dielectric function. Also, by tailoring the layout of the grooves or holes, the spoof plasmon dispersion can be tuned [49].

As discussed earlier, much of the plasmonic enhancement work occurs over different layouts. Table II.1 shows a summary of layout and illumination parameters from the above highlighted studies in an attempt to categorize their results.

| Researcher | Peak Wavelength (nm) | Dimension | Pitch (nm) | Hole Size (nm) | Absorber Thickness (nm) | Aspect Ratio (h/w) |
|---|---|---|---|---|---|---|
| **Ebbesen [34]** | 1370 nm | 2-D | 900 nm | 150 nm | 200 nm | 1.33 |
| **Ghaemi [38]** | ≈700 nm/950 nm | 2-D | 600 nm | 150 nm | 200 nm | 1.33 |
| **Thio [30]** | 800 nm | 2-D | 750 nm | 440 nm | 300+100 nm | 0.91 |
| **Porto [47]** | 3500 nm | 1-D | 3500 nm | 500 nm | 600 nm | 1.2 |
| **Salomon [51]** | 1420 nm | 2-D | 900 nm | 300 nm | 20 nm | 0.06 |
| **Cao [48]** | 4900 nm | 1-D | 3500 nm | 500 nm | 4000 nm | 8 |
| **Barnes [45]** | ≈700 nm | 2-D | 420 nm | 250 nm | 180 nm | 0.72 |
| **Chang [52]** | 640 nm | 2-D | 600 nm | 200 nm | 100 nm | 0.5 |
| **Flammer [53], [54]** | 852 nm | 1-D | 400 nm | 150/450 nm | 200 nm | 1.33 |
| **Lezec [39]** | 700 nm | 2-D | 410 nm | 150 nm | 175 nm | 1.16 |

**Table II.1: Wavelength and layout data for historic hole transmission enhancement studies.**

As Table II.1 shows, the bulk of the work was done with silver and gold films in regions where their SPP dispersions are favorable for large field enhancement. Also evident is that most studies used modest aspect ratio designs, except for Porto (not shown) and Cao. These studies also reach different conclusions than the others, namely that guided modes in the slots were responsible for enhanced transmission. Table II.1 also shows the illumination wavelength and pattern layout. Although in most cases a spectrum is used, here a representative wavelength is chosen where some peak transmission is located. Comparing the data, in all cases where large peaks are located, the wavelength is larger than the feature pitch. This indicates that although diffraction occurs, aside from the $0^{th}$

order there are no other propagating orders. Of course, for isolated structures, the transmitted fields cover all frequency components and expand radially. The scale of the periodic layouts also leads to the opening of "plasmonic bandgaps" as in [45], [47] which are similar to those arising from periodic structures in dielectrics such as in the field of photonics [55].

Other notable work pertains to coupling into and out of near fields using gratings. This further reinforces the reciprocity first noted by Leviatan. Fong and Hui used identical surface relief gratings on the top and bottom of a 120-130 nm thick silver substrate [56]. The gratings had a 1 μm pitch and the groove features were patterned to a depth of half the silver substrate, and their width was 50-200 nm. When illuminated with TM polarized illumination, the stacked gratings reveal unique transmission peaks that are strongest when the two gratings are misaligned. In other words, the fields must penetrate the metal in order to reach the opposite side. The authors were able to conclude that the enhanced transmission in this case comes from the SPP mode on the input surface coupling through the thinned metal region to the slot on the output side grating [56]. The output side grating can then take the transmitted field and convert it back to propagating light.

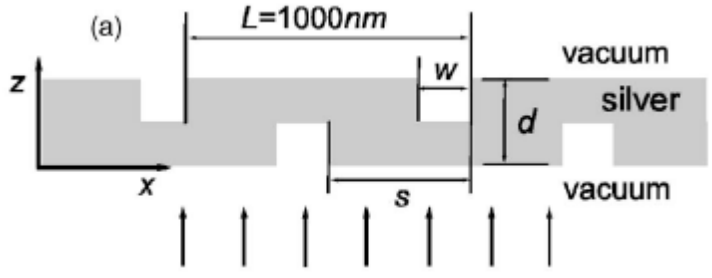


**Figure II.21: Schematic of shifted grating experiment performed by Fong and Hui [56].**

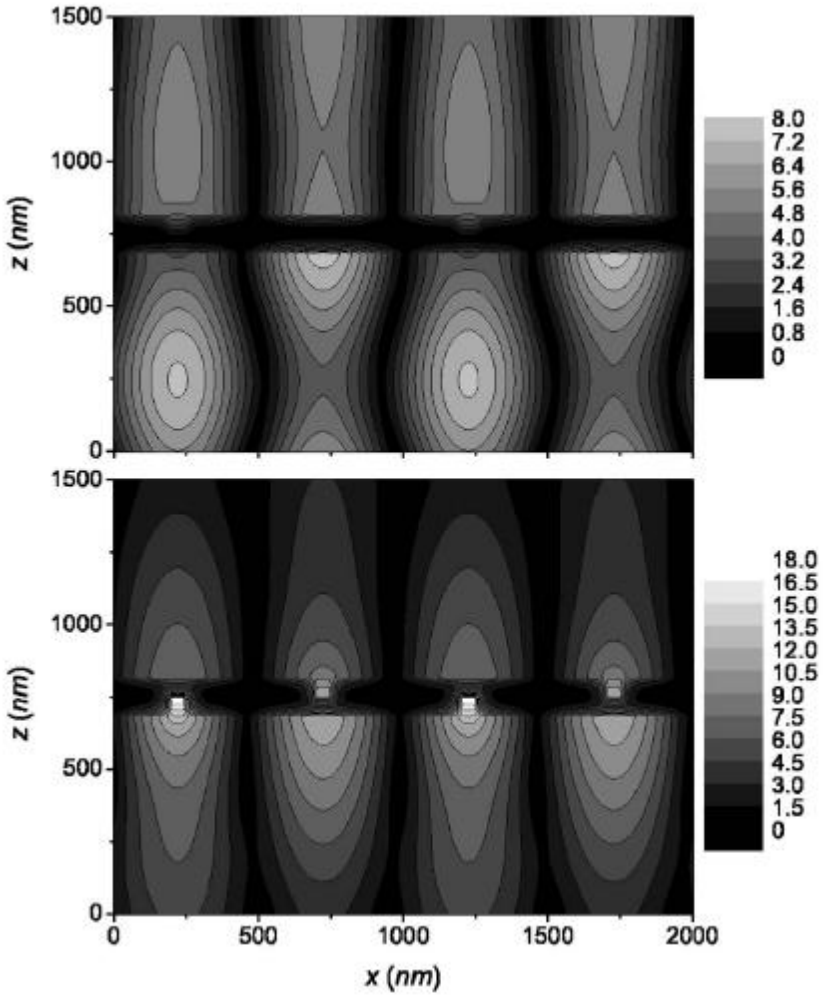


**Figure II.22: Magnetic field profiles for shifted gratings described in [56].**

Chan, et al. looked at stacked transmission grating structures in comparison to the surface-relief features of Fong. The structures consisted of aluminum gratings of 2 μm pitch with 400 nm slits, patterned in 410 nm thick aluminum. Although the structure is much different, they were able to conclude similarly that the transmission was largest when grating structures were misaligned by almost half of the pitch such that no direct line of sight existed between the two structures. A micrograph of the experiment is shown in Figure II.23. The dashed curve represents the single aluminum grating while the solid

curve represents the double layer grating with an offset of 0.9 µm. Although the enhancement is not as striking as in previous experiments, there is a clear effect caused by the addition of the second Al grating layer.

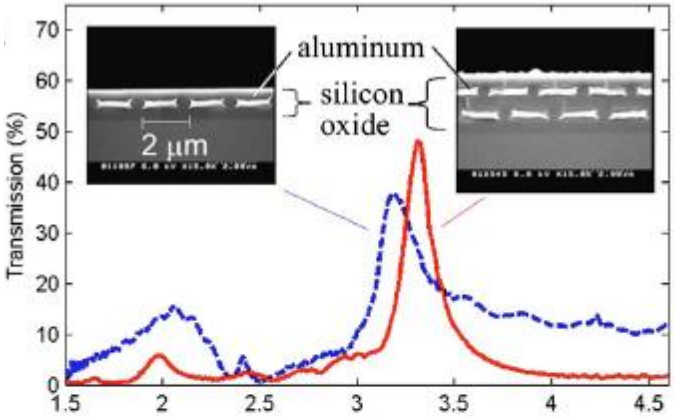


**Figure II.23: Micrographs and transmission output of transmission double-layer grating reported in [57].**

This chapter introduced key concepts such as evanescent waves and surface plasmon polaritons. It also provides background for evanescent modes on gratings and apertures. Key studies involving enhancement of intensity through sub-wavelength apertures are presented to provide context for EWAFs and their effects, and to highlight similarities and differences of the design from previous work.

# III. EVANESCENT WAVE ASSIST FEATURES

Evanescent Wave Assist Features (EWAFs) are small grooves adjacent to a transmitting periodic aperture in a photomask used for optical projection lithography, as shown in Figure III.1.

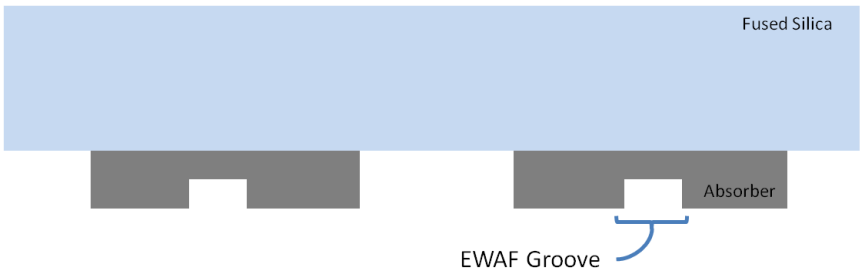


**Figure III.1: Illustration of evanescent wave assist features surrounding an aperture on a photomask.**

EWAFs are an extension of the "enhanced transmission" experiments summarized in Chapter II.F with several key differences. First, the wavelengths used are much smaller. Instead of operating in the visible or microwave regime, these photomasks are designed for the DUV spectrum. This has several material consequences that will be highlighted later. Second, the layout parameters used are no longer much smaller than the wavelength of illumination. In fact, the features often approach the wavelength scale, or are larger. Such is the case with the pitch of many of the patterns under test. This is required since the patterns create diffraction spectra to be used for imaging. Most studies to date have focused on enhancement through an isolated sub-wavelength hole or arrays of holes. When grooves or dimples have been employed, they are surrounding an isolated hole or slot. Since the wavelength is larger than the pitch of many of these patterns, discrete

orders are not produced. The main issue from the lithographic standpoint is not the total energy flowing through the periodic apertures, but the distribution of that energy into the orders and how that distribution is modified by the presence of the EWAFs.

This chapter will introduce the concept of Evanescent Wave Assist Features, and include schematics describing their layout and parameters discussed in this thesis. Since a large part of the investigation was performed using computer simulation, the finite-difference time-domain method will be described, followed by a description of the lithography and thin film stack simulation. The results of mask simulation will be presented and categorized based on design type as well as other design parameters for the EWAF grating. Using these results, the imaging performance from a mask employing EWAFs will be presented and compared to a standard binary reticle. The optimized EWAF solution will also be compared to performance gains offered by an optimized attenuated phase shift mask.

### A. Layout

The idea of non-transmitting grooves surrounding an aperture on a photomask was briefly presented in Chapter I. Here, details on the EWAF layout will be presented. A standard binary photomask or reticle consists of a UV-grade fused silica substrate coated with an absorber. The absorber is often an anti-reflective chromium, chromium nitride, and chromium oxide composite film and has a thickness of near 100 nm [58]. The absorber has continuously varying optical constants over this thickness, however the bulk of the film can be considered a CrON understoichiometric mixture. For simplicity in analysis, a simple absorber model using a single Cr film was used in some of these studies. Figure III.2 illustrates schematically EWAFs located at the absorber/silica

interface, also called top-side features, and the absorber/air interface, also called bottom-side features. These comprise the two categories of EWAFs investigated in this thesis.

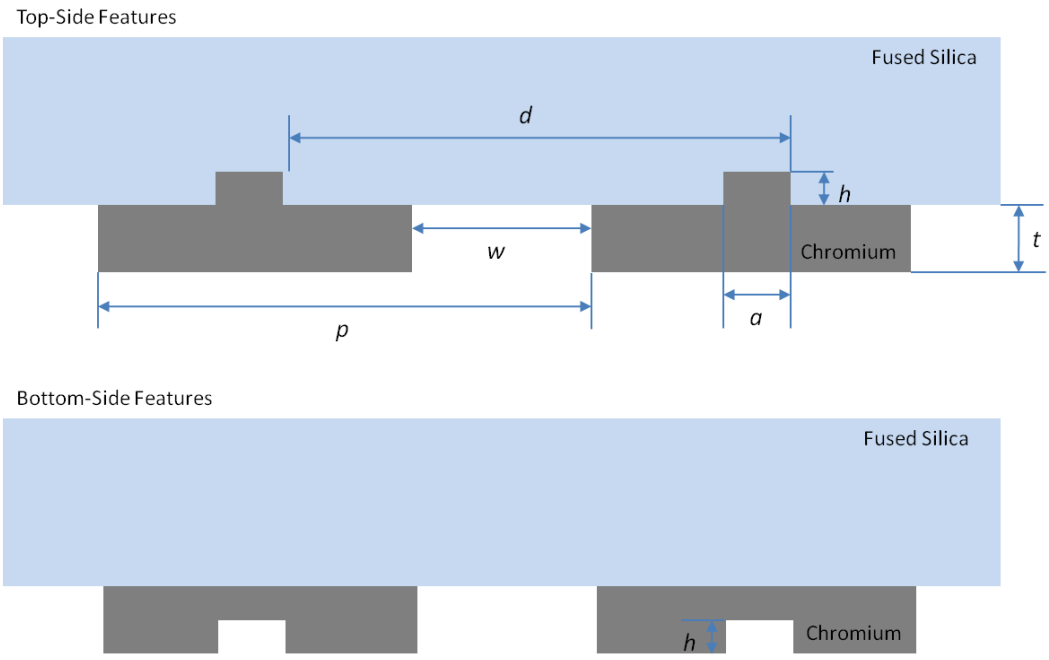


**Figure III.2: Schematic of top and bottom-side EWAF layouts. Both domains are periodic. Main feature pitch is *p*, CD is *w*, *d* represents the EWAF feature pitch, *a* represents the width of the EWAF notch, *t* represents the planar absorber thickness, and *h* represents the notch depth or height depending on design type.**

Both top- and bottom-side layouts have the same layout parameters, which will be used to reference these features throughout the rest of this work. The pitch of the main transmitting features is parameterized as *p*, while the Critical Dimension (CD) of the main feature is represented by *w*. Absorber thickness is considered in the absence of EWAF modulation and is represented by *t*. EWAF pitch is represented by *d*, while EWAF CD is parameterized as *a*. EWAF height or depth for top- and bottom-side layouts, respectively, is represented by the parameter *h*. Representative mask dimensions for these layouts are *w*=180 nm, *t*=90 nm, *h*=30 nm, *a*=120 nm and *d*=*p*=600 nm.

Both top-side and bottom-side EWAF layouts require a two-step lithography process to fabricate. The first lithography step defines the regions that will be etched to define the EWAFs, while the second lithography defines the transmitting main features and must be carefully aligned to the first exposure. A combination of both top and bottom EWAF features is not considered in this work, since fabrication would require three separate patterning steps and is infeasible. The fabrication process will be discussed in more detail in Chapter IV. Fabrication of such structures is time-consuming and challenging, therefore numerical modeling was used as a screening tool to determine ideal layout dimensions and mask responses to illumination.

Experiments have been performed at $\lambda_0$=193 nm and 248 nm. The latter wavelength choice increases the minimum size requirements and makes fabrication of a test device less complicated while still using similar physics and wavelength scales. These slightly larger dimensions also bring the fabrication specification to within range of those possible at the RIT Semiconductor and Microsystems Fabrication Laboratory (SMFL).

### B. Thick Mask Modeling

Both top and bottom side layouts involve features which are buried under or above the mask absorber. This makes simulating their effect complicated, since rigorous techniques must be applied. Typical lithographic simulation applies Kirchhoff boundary conditions, which assume that the mask absorber is completely opaque. These boundary conditions also state that the electric field and its derivative directly below the absorber are both zero, and the fields in transmitting apertures of the mask are the same as they would be in absence of the absorber [59]. Assuming that the input field to the problem is

a uniform plane wave of unity amplitude, the boundary conditions allow for convenient analysis of the problem using a Fraunhofer Approximation. The Fraunhofer approximation used here allows the diffracted orders to be determined (up to a multiplicative phase factor of $(x,y)$) by a Fourier transform of the mask function and is valid here based on the small illumination angles present at the mask plane, as well as the large observation distance of the pupil plane from the reticle [59]. In this particular case with buried features, as well as for masks with significant topography (shadowing), these simulations are not accurate and the mask fields must be determined rigorously, using either Rigorous Coupled Waveguide Analysis (RCWA), Finite-Difference Time-Domain (FDTD), or Finite Element Method (FEM) techniques [60-64].

The FDTD method is the preferred choice in this particular application because of ease of use, Bloch boundary conditions and Perfectly Matched Layers (PMLs), support for dispersive linear isotropic materials, and scripting capability [65]. In addition, FDTD is a standard method and well trusted in many disparate fields. There are a number of references that detail operation of FDTD algorithms including [66], [67], and [68]. Only a high-level explanation will be given here in order to introduce the basic principles.

In general, FDTD algorithms apply a grid to an arbitrary layout. The gridding operation defines the material properties for that particular cell, and discretizes the layout to match the grid. Time dependent Maxwell's equations are also discretized using finite differences in place of the partial temporal and spatial derivatives. These finite differences are then solved in a "leapfrog manner"; at integer time steps, the method solves for electric fields, while at integer +½ time steps, the magnetic fields at all points in the grid are solved [67]. This iterative stepping technique goes on until the excitation

pulse is extinct and the domain converges, meaning no more changes in the fields are happening, to within some defined convergence criteria. Because of the iterative technique, problems can be solved where no closed form analytical solution exists.

A typical simulation domain is illustrated in Figure III.3, showing PML's, Bloch boundaries, input excitation (plane wave in upper half-space), frequency domain output monitor (dashed line in lower half-space), and time monitor (X in lower half-space).

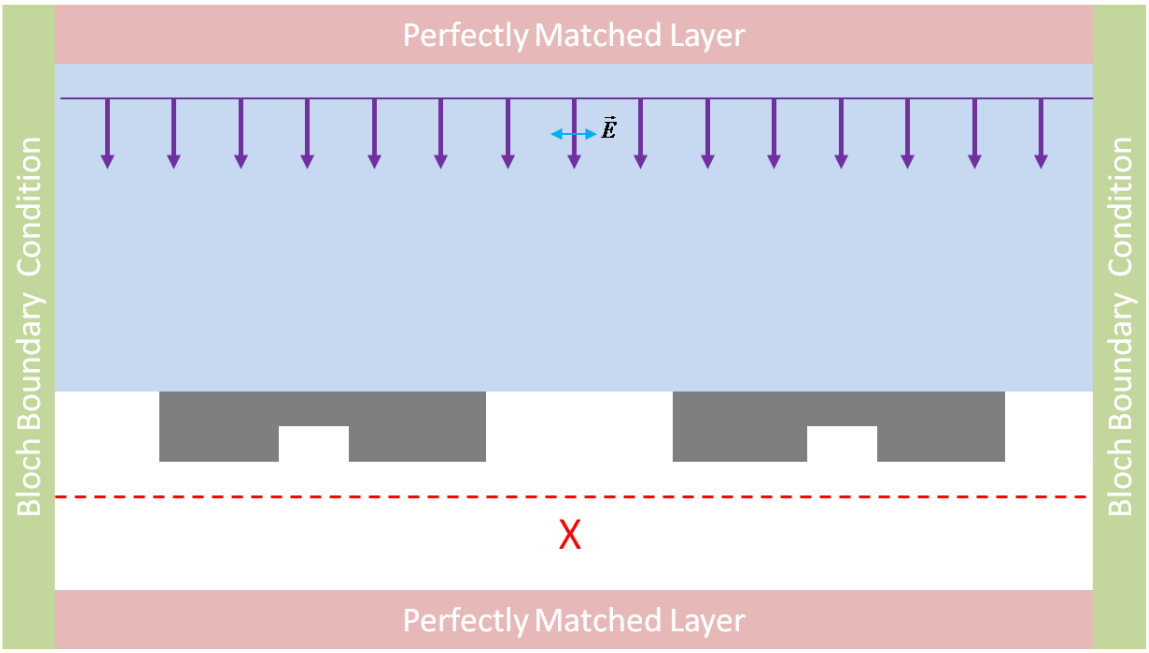


**Figure III.3: Schematic of a typical simulation domain.**

Perfectly matched layers are one of the major advances in FDTD methods in the last 20 years. In order to get good simulation accuracy, it is essential that the small domain simulation accurately describe the real world it is attempting to model. PMLs are non-physical materials added to the domain with the special property of absorbing incoming radiation without reflection for all frequencies and angles of incidence. In other words, they allow radiation to exit the domain without being reflected. The top PML absorbs

reflections from the top of the metal absorber, while the bottom PML absorbs radiation scattered forward from the photomask.

Bloch boundaries are a special case of periodic boundary conditions. Periodic boundary conditions require that the fields across a matching pair of boundaries are equal, as they would be if the domain was simulated across many periods. Standard periodic boundaries are only accurate for normally incident plane waves since they do not take into account the phase of plane waves with non-normal incidence. Bloch boundaries are used for single-frequency plane waves to model these phases and arrive at accurate simulations.

As in [67], the photomask under simulation is regarded as an object that takes a plane wave and scatters it into many plane wave components. A single plane wave at a given angle is used as the input excitation to the domain in Figure III.3. The scattered plane waves are collected at the frequency domain monitor below the mask absorber. The field components and power flow can be collected, however the electric field is of primary interest in this case. The output from the frequency domain monitor is the near-field electric field components that will be used in further simulation. To aid in convergence checking, a time-domain point field monitor is included in the domain. This will display the fields with respect to time of simulation. If the PMLs are working properly, the point monitor will show the field increasing through the excitation pulse and then damping as the radiation leaves the domain. Once the system has converged, the time domain monitor can automatically end the simulation, eliminating wasted iterations.

If the fields are known across a simulation plane, they can be projected to any point in the half space below that surface. In this case, the fields are known along the line

output monitor and the far field projection from these known near-fields can be made. Since the domain is periodic, discrete diffraction orders are projected from the monitor as a function of angle into the half-space. These complex orders and their propagation angle are shown pictorially in Figure III.4.

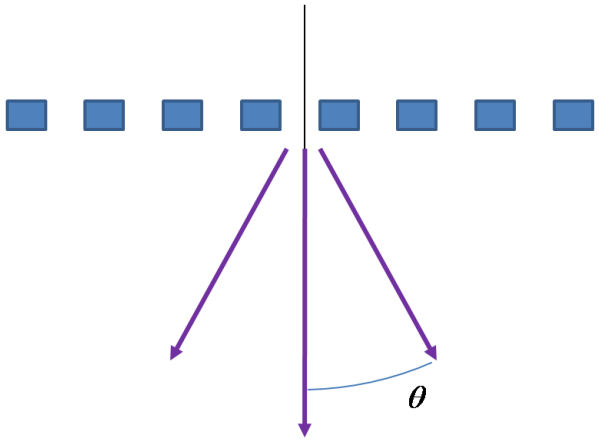


**Figure III.4: Diffraction orders vs. angle leaving the photomask.**

The mask side frequency of a diffraction order can be calculated from this angle via Equation (3.1). Here $f_x$ represents the spatial frequency of the diffraction order, $\theta_x$ is the angle of the order in question, $n$ is the index of the medium the order is propagating in, $\mathrm{NA}_x$ is the Numerical Aperture (NA) space location of the order, and $\lambda$ is the illumination wavelength.

$$f_x = \frac{n \sin \theta_x}{\lambda} = \frac{\mathrm{NA}_x}{\lambda} \tag{3.1}$$

The fields are cast in cylindrical coordinates for convenience. For TM or *p* polarized simulations, the electric field is uniquely in the tangential component $\theta$ while for TE or *s* polarized simulations, the field will be uniquely in the *y* component. With the

electric fields conveniently in one component, the optics of the reduction scanner can be simulated.

### C. Lithography Simulation

The optics of scanners collect diffracted order from the photomask, filtering those orders to include only those that reside inside of the pupil, applying a reduction (typically 4X), and delivering reduced, filtered, scattered plane waves to the film stack for recording. All of the features on the photomask must be sized at 4X larger than the intended printing size on the wafer to get accurate interactions of the incoming plane waves with the mask. Magnification has a multiplicative relation with NA:

$$\begin{aligned} \mathrm{NA}_{xw} &= M\mathrm{NA}_{xm} \\ n_w \sin\theta_{xw} &= M n_m \sin\theta_{xm} \end{aligned} \tag{3.2}$$

In Equation (3.2), the subscripts *xw* and *xm* indicate the NA or angle of a particular order on either the wafer or mask side. The demagnification factor, *M* represents the reduction ratio of the exposure tool. Also, the NA on the wafer side of the imaging system scales in relation to the magnification, and the plane wave angles can be calculated based on Equation (3.2). Typically, the NA of the tool is defined at the imaging plane and the NA on the mask side is much lower. The plane waves can then be filtered based on the NA of the system. Since each plane wave coming from the mask can be assigned a wafer-side $\mathrm{NA}_x$ value, these can be filtered using Equation (3.3) for the ideal pupil function, where NA represents the maximum NA of the system.

$$P_{\text{ideal}}\left(f_x\right) = \begin{cases} 1, & f_x \le \mathrm{NA}/\lambda \\ 0, & f_x > \mathrm{NA}/\lambda \end{cases} \tag{3.3}$$

There is also a radiometric correction that should be used in reduction imaging due to conservation of energy [8]. The reduction design of the lens causes the energy entering the pupil to be distributed differently at the lens output. The radiometric correction, Equation (3.4), accounts for this difference and corrects for it across the spatial frequency domain of the pupil. Equation (3.4) is an approximate relation that holds when the reduction ratio of the objective lens is 4 or higher.

$$P_{\text{rad}} = \left(1 - \frac{\lambda^2 f_x^2}{n_w^2}\right)^{-0.25} \tag{3.4}$$

The pupil function of an aberration free system can then be calculated by Equation (3.5).

$$P(f_x) = P_{\text{rad}}(f_x) P_{\text{ideal}}(f_x) \tag{3.5}$$

The complex electric fields of the plane waves converging at the image plane are then given by Equation (3.6) and shown in Figure III.5. Here $\vec{E}_{w,\text{tot}}(f_x)$ represents all unfiltered plane wave components leaving the reticle, with angular distribution scaled to the image plane.

$$\vec{E}_w(f_x) = \vec{E}_{w,\text{tot}}(f_x) P(f_x) \tag{3.6}$$

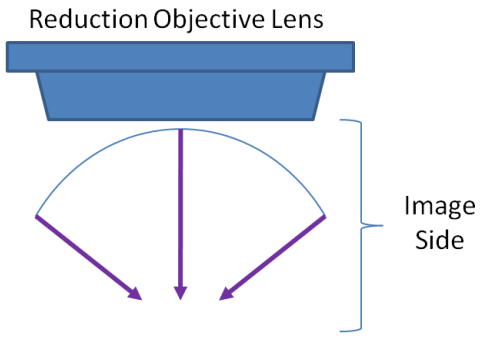


**Figure III.5: Converging, filtered plane waves on the output side of a lithographic reduction lens.**

### D. Film Stack Modeling

The converging plane waves then enter the thin film stack, which is typically comprised of a topcoat, photoresist, Bottom Anti-Reflective Coating (BARC) and substrate. The multiple films and angles of the plane waves result in beams that are multiply reflected and transmitted throughout the film stack. Accurate simulation of refraction in photoresist and the film stack is especially critical for TM polarized light, since there is an angularly dependent demodulation that occurs because of the two electric field components that exist [69]. These multiple reflections can be accurately described using the matrix methods described by Macleod [70] and have been used by several authors, including [71] and [72]. The layout of the isotropic thin films is described in Figure III.6. The angle of each diffraction order in each film can be calculated using Snell's law, Equation (2.1).

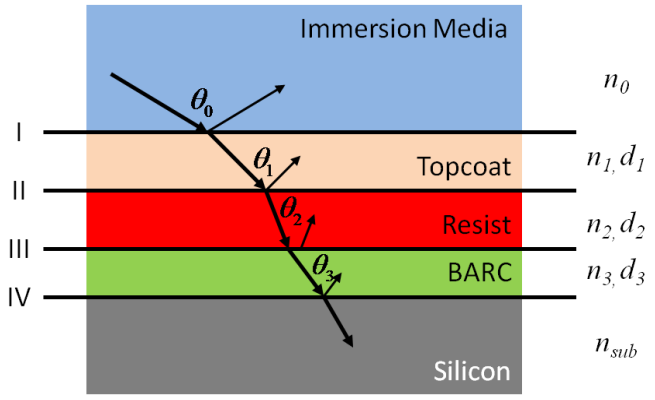


**Figure III.6: Imaging film stack illustrating refractive index, *n*, interface scheme, and thickness, *d*, of each layer.**

Each film in the stack of Figure III.6 can be conveniently described using the characteristic matrix of Equation (3.7).

$$M_j = \begin{bmatrix} \cos\delta_j & i\dfrac{\sin\delta_j}{\eta_j} \\ i\eta_j \sin\delta_j & \cos\delta_j \end{bmatrix} \tag{3.7}$$

In the characteristic matrix, the term $\delta_j$ represents the phase factor and $\eta_j$ represents the oblique optical admittance for the $j^{th}$ film. These are defined as:

$$\eta_j = \frac{n_j}{\cos\theta_j} \text{ for TM polarization} \tag{3.8}$$

$$\delta_j = \frac{2\pi d_j n_j \cos\theta_j}{\lambda} \tag{3.9}$$

The top layer of the stack, $j$=0, and the substrate, $j$=sub, also have optical admittances that are calculated via Equation (3.8). The terms $B$ and $C$ are calculated using the equation:

$$\begin{bmatrix} B \\ C \end{bmatrix} = \left( \prod_{j=1}^{q} M_j \right) \begin{bmatrix} 1 \\ \eta_{\text{sub}} \end{bmatrix} \tag{3.10}$$

Using the $B$ and $C$ values, the amplitude reflection and transmission coefficients can be calculated as:

$$\tau_x = \frac{2\eta_0}{B\eta_0 + C} \tag{3.11}$$

$$r_x = \frac{B\eta_0 - C}{B\eta_0 + C} \tag{3.12}$$

It is worth noting in Equation (3.11) and (3.12) that these coefficients represent the transmission through the entire film stack under consideration. Selecting different films as the "starting film" and recalculating the $B$ and $C$ parameters and $\eta_0$ (for the new starting film) will yield reflection and transmission coefficients for different permutations

of the film stack. The *x* subscript in (3.11) and (3.12) indicates that for TM polarization, these represent the coefficient for the *x* (lateral) component of the electric field. The *z* component coefficients are not continuous across film boundaries. Since the *z* component is orthogonal to *x*, it must be treated separately. The coefficients can be calculated by applying Maxwell's equations in source-free media, requiring (as in [71]):

$$\nabla \cdot \vec{E} = \vec{k} \cdot \vec{E} = 0 \tag{3.13}$$

The amplitude coefficients $r$ and $\tau$ are defined with respect to the fields incident on the first interface, and leaving through the last interface. For the entire stack, these are defined as:

$$r_{x,\mathrm{TM}} = \frac{E_{rx,\mathrm{I}}}{E_{ix,\mathrm{I}}} \tag{3.14}$$

$$\tau_{x,\mathrm{TM}} = \frac{E_{tx,\mathrm{IV}}}{E_{ix,\mathrm{I}}} \tag{3.15}$$

Using Equation (3.13), the transmission coefficients for the *z* polarized electric field component can be calculated.

$$r_{z,\mathrm{TM}} = -\frac{E_{rx,\mathrm{I}}}{E_{ix,\mathrm{I}}} = -r_{x,\mathrm{TM}} \tag{3.16}$$

$$\tau_{z,\mathrm{TM}} = \frac{\sin\theta_t \cos\theta_i E_{tx,\mathrm{IV}}}{\sin\theta_i \cos\theta_t E_{ix,\mathrm{I}}} = \frac{n_i \cos\theta_i E_{tx,\mathrm{IV}}}{n_t \cos\theta_t E_{ix,\mathrm{I}}} = \frac{n_i \cos\theta_i}{n_t \cos\theta_t}\tau_{x,\mathrm{TM}} \tag{3.17}$$

Considering the full stack, the field transmitted across boundary IV can be calculated. This result can then be used in subsequent matrix permutations to back calculate the fields incident on interfaces II and III. After the incident fields are known, the same

matrices can calculate the reflected fields from each interface. The matrix method automatically accounts for all interference effects and standing waves that happen throughout the thin film stack under consideration. Now the incident and reflected fields at each interface in the stack are established for each field component.

The image formed in the photoresist, layer 2, can now be considered. Some plane in the resist can be established as $z$=0, as in Figure III.8.

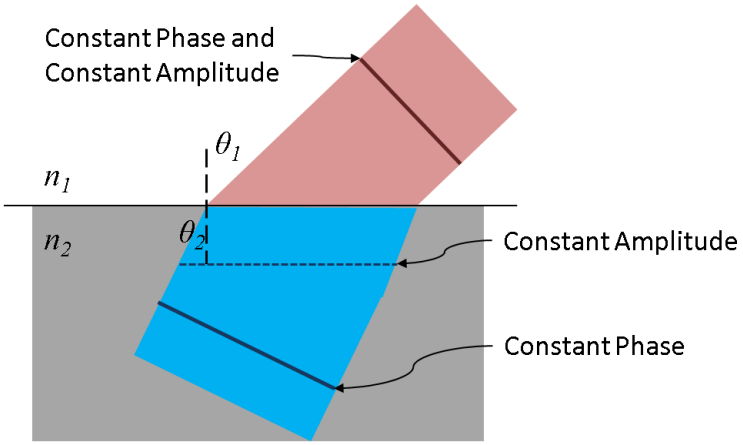


**Figure III.7: Transmission into an absorbing medium. Refractive index $n_2$ is complex and causes the constant amplitude and phase planes to split.**

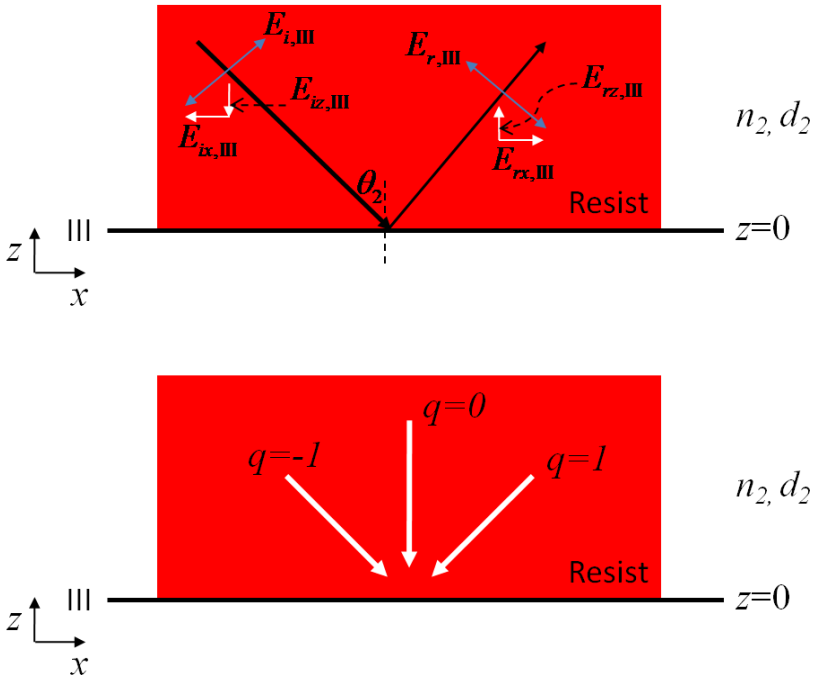


**Figure III.8: Top: Electric field components for calculation of the in-resist image. Bottom: Plane wave components and *q* labels, as used in Equations (3.19) and (3.20).**

At this plane, the resist image will be in perfect focus (ignoring induced spherical aberration caused by the planar film stack). The field from the plane waves can be mapped out in the photoresist as a sum of the incident and reflected plane waves calculated from the matrices. The phase for a plane wave in the slightly absorbing resist is given by

$$\phi_q = \frac{2\pi}{\lambda}\left( \mathrm{Re}\left[n_{\mathrm{III}}\right]\left(z\cos\theta_{q,\mathrm{III}} - x\sin\theta_{q,\mathrm{III}}\right) + i\frac{zk_{\mathrm{III}}}{\cos\theta_{q,\mathrm{III}}}\right) \tag{3.18}$$

where $k$ is the imaginary part of the complex refractive index and $q$ represents the particular diffraction order the phase term will be calculated for. Inserting this phase term along with the calculated electric field, gives the total electric field for each component, across all plane waves in the photoresist:

$$E_{x,\mathrm{tot}} = \sum_{-q}^{q} \begin{aligned} & E_{ixq,\mathrm{III}} \exp\left[ i\frac{2\pi}{\lambda}\left( \mathrm{Re}\left[n_{\mathrm{III}}\right]\left(z\cos\theta_{q,\mathrm{III}} - x\sin\theta_{q,\mathrm{III}}\right) - i\frac{zk_{\mathrm{III}}}{\cos\theta_{q,\mathrm{III}}}\right)\right] \\ & + E_{rxq,\mathrm{III}} \exp\left[ -i\frac{2\pi}{\lambda}\left( \mathrm{Re}\left[n_{\mathrm{III}}\right]\left(z\cos\theta_{q,\mathrm{III}} + x\sin\theta_{q,\mathrm{III}}\right) + i\frac{zk_{\mathrm{III}}}{\cos\theta_{q,\mathrm{III}}}\right)\right] \end{aligned} \tag{3.19}$$

$$E_{z,\mathrm{tot}} = \sum_{-q}^{q} \begin{aligned} & E_{iz,\mathrm{III}} \exp\left[ i\frac{2\pi}{\lambda}\left( \mathrm{Re}\left[n_{\mathrm{III}}\right]\left(z\cos\theta_{q,\mathrm{III}} - x\sin\theta_{q,\mathrm{III}}\right) - i\frac{zk_{\mathrm{III}}}{\cos\theta_{q,\mathrm{III}}}\right)\right] \\ & + E_{rz,\mathrm{III}} \exp\left[ -i\frac{2\pi}{\lambda}\left( \mathrm{Re}\left[n_{\mathrm{III}}\right]\left(z\cos\theta_{q,\mathrm{III}} + x\sin\theta_{q,\mathrm{III}}\right) + i\frac{zk_{\mathrm{III}}}{\cos\theta_{q,\mathrm{III}}}\right)\right] \end{aligned} \tag{3.20}$$

The final resulting intensity throughout the resist film is then:

$$I_{\mathrm{resist}} = \left|E_{x,\mathrm{tot}}\right|^2 + \left|E_{z,\mathrm{tot}}\right|^2 \tag{3.21}$$

Equation (3.21) is the resist image from a single plane wave illuminating the reticle. For partially coherent illumination, an envelope of plane waves must be considered. In this case, the individual coherent images can be summed in intensity to get the final image recorded in the photoresist.

$$I_{\mathrm{resist,tot}} = \sum_{\text{plane waves}} I_{\mathrm{resist}} \tag{3.22}$$

### E. Quality Metrics

This section introduces the metrics used throughout the remainder of this thesis for analyzing the lithographic impact of Evanescent Wave Assist Features. To isolate effects arising purely from the mask from those where the lithographic tool plays a role, masks with EWAFs are analyzed using diffracted orders in absence of projection imaging systems in Section (i). Combined effects from both mask and projection system are also considered using the metrics defined in Section (ii).

### (i) Reticle

To measure the effect of EWAFs, the enhancement factor is used for comparing the diffracted orders from a reticle with EWAFs to a reference reticle without. For these types of comparison, all transmitting feature sizes, pitches, material thicknesses and types are held constant (*w*, *p*, and *t* from Figure III.2, respectively).

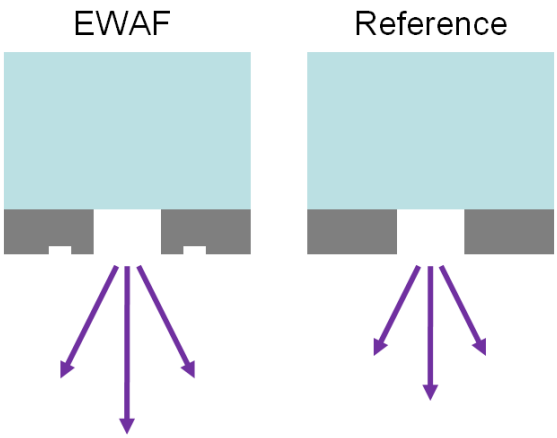


**Figure III.9: Diffracted orders from a reticle including EWAF features and a reference reticle.**

The diffracted order enhancement factor is defined here as:

$$0^{\text{th}}\ \text{Order Enhancement} = \frac{\left|E_0^{\text{EWAF}}\right|}{\left|E_0^{\text{ref}}\right|}$$
$$1^{\text{st}}\ \text{Order Enhancement} = \frac{\left|E_1^{\text{EWAF}}\right|}{\left|E_1^{\text{ref}}\right|} \qquad (3.23)$$

Equation (3.23) has the advantage that many mask pitches, materials, EWAF grooves, and space CDs can be screened independently of the particular imaging tool. This isolates mask effects from those that may arise due to choices in illumination and film stack.

### (ii) Aerial Image in Resist

To measure the effect the EWAFs have on a particular aerial image, the contrast improvement and NILS improvement are used. Similar to the order enhancement metric defined above, both of these compare aerial images at best focus, formed from two identical imaging systems and masks (except for the inclusion of EWAFs).

Image contrast (or modulation, as used in Chapter I) is determined by the maximum intensity in a space region of an image, vs. the minimum intensity in a line or other opaque feature. The image contrast is defined as:

$$\mathrm{M} = \mathrm{Contrast} = \frac{I_{\max} - I_{\min}}{I_{\max} + I_{\min}} \tag{3.24}$$

For the best possible case of having zero intensity in dark region of the image, the contrast will be unity. Contrast is mainly useful for analyzing images near resolution limits, since large patterns will often have high contrast regardless of their quality [8]. Contrast is generally related to Depth of Focus (DOF) since contrast decreases as the image goes out of focus. A high contrast image at best focus can tolerate more defocus before reaching a minimum useable contrast.

Another image quality metric that will be used throughout this thesis is the Image Log Slope, or ILS.

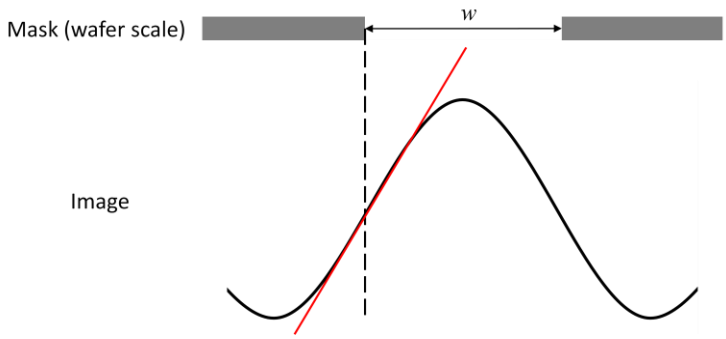


**Figure III.10: The NILS is calculated from the log slope of the image at the mask edge, and normalized to the feature width, *w* [8].**

Image Log Slope is the log slope of the image intensity profile, taken at the edge of the photomask. Often this is scaled by the width of the feature, *w*, for comparison with other features. This is known as the Normalized Image Log Slope (NILS).

$$\begin{aligned} \text{ILS} &= \left| \frac{d \ln(I)}{dx} \right| \\ \text{NILS} &= \left| w \frac{d \ln(I)}{dx} \right| \end{aligned} \tag{3.25}$$

NILS is also directly related to the Exposure Latitude (EL) of a process [8]. For an infinite contrast photoresist, the NILS is approximately related to CD change with respect to exposure dose, *E*, as:

$$\frac{\partial \ln E}{\partial \ln \text{CD}} = \frac{1}{2} \text{NILS} \tag{3.26}$$

The percent of EL for the same high contrast resist (assuming required CD control of ±10% of nominal) can be directly related to the NILS as:

$$\%\ \text{Exposure Lattitude} \approx 10 \times \text{NILS} \tag{3.27}$$

Equation (3.27) assumes a linear region where NILS is measured and is not accurate when the nominal line or space edge lies on a region of the profile with rapidly changing slope.

### F. EWAFs on 2-Dimensional Layouts

Evanescent Wave Assist Features were initially explored in the near field in order to test their applicability to photomasks. Extending some of the work presented in Chapter II, a photomask could be modified to include buried grooves etched into the mask substrate. An initial test using a four-film approximation to an AR-Cr film stack was used as a screening experiment to gauge the impact of these features. The film stack's layers increase their percentage of $CrO_x$ and decrease their concentration of Cr with increasing distance away from the fused silica substrate [58]. They are modeled as a uniform EMA layer based on their constituent components. Refractive index and thickness of each layer used for this initial experiment is shown in Table III.1.

| | **Layer 1** | **Layer 2** | **Layer 3** | **Layer 4** |
|---|---|---|---|---|
| **n** | 0.8209 | 1.5649 | 1.6740 | 1.7782 |
| **k** | 1.1825 | 0.4121 | 0.3597 | 0.1348 |
| **Thickness (nm)** | 50 | 13.3 | 13.3 | 13.3 |

**Table III.1: Refractive index data and thickness for AR-Cr at 193 nm [58].**

The layout used for this initial study was a 260 nm contact ($w$) at 1600 nm pitch ($p$). The simulation was performed using a 193 nm, normally incident plane wave. Two EWAF features were included in each simulation (except for the zero case) to investigate their impact on near-field image quality. The EWAFs were etched into the substrate a distance corresponding to a $\pi$ phase shift in glass ($h$). Their duty ratio is 1:1 depending on their width ($a$), which was varied from 20 nm to 120 nm. The structures differ from those used

in Figure III.2 (top) in that the grooves are located next to the contact opening of the mask, as in Figure III.11.

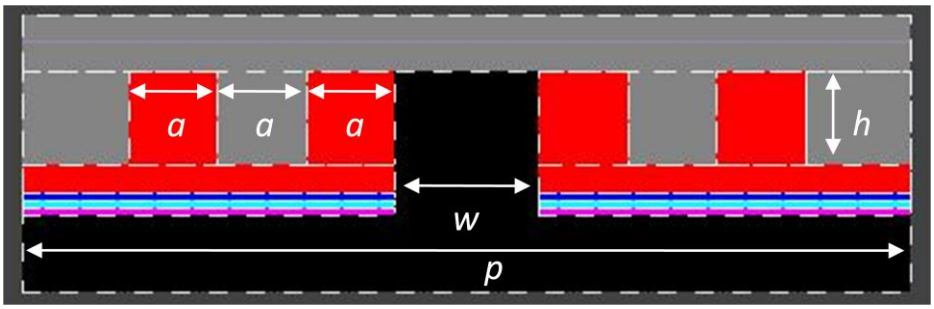


**Figure III.11: Mask layout showing location of EWAF features and proximity to slot. *p*=1600 nm and *w*=260 nm.**

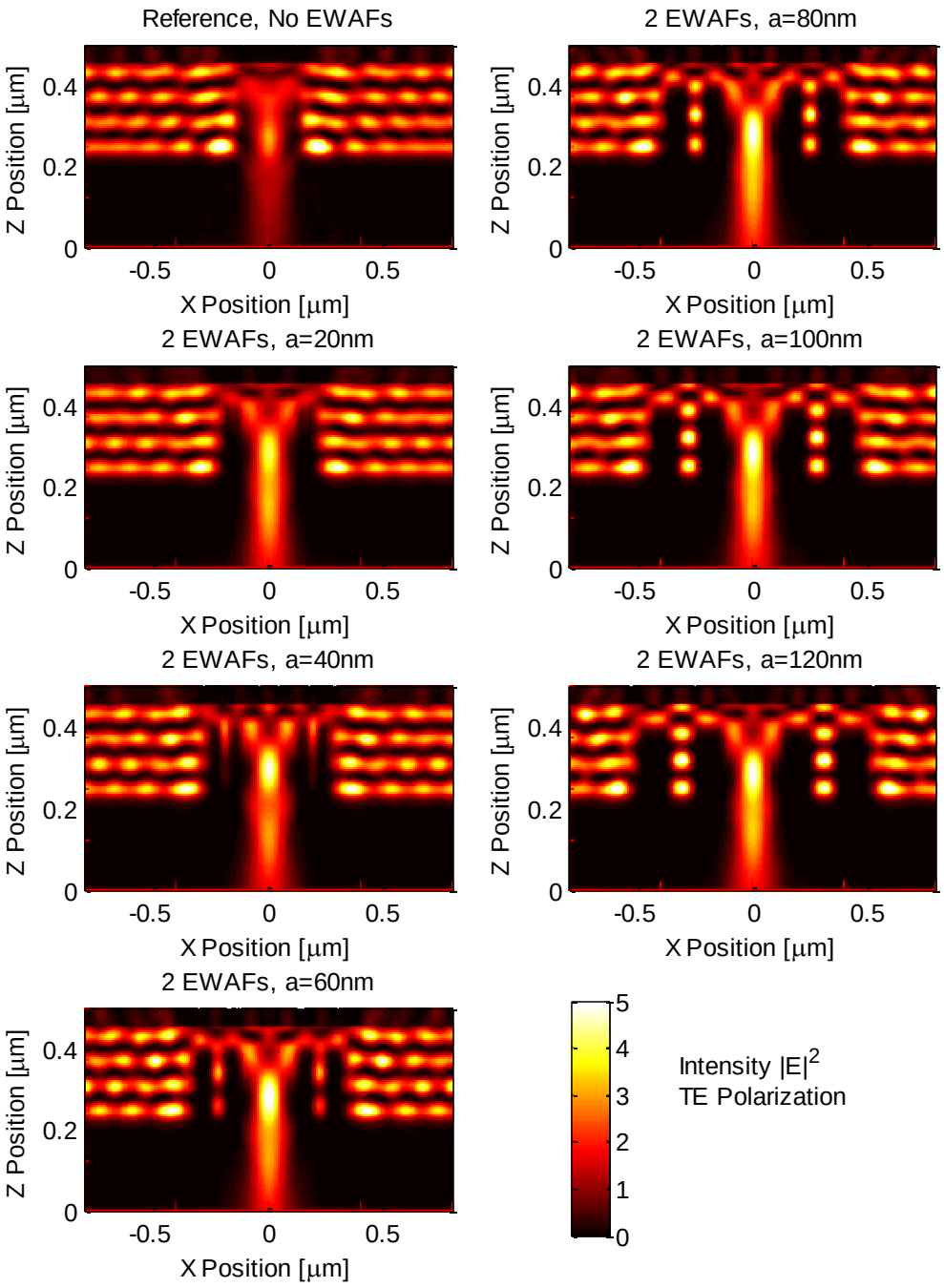


**Figure III.12: FDTD simulation of mask layouts described in Figure III.11.**

The FDTD-based Maxwell's equations solver TEMPEST pr2 [61] was used to simulate the differently sized raised groove structures under TE illumination. The results are displayed according to groove width *a* in Figure III.12. As groove width changes, the field profile in the glass is changed, however more important is the effect caused on the radiation transmitted through the contact. The bright central spot reaches a maximum when $a$=60 nm, or approximately $\lambda/2n_{glass}$. Also important is that TE illumination was used, suggesting that the scattered near fields from the grooves may be responsible for this change in intensity distribution at the contact center.

Another characterization of the near-field effects arising from inclusion of EWAFs was done using features evenly spaced above a solid Cr absorber [73]. In this experiment, FDTD simulation was performed using 193 nm TE illumination for an 862 nm pitch feature ($p$) with 180 nm contact ($w$) and using 62 nm x 62 nm square EWAFs ($a$ and $h$, respectively). These constrained features were placed evenly across the absorber as the number of assist features was varied, represented by N. As Figure III.13 shows, as the number of features is increased, the intensity distribution changes shape and size. A constant intensity contour is included throughout the figure to objectively show the effect.

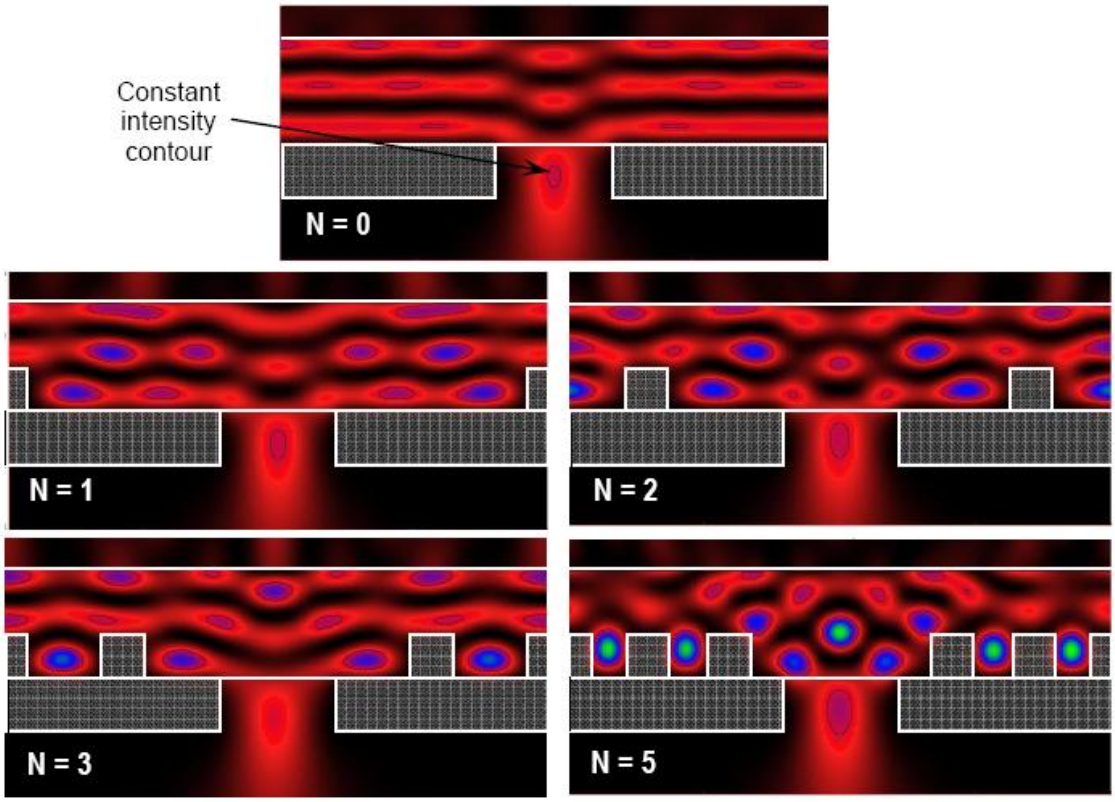


**Figure III.13: Near-field intensity maps of 180 nm slots at 862 nm pitch, with the number of assiste features, N, changing from 0 to 5 [73].**

The intensity in the slot changes with the pitch of the features. At pitches where the features correspond to approximate multiples of $\lambda/n_{glass}$, the constant intensity region grows in size. This is the case for the N=2, and N=5 plots. The N=3 plot is approximately at a $\lambda/2$ pitch and corresponds to destructive interference where the central spot is less intense. The N=1 case's features are too far away from the slot and any evanescent waves diffracted from the grooves attenuate before an obvious change happens. Looking at the N=2 spot in more detail in Figure III.14 shows that at the central cut-line, the intensity compared to N=0 has a 20% size decrease and a 17% intensity increase caused by the added EWAF grooves.

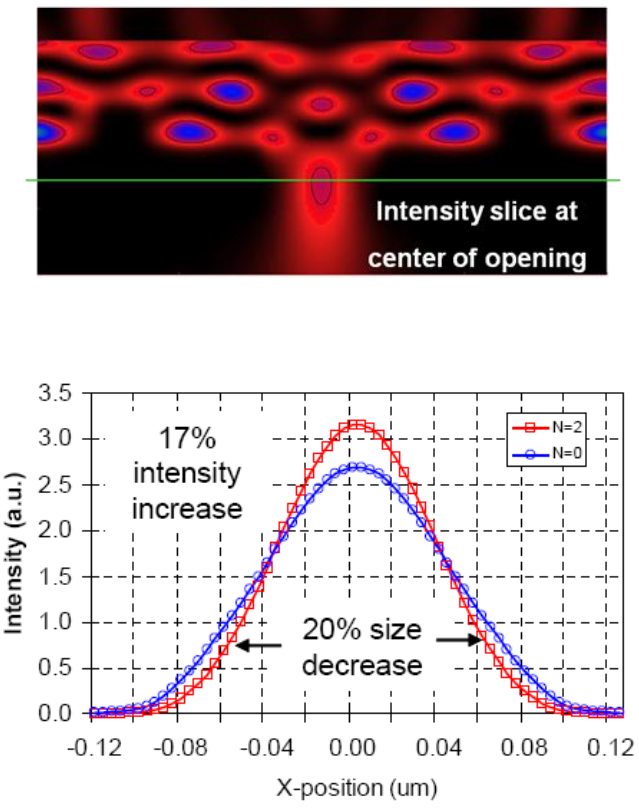


**Figure III.14: Intensity distribution at the center of the N=2 slot, pictured in the top intensity map [73]. the 20% size decrease is taken at a 0.75 level.**

Extending this concept further to a 2-D feature, contact holes were simulated. Although the ideal geometry for isolated holes is known as a ring-shaped groove, in this case a Manhattan layout was preferred because of its compatibility with traditional mask-making processes [30]. Mask feature parameters were adjusted only slightly from those above, with the contact CD=180 nm and the contact pitch equal in *x* and *y*. The top-down view (looking through the glass) for the case of N=4 assist features is shown below. The dashed region in the upper right corner is a single domain that was simulated at periodic boundary conditions.

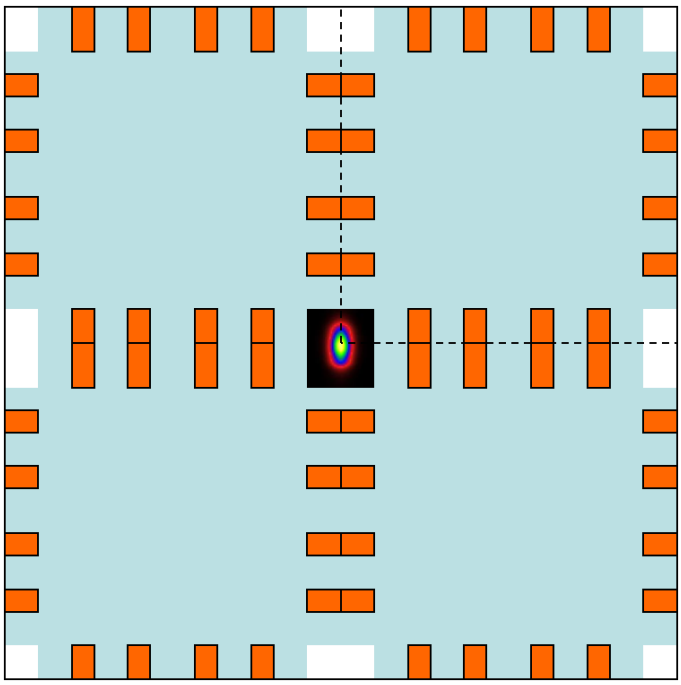

**Figure III.15: Top-down view of layout with contacts in two dimensions and Manhattan style EWAFs. The assist features are located at the absorber/glass interface and are in dark-field portions of the mask [15].**

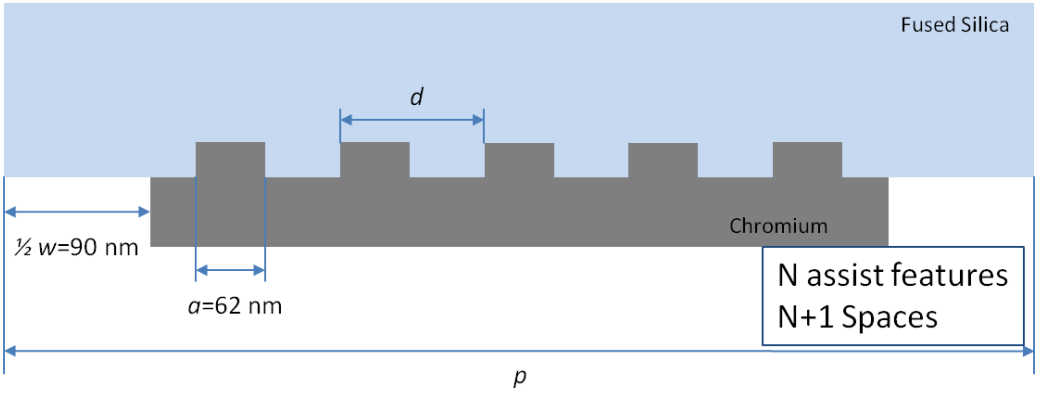


**Figure III.16: Side view of Figure III.15 showing detail on EWAF layout and spacing. The EWAFs have equal spacing across the mask absorber.**

The single domain is then arrayed infinitely in software so the simulated conditions resemble those in Figure III.15. The contact pitch of the design above was varied from 400 nm pitch to 1500 nm, and the number of assist features was varied from 0 to 5, all spaced equally on the dark-field absorber island in between contacts. Figure III.16 shows

the side view of the EWAF spacing scheme employed. EWAFs are placed such that there is an equal space between each assist feature as well as between the end EWAFs and the edge of the contact. In preparation for far-field results, the output plane was moved to a *z*-location $\lambda/4$ below the lowest absorber surface and $\lambda/4$ above the bottom of the simulation domain. Results in the near-field are presented below in Figure III.17 and Figure III.18. For these simulations, the highest intensity occurred when the main feature pitch allowed assist features to be inserted at pitches near $\lambda/n_{glass}$.

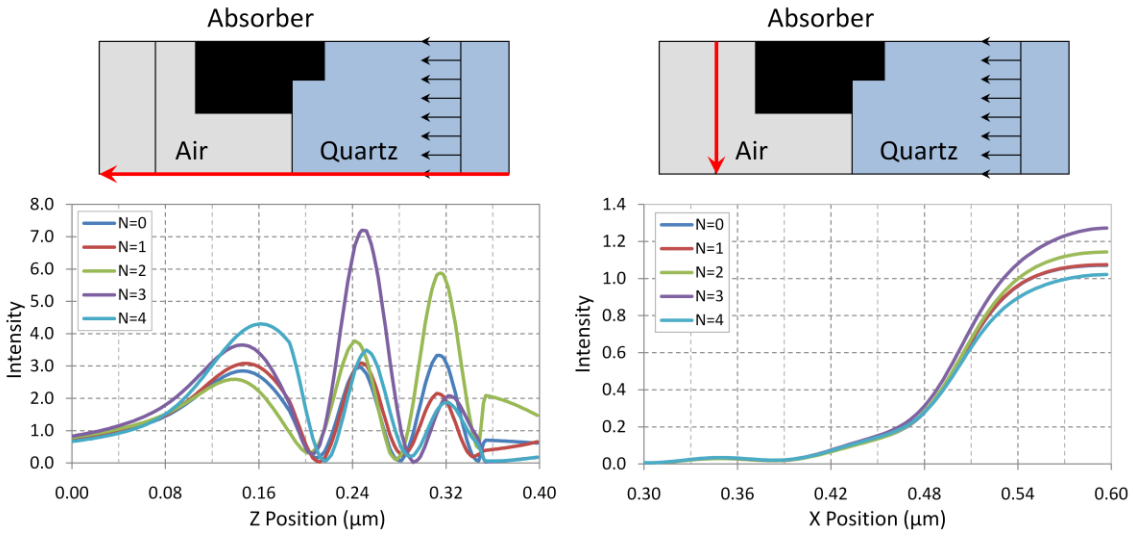


**Figure III.17: Intensity cutlines taken straight through the center of the contact, and $\lambda/4$ below the absorber. These plots are from a 90 nm Cr absorber with 600 nm pitch. Max intensity is at N=3, a gain of 18.8%.**

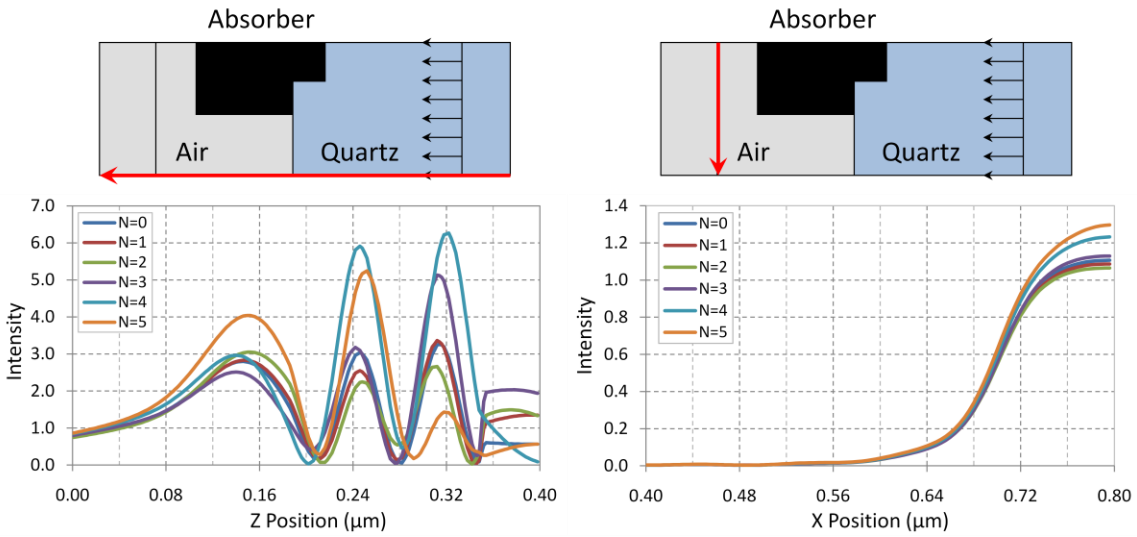


**Figure III.18: Intensity cutlines taken straight through the center of the contact, and $\lambda/4$ below the absorber. These plots are from a 90 nm Cr absorber with 800 nm pitch. Max intensity is at N=5, a gain of 17.2%.**

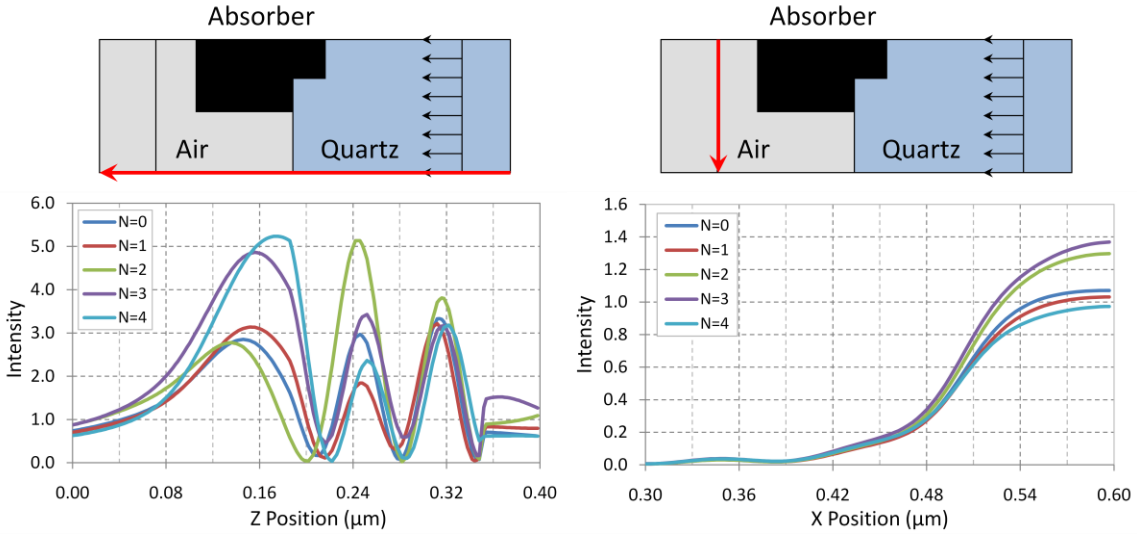


**Figure III.19: Intensity cutlines taken straight through the center of the contact, and $\lambda/4$ below the absorber. These plots are from a 90 nm Cr absorber with 600 nm pitch and a $3\lambda/4$ EWAF etch height *h*. Max intensity is at N=3, a gain of 28%.**

The left-hand side plots above show the intensity variation as the cutline is taken vertically down the center of the contact. This gives a snapshot of the intensity

distribution with $z$ distance. The right-hand side plots are from a horizontal cutline $\lambda/4$ below the absorber, as described above. Analyzing the cases in Figure III.17 and Figure III.18, the largest near-field intensity gain occurs when contact pitch and the number of assist features allows for the EWAF pitch, $d$, to be approximately $\lambda/n_{glass}$. Taking the results of varying the number of assist features and contact pitches, an ideal case of identical EWAF pitches is simulated in Figure III.19. Here a Cr absorber is used and the contacts are simulated at $w$=180 nm, $p$=600 nm as in Figure III.17. These conditions correspond to the highest intensity increase in the center of the contact for chromium absorber material studied so far. In the case of Figure III.19 however, the EWAF depth is changed to $3\lambda/4n_{glass}$ and the result is further improvement in the intensity value taken along the horizontal cutline at the center of the contact. The intensity improvement over an N=0 mask is 28%.

These experiments were extended further and Cr, $Cr_2O_3$, and CrN as mask absorbers in conjunction with the EWAF depth, $h$, were analyzed. The materials were selected due to their relevance to mask making and compatibility with current mask processes.

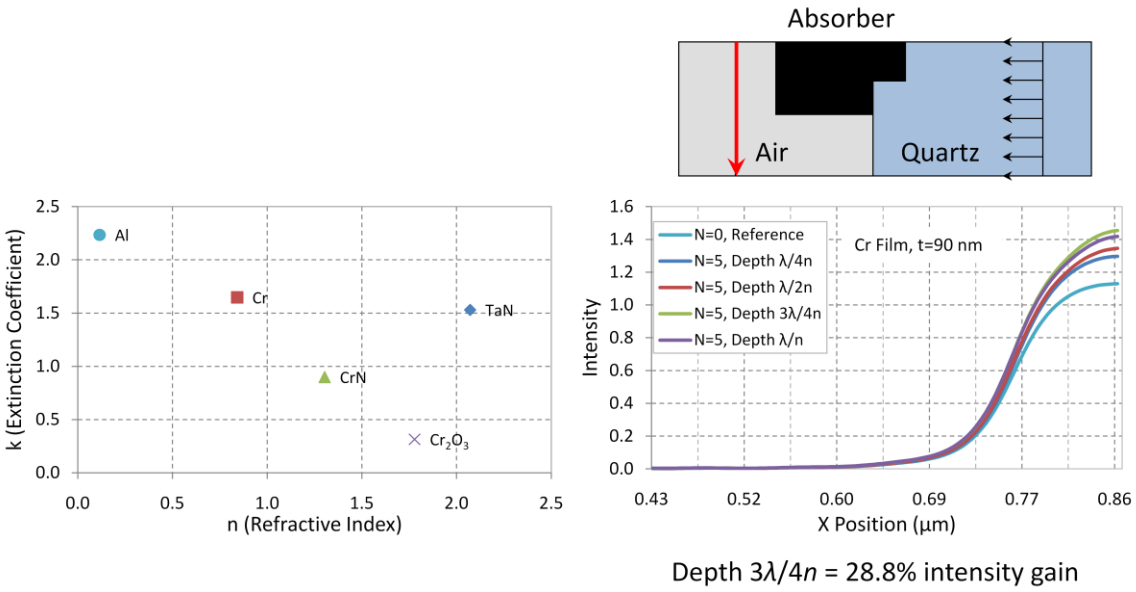


**Figure III.20: Refractive index scatter plot, along with horizontal cutline information for a Cr absorber photomask at 862 nm pitch with varying EWAF etch depths, *h*. N=5.**

For the etch depth and materials study, contact size was kept at 180 nm while contact pitch was adjusted to 862 nm. This pitch allows for insertion of N=5 EWAFs at an optimal pitch of $\lambda/n_{glass}$. The etch depth was also varied at multiples of wavelength to determine if the intensity signatures of the contacts were affected. Results from this experiment are shown in Figure III.20 and Figure III.21. In general, by adjusting the EWAF etch depth of every material studied, a higher central intensity was seen. In the case of Cr, the best case at $h=3\lambda/4n_{glass}$ resulted in an intensity increase of 28.8% over nominal. Both CrN and $Cr_2O_3$ had larger intensity improvements of 42.0% and 42.6% respectively, compared to their N=0 cases.

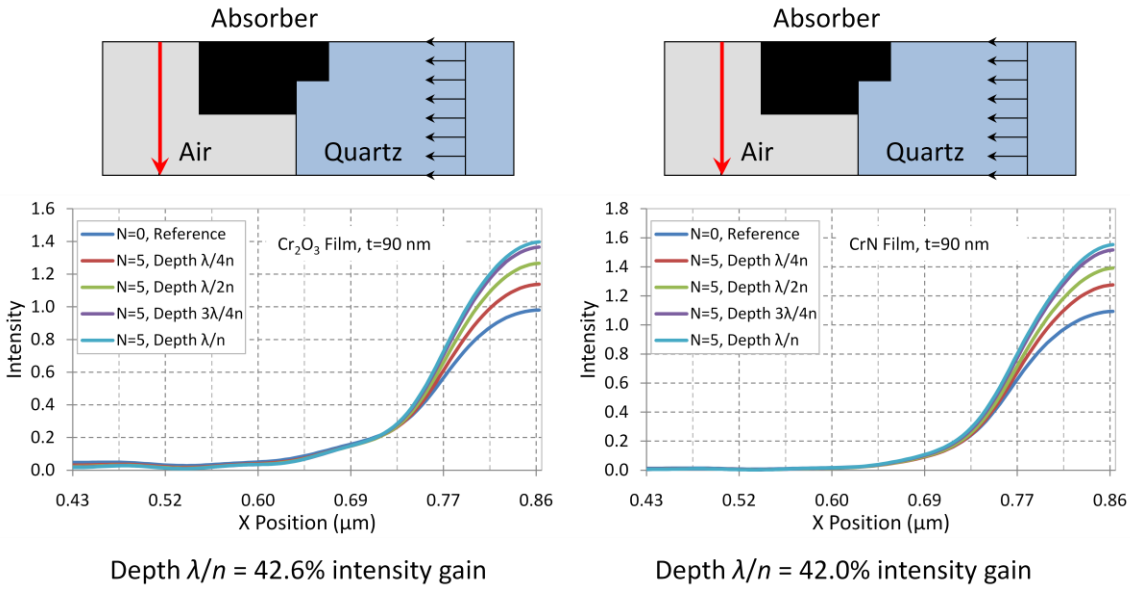


**Figure III.21: Horizontal cutline information for $Cr_2O_3$ and CrN absorber photomasks at 862 nm pitch with varying EWAF etch depths, *h*. N=5.**

These best-case near-field results were then used as inputs for lithography simulation to determine the EWAF's effect on the aerial image through the projection system. $Cr_2O_3$ was used as the mask absorber since in most cases it is a component of binary mask composite absorber films and it provided the best near-field performance. Figure III.22 shows the $0^{th}$, $1^{st}$, and $2^{nd}$ diffracted orders projected for both TE and TM illumination. As the etch depth is increased, the $0^{th}$ order is decreased, while the $\pm1^{st}$ and $\pm2^{nd}$ order magnitudes are simultaneously increased for both illuminations. The $0^{th}$ order magnitude is decreased by 30%, while the $1^{st}$ and $2^{nd}$ order magnitudes are increased by approximately 19%. The diffraction orders from the mask were used in a high-NA vector lithography simulation at NA=0.93 and σ=0.3 [61]. These exposure tool values were selected based on the wafer-level contact pitch of 215 nm. Recasting the Rayleigh Criterion, Equation (1.2), the effective NA, $NA_{eff}$ needed to print this feature pitch can be calculated as [7]:

$$\mathrm{NA}_{\mathrm{eff}} = \frac{\lambda}{p} \tag{3.28}$$

For this main feature pitch, *p*, the coherent effective NA was approximately 0.90. Lithographic objective lenses have maximum NA values that jump in incremental improvements from previous generations. In this case a 0.93 NA lens is the incremental jump from 0.85 NA exposure systems and is able to print these *p*=215 nm features throughout the full range of illumination angles. The partial coherence of 0.3 was chosen because it is the minimum possible $\sigma$ setting on most systems of this vintage.

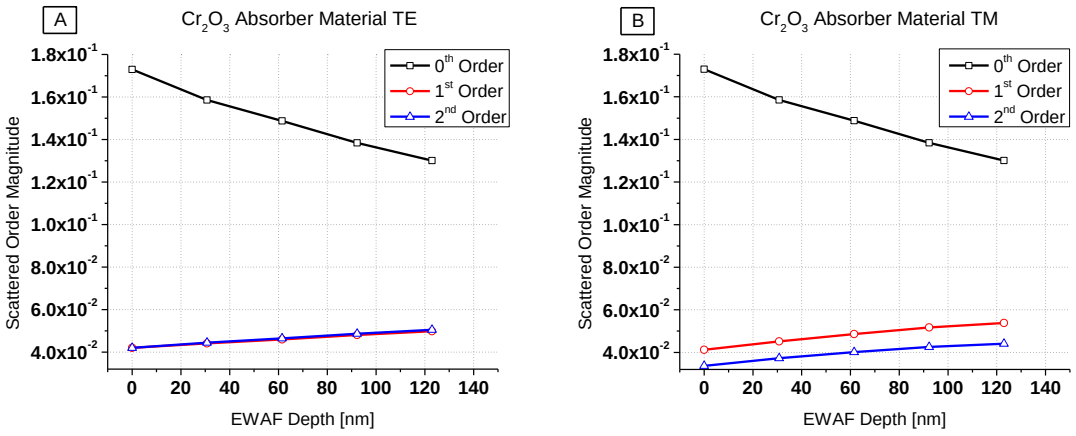


**Figure III.22: Primary diffraction order magnitudes for TE (A) and TM (B) illumination of $Cr_2O_3$ mask in Figure III.21 [15].**

The aerial images at best focus are shown below in Figure III.23 as the etch depth, *h*, of the N=5 EWAFs is adjusted. For comparison, the aerial images have been normalized. It is evident that as the EWAF etch depth is increased, the areas between contacts become darker.

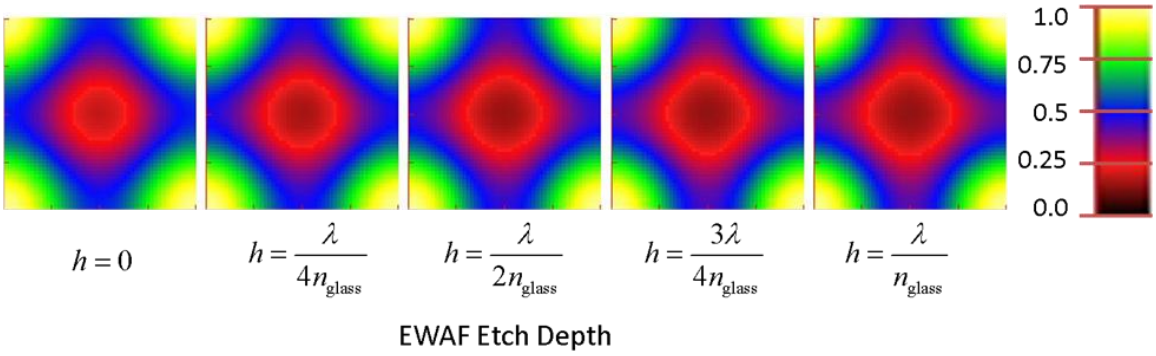


**Figure III.23: Normalized top-down aerial images at best focus of contacts investigated in Figure III.21. Contact CD=45 nm and pitch is 215 nm. Unpolarized illumination, NA=0.93, and σ=0.3 [15].**

This is more easily viewed in Figure III.24, where the intensities across the cutline are taken and compared. The simulated domain has its dark-field areas darkened in horizontal and vertical, as well as diagonal directions. Figure III.23 and Figure III.24 are from unpolarized illumination, and the contrast gain is approximately 27% when the full-wavelength deep EWAFs are used. There is also an increase in ILS, from 2.06 to 2.65.

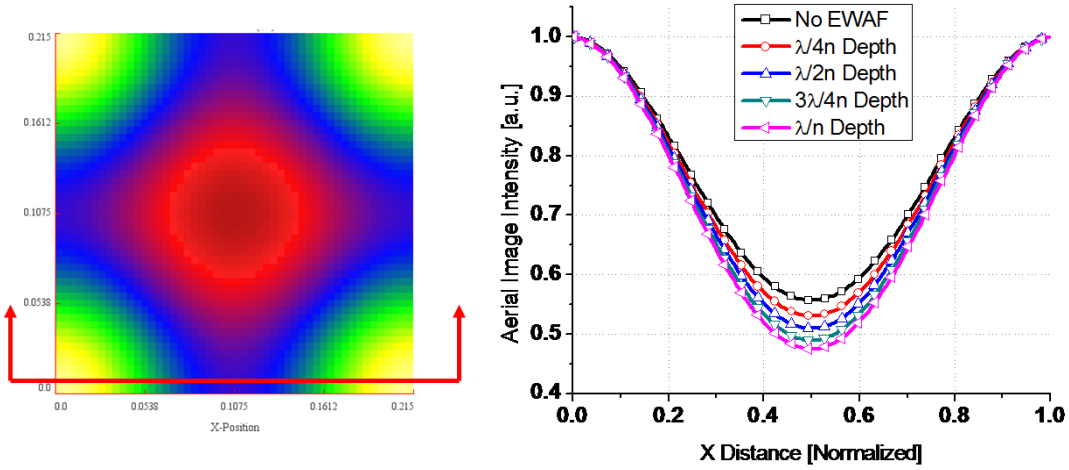


**Figure III.24: *X*-axis cutline through center of contacts, unpolarized illumination at NA=0.93 and σ=0.3. Left diagram shows cutline position. Intensity profiles for the normalized aerial images are shown on the right. ILS from 2.06 to 2.65 and 27% contrast improvement over the unassisted case [15].**

Adjusting the simulation slightly to use azimuthally polarized (TE) illumination with NA=0.93 and σ=0.3 shows that the EWAFs respond in a similar way, but are less sensitive to azimuthal polarization than they are to unpolarized conditions. The azimuthal, or tangentially polarized light shown in the inset of Figure III.25 assures that for each direction of diffracted order the electric field is TE polarized in its Plane of Incidence (POI). In this case, the contrast improvement was only 8% and ILS improved from 1.1 to 1.3 over unassisted contact patterns.

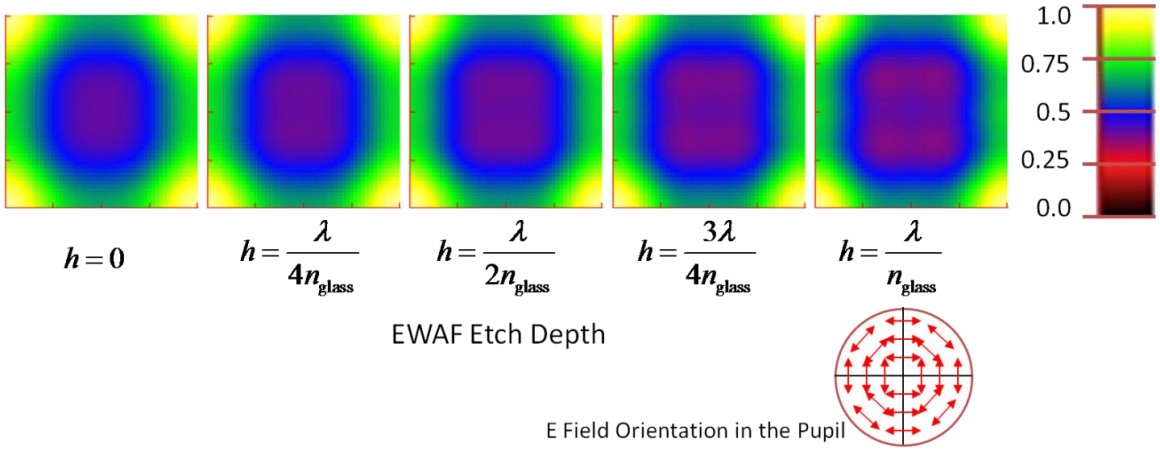


**Figure III.25: Normalized top-down aerial images at best focus of contacts investigated in Figure III.21. Contact CD=45 nm and pitch is 215 nm. TE polarized illumination, NA=0.93, and σ=0.3. The inset describes the electric field orientation in the pupil plane.**

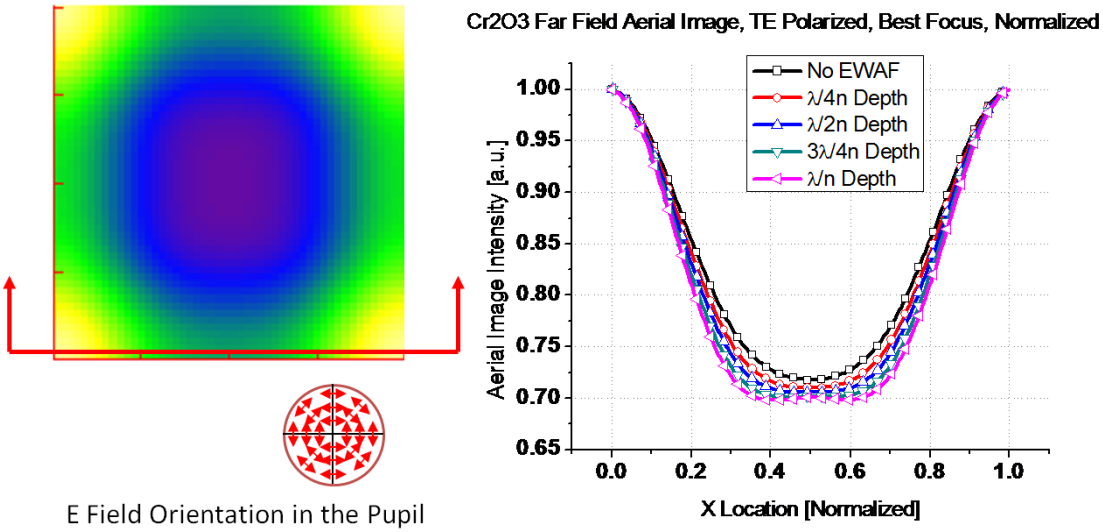


**Figure III.26: *X*-axis cutline through center of contacts, TE polarized illumination at NA=0.93 and σ=0.3. Left diagram shows cutline position. Intensity profiles for the normalized aerial images are shown on the right. ILS from 1.1 to 1.3 and 8% contrast improvement over the unassisted case.**

Finally, Figure III.27 and Figure III.28 are the same simulation performed with radially polarized (TM) illumination with NA=0.93 and σ=0.3. The radially polarized light shown in the inset of Figure III.27 assures that for each direction of diffracted order the electric field is TM polarized in its Plane of Incidence (POI). Figure III.28 shows the negative effects of the TM polarization are also increased as the EWAF etch depth is increased. In this particular pattern, the consequences of TM illumination are the central lobes or dark spots in the center of each contact hole. This is most visible in the $h=\lambda/n_{glass}$ case in the corners of the simulation domain. The unusual intensity profiles are also apparent in Figure III.28. The dark contact spot is due to the polarization of the light used since two electric field components contribute to intensity.

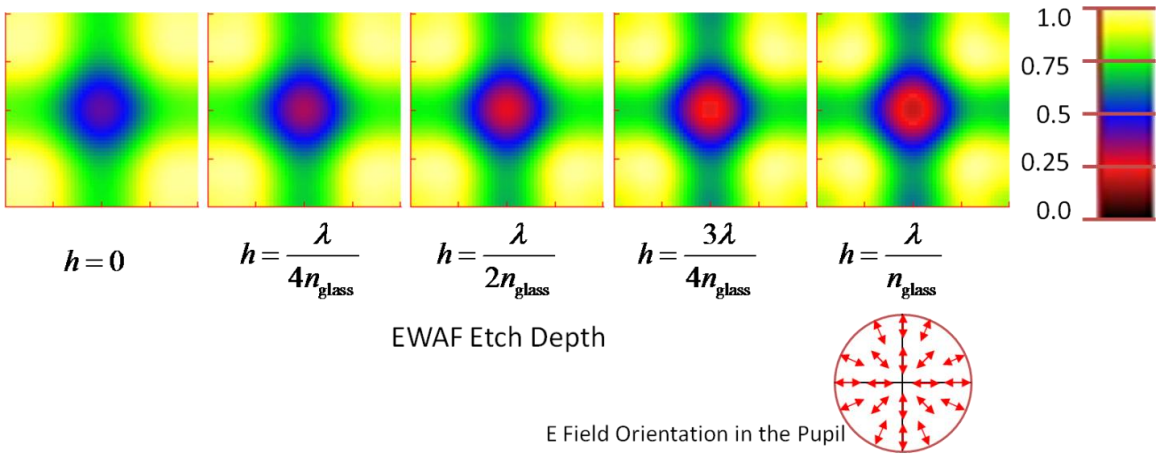


**Figure III.27: Normalized top-down aerial images at best focus of contacts investigated in Figure III.21. Contact CD=45 nm and pitch is 215 nm. TM polarized illumination, NA=0.93, and σ=0.3. The inset describes the electric field orientation in the pupil plane.**

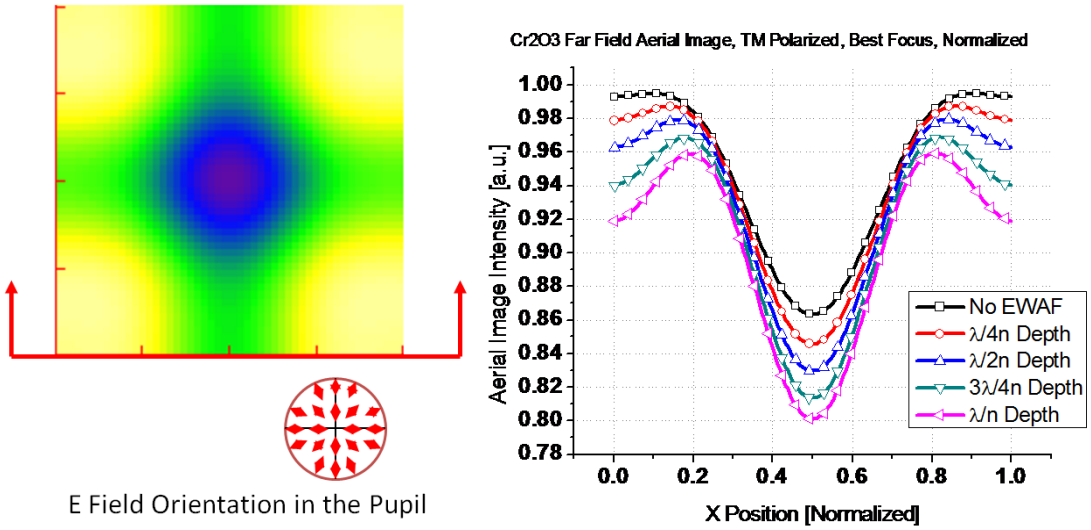


**Figure III.28: *X*-axis cutline through center of contacts, TM polarized illumination at NA=0.93 and σ=0.3. Left diagram shows cutline position. Intensity profiles for the normalized aerial images are shown on the right. Undesired center lobes (recurve) give undesired worsening contrast and are more severe as *h* increases.**

This polarization effect is well known and has been studied extensively [69], [74]. The low intensity areas at the center of each contact occur because at the image plane, the electric field components of the diffraction orders in the *x* direction are pointed in the

same direction, while the *z* components have opposite sign. The Fourier transforms of these plane wave components gives a cosinusoidal term associated with the *x* component electric field and a sinusoidal term associated with the *y* component electric field. Since the states are summed incoherently (in intensity), when the components are equal, the two terms yield no modulation. These components are determined based on the angle of the diffraction order, and depending on the spatial frequencies. For imaging angles approaching 45°, the image will be increasingly demodulated. At a 45° angle, image contrast will be zero. Increasing imaging angles beyond 45°, image contrast will improve but image tone will be reversed. In the aerial image in photoresist above, the imaging orders in photoresist are 32°. The addition of the EWAFs further amplifies this intrinsic demodulating effect from the radially polarized source.

Although this contact study was promising, there were also confounding effects that warranted further study. The layout of Figure III.11 indicates that when EWAF features are simulated with large *h,* it is possible for the features to be thicker than the nominal absorber region. At the maximum etch depth used above, this corresponds to an EWAF depth of ≈125 nm where the absorber is only 90 nm thick. The opacity of the absorber can be calculated by:

$$\frac{I_t}{I_0} = \exp\left[-4\frac{\pi k}{\lambda_0}t\right] \tag{3.29}$$

In Equation (3.29), $I_t$ is the transmitted intensity through the planar absorber, $I_0$ is the intensity incident on the mask absorber, $t$ is the absorber thickness, $\lambda_0$ is the vacuum wavelength of radiation, and $k$ is the extinction coefficient of the absorber. Optical constants of the mask materials used in the study above were obtained from [75], and are

shown in Table III.2. With CrN and $Cr_2O_3$, large enhancements to the image intensity, especially in the near-field were seen, since the nominal case has a high transmission through the mask absorber.

| **Material** | **n** | **k** | ***T* through 90 nm absorber ($I_t/I_0$)** |
|---|---|---|---|
| **Cr** | 0.84 | 1.65 | 6e-3% |
| **$Cr_2O_3$** | 1.75 | 0.31 | 16.3% |
| **CrN** | 1.29 | 0.90 | 0.5% |

**Table III.2: Refractive indices and *T* for selected mask absorber materials [75].**

As the EWAF depth was increased and the duty ratio of the assists kept at 1:1, the large features contribute to a half-toned increase in absorber thickness. The effective thickness the EWAFs contribute is:

$$t_{\text{eff}} = \frac{h}{2} \tag{3.30}$$

In the cases of $Cr_2O_3$ and CrN, the transmission through the absorber at $h=\lambda/n_{\text{glass}}$ was then 4.6% and 0.01%, respectively. This large effect is seen directly in the $0^{\text{th}}$ order of Figure III.22. As $h$ is increased, the $0^{\text{th}}$ order decreases in part due to the significant reduction in light leakage through the absorber. In contrast, as EWAFs are added with the Cr absorber and thickness increased, the contribution to overall absorber thickness has an insignificant impact on an already low *T*. Diffraction orders from a Cr absorber mask with EWAFs were analyzed as EWAF thickness $h$ was increased, and are shown in Figure III.29. The general trend is the same for this mask as the CrN and $Cr_2O_3$: as EWAFs are added the $\pm1^{\text{st}}$ and $\pm2^{\text{nd}}$ orders are amplified, but only 6%. Also, the $0^{\text{th}}$ order experiences no significant change. When the mask is used in lithography simulation to

quantify the Cr EWAF effects, aerial image quality is not changed as significantly as cases with CrN and $Cr_2O_3$ absorbers. The aerial image from an NA=0.93 and σ=0.3 projection system compared between N=0 and N=5 EWAFs at $h=3\lambda/4n_{glass}$ depths has no significant gain in contrast or NILS.

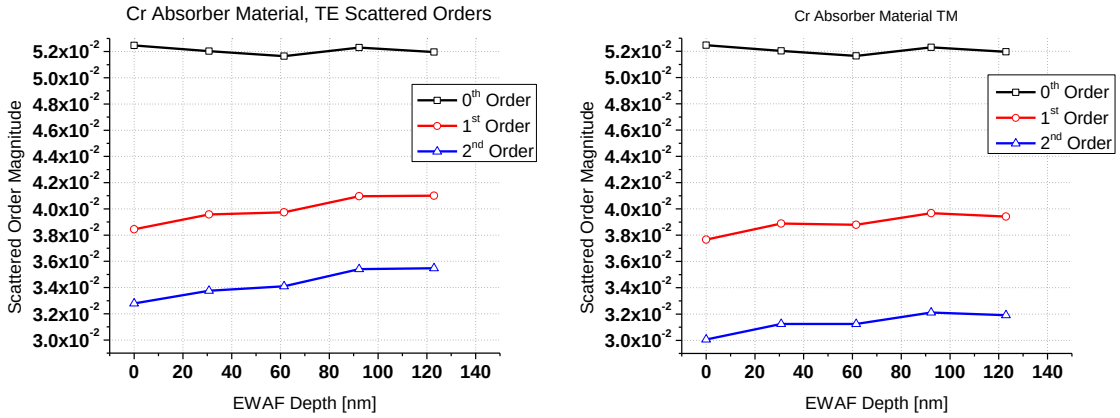


**Figure III.29: Primary diffraction order magnitudes for TE and TM illumination of Cr mask in Figure III.21. Mask *p*=860 nm and *w*=180 nm.**

Intensity values in the near-field below the photomask show excellent response to the addition of EWAFs. Also, Figure III.22 and Figure III.29 both show changes in the diffraction order magnitudes as EWAFs are added, although their relative changes vary with absorber material. In the Cr case, the $0^{th}$ has no significant change as assist thickness is increased, since the transmission through Cr is close to zero even at the starting case. A problem with the assist feature design considered is that as the grooves are added, effective absorber thickness is increased. Several studies have shown that masks with thicker absorber layers have higher contrast aerial images, such as [76]. These other mask effects are confounded with intended EWAF effects. The assist design was carefully adjusted so that the absorber thickness was not increased as the grooves were added.

### G. EWAFs on 1-Dimensional Layouts

In this section, the effects of EWAFs on image quality are investigated. The 1-D layout presented here provides an in-depth study to complement that of Section F. The section is split into several sub-sections that individually study key parts of the lithography process pertaining to EWAFs. Sections G.(i) and (ii) investigate the diffracted orders propagating from photomasks with and without assist features. Section G.(iii) takes the diffracted orders output from the masks with and without EWAFs and uses them as an input to a high NA vector lithography simulator. This allows the influence of exposure tool and diffracted order capture to be determined. The final aerial image contrast and NILS improvements as a result of EWAF inclusion can then be considered and compared to alternative technologies.

#### (i) Top-Surface EWAF

In order to better understand the role of the near-field effects in the far-field images, the test patterns above were simplified to a single dimension. The groove designs themselves were also changed slightly to avoid the above-mentioned influences of absorber thickness variation. The groove layout was changed such that instead of the groove extending into the substrate, the groove now penetrates into the absorber as in Figure III.30. This reduces the range of possible EWAF depths that can be used, but also forces any positive effect on aerial image to be uniquely assist feature related.

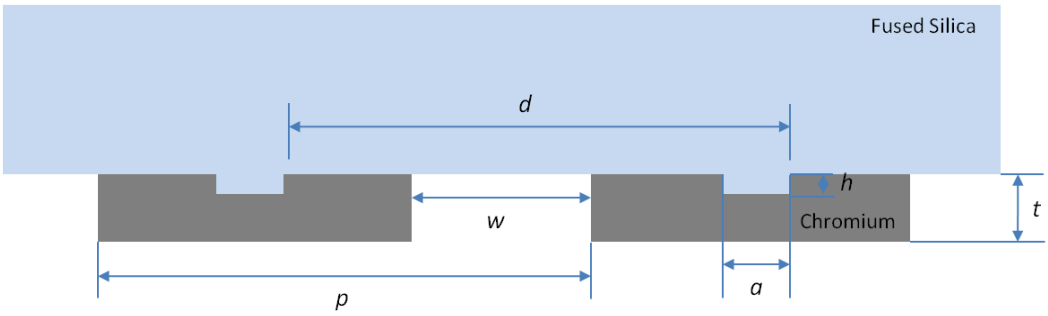


**Figure III.30: Modified EWAF design with grooves extending into the absorber.**

Since all changes in aerial images will relate back to changes in the diffracted orders resulting from inclusion of the grooves, the orders were directly analyzed using the diffracted order enhancement factor described in section E.(i). The arrangement of the EWAFs was also adjusted so that the grooves were equally spaced over the entire domain, not just the absorber. This is illustrated in Figure III.31 with the case of N=2 grooves per period.

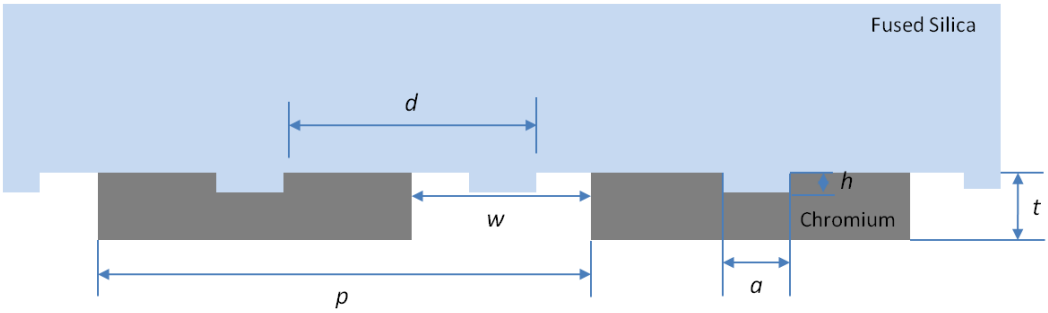


**Figure III.31: Layout with N=2 grooves per period. In this case, the groove pitch *d* is ½ of the main feature pitch *p*.**

The even spacing of EWAFs over the domain was in preparation for fabricating a test case. Simulations were also conducted at $\lambda$=248 nm, since the scaling increases the dimensions that would need to be fabricated and also facilitates easier testing through more robust light sources.

Layouts similar to those in Figure III.31 using a $t$=90 nm absorber, EWAF depth $h$=30 nm, width $a$=82 nm, and N=3 were analyzed under TM polarization while pitch $p$ was swept from 450 nm to 550 nm and the absorber materials were varied. This range of pitches covers the previously simulated sweet spot corresponding to $d \approx \lambda / n_{glass}$. Results are presented in Figure III.32 for the above studied Cr, $Cr_2O_3$, as well as, Al absorbers. There is a large peak at 496 nm that exists across all material choices. This sharp peak is the point where diffraction orders are at grazing incidence for the top-grooves, as well as the transmitting features. It is also known as a Rayleigh wavelength anomaly, as mentioned in chapter II.F. This allows additional energy to couple into the primary diffracted orders. This peak is strong and sharp, therefore not very useful. For Cr and chromium oxide, the assist groove causes additional light to come through the absorber. In the case of Cr and $Cr_2O_3$, the regions with thinned absorber allow significantly more light through, which is apparent with the large constant offsets in the $0^{th}$ and $1^{st}$ enhancement curves. The $0^{th}$ order is always increased in these cases. In the Al absorber case, since the material is more opaque at 248 nm, there is no significant negative impact that the thinned EWAF absorber has throughout this curve. The Al case also has a unique feature just left of this grazing incidence peak, at 490 nm, where the $0^{th}$ and $1^{st}$ order enhancement factors is 0.94 and 1.06, respectively. Although these are interesting effects, their magnitude does not give any significant far-field benefit. Additionally, the range of this desirable shift in diffracted fields occurs over 10 nm in pitch.

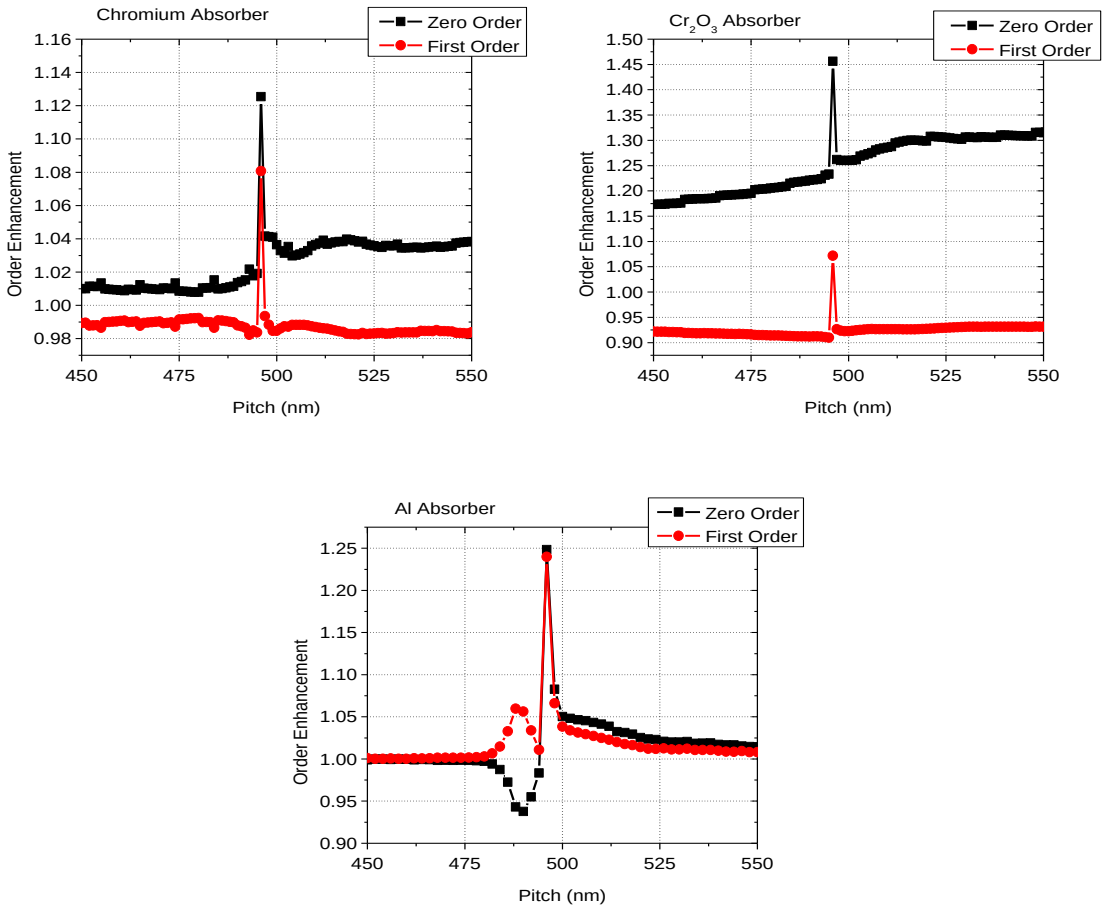


**Figure III.32: Diffraction order enhancement factors from 450 nm-550 nm pitch. N=3, *w*=180 nm, *t*=90 nm, *a*=82 nm, *h*=30 nm. Absorber material is as indicated. TM polarization.**

Under TE illumination, the identical pattern at the same pitches yielded no response, with $0^{th}$ and $1^{st}$ order enhancement ≈1 throughout the range of pitches as in Figure III.33. As the EWAF's tone is reversed, similar to the patterns studied first in Section F, the enhancement factors also change polarity in a similar way as seen in Figure III.34.

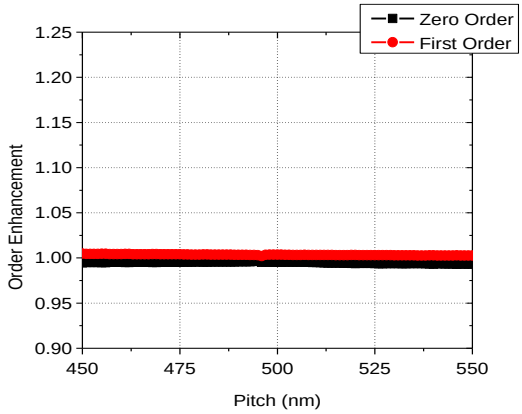


**Figure III.33: Diffraction order enhancement factors from 450 nm-550 nm pitch. N=3, *w*=180 nm, *t*=90 nm, *a*=82 nm, *h*=30 nm. Al absorber, TE polarization.**

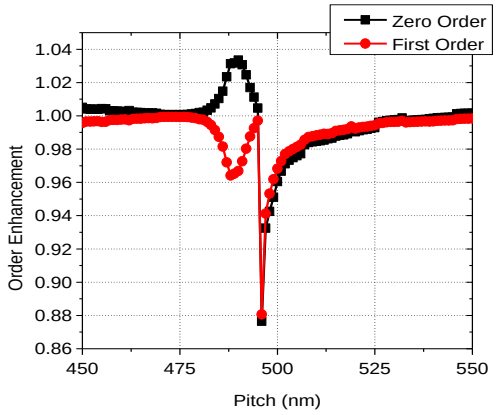


**Figure III.34: Diffraction order enhancement factors from 450 nm-550 nm pitch. N=3, *w*=180 nm, *t*=90 nm, *a*=82 nm, *h*=30 nm. Al absorber, TM polarization. Tone of grooves is reversed, as in Figure III.2 top.**

As the number of grooves per pitch is changed between N=1, 4, 5, and 6 grooves per pitch in Figure III.35, the curves also respond uniquely depending on the assist feature pitch and the main feature pitch. With a single groove per pitch (N=1), the enhancement curve exhibits sharp features corresponding to $p$=248 nm, 496 nm, and 744 nm. This results from strong coupling between the 3$^{rd}$ order of the top-surface EWAF grating and the 2$^{nd}$ order of the transmitting grating features, as well as emerging orders and Wood's

Anomalies. Figure III.36 illustrates this by showing the *x*-component spatial frequency of orders 1 to 4 for both EWAF and transmitting gratings for each layout shown in Figure III.35. The N=1 plot of Figure III.36 indicates that the 3rd order of the EWAF grating and 2nd order of the transmitting grating are closely matched in spatial frequency. At $p$=496 nm, the 3rd order is approximately grazing at the substrate/absorber interface ($\theta \approx 83°$), and the 2nd order is also at grazing incidence of the absorber/air interface. The peak enhancement at $p$=496 nm is not higher because the 3rd order of the EWAF grating has a smaller electric field compared to its 1st order. The smaller field in that particular order limits how much energy can couple to the transmission grating orders. In the case of Figure III.32, the 1st EWAF order is closely matched with and couples to the 2nd transmission grating order. Figure III.36 also illustrates that in the N=3 case, the 2nd EWAF order is matched to the evanescent 4th order of the transmission grating. In the N=1 and N=3 cases, even though reflection and transmission gratings are matched in spatial frequency, the order enhancement occurs at integer multiples of wavelength where diffraction orders emerge from evanescence. The N=4 plot in Figure III.35 is relatively flat because there are no regions where diffraction orders are emergent. By examining the related N=4 plot in Figure III.36, there are also no orders that are as closely matched as in the N=1 or N=3 cases, resulting in very little coupling of energy into transmitted orders. The N=5 case has slightly better coupling between the 1st EWAF order and the 3rd transmitted order, and at $p$=744 nm, the 3rd transmitted order is at grazing incidence, allowing limited energy to couple into propagating diffracted orders. In this case there is also a SPP mode supported by the transmission features which is visible just below the small optical coupling peak at $p$=744 nm.

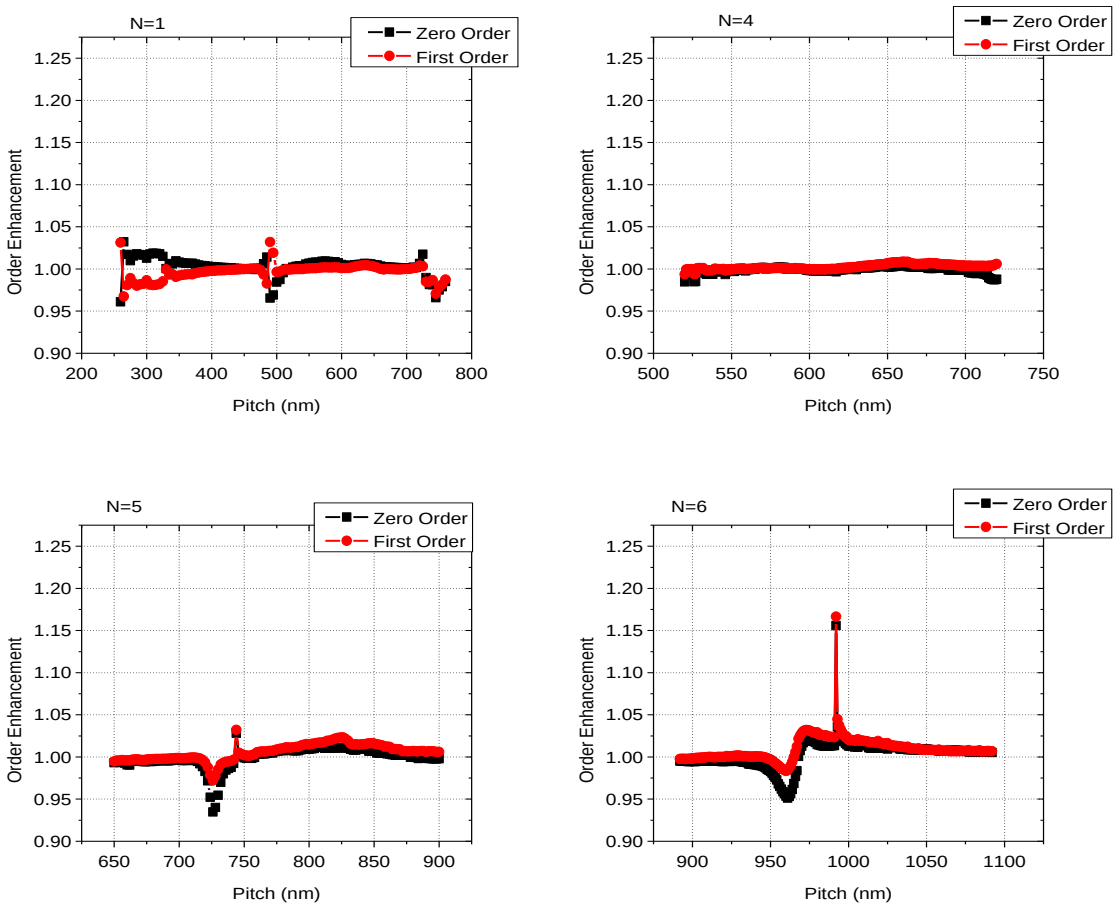


**Figure III.35: Diffraction order enhancement factors through pitch. N varies, *w*=180 nm, *t*=90 nm, *a*=82 nm, *h*=30 nm. Al absorber, TM polarization.**

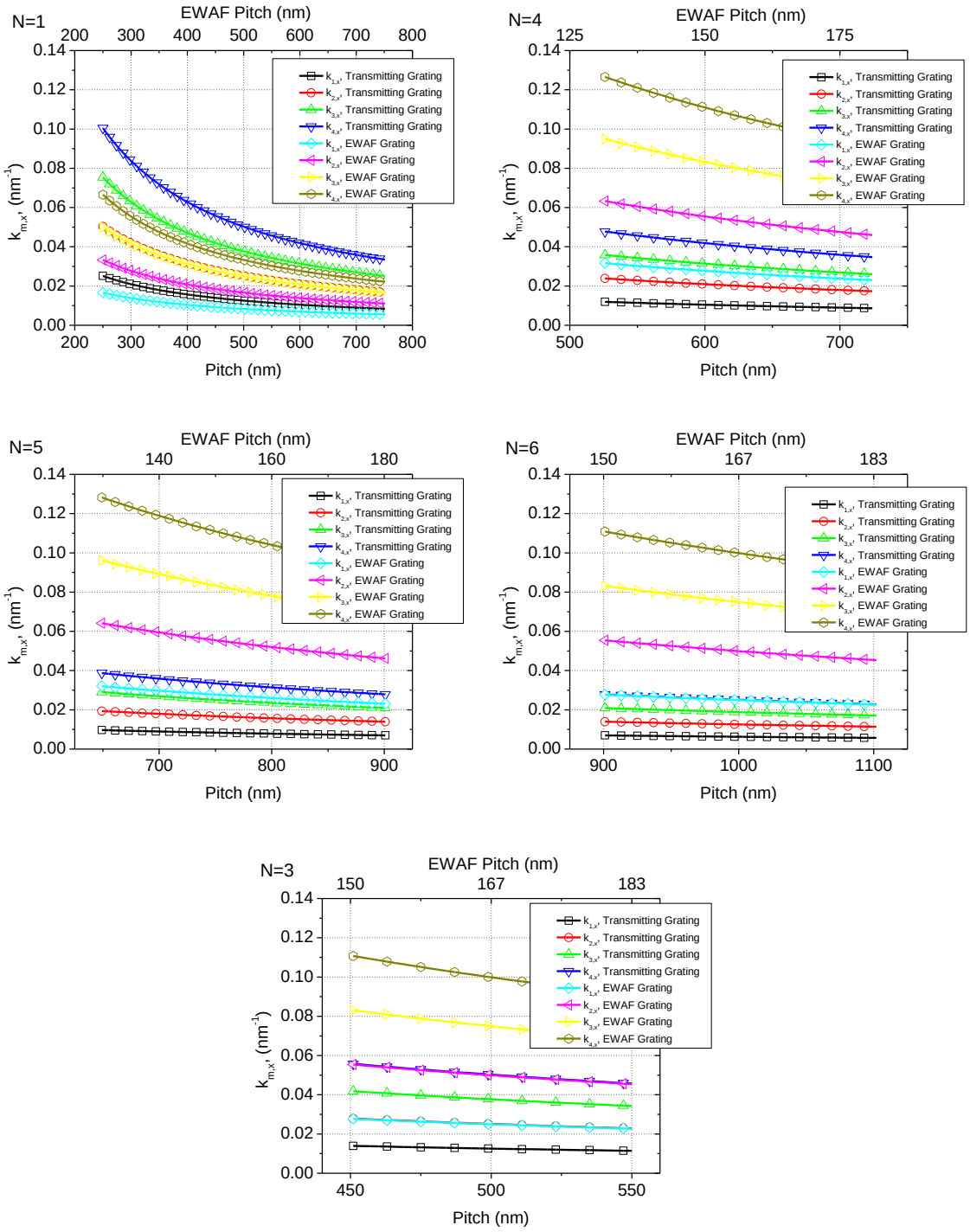


**Figure III.36: *x*-direction spatial frequency, $k_x$, through pitch. Each plot corresponds to the identical conditions in Figure III.35.**

At N=6, the grating pitches are again matched such that the 4$^{th}$ order of the transmission grating is matched with the spatial frequencies of the 1$^{st}$ order EWAF grating. In this

case, a large optical coupling peak is observed at $p$=992 nm, but since the field captured by the emergent 4$^{th}$ order must be distributed over 7 orders instead of the 3 in the N=3 case of Figure III.32, the peak order enhancement is lower. The matching is close, resulting in excellent coupling of additional energy into the transmitting grating at these two pitches. Common to these four plots are small dips just to the left of the optical coupling peaks, which are interpreted as SPP anomalies [25]. These dips in one or both orders represent the reduction in electric field the existing orders of the transmitting grating experiences as the electric field is coupled into an SPP mode supported by the transmission grating. Although several of these designs have interesting effects caused by the EWAF grooves, they occur over a very small pitch range. Even in the case of the most promising top-groove designs, N=3 and 6 with Al absorbers, the optical coupling peak increases 0$^{th}$ and 1$^{st}$ orders uniformly; the aerial image will simply become brighter.

### (ii) Bottom-Surface EWAF

Bottom surface assist features similar to those pictured at the bottom of Figure III.2 were also studied. These were investigated to determine if EWAFs with the same index of refraction as the main feature made any difference to the results. Many similarities of the top EWAF simulations were retained, especially feature width $w$=180 nm, varying pitches, normally incident illumination, EWAF depth $h$=30 nm, and varying numbers of grooves N. Since the Al absorber resulted in the highest order enhancement factors, it was studied extensively. Aluminum is also highly opaque and mitigates the effects of additional light leaking through the absorber areas where grooves are placed. EWAF width $a$ was adjusted to be 124 nm and the absorber thickness $t$ was chosen at 90 nm. The most promising results are for the case where N=1. This also

conveniently allows the EWAFs to be used down to main feature pitches at the resolution limits of projection systems. Figure III.37 shows the diffraction order enhancement factor for these bottom side grooves. The optical coupling peak at $p$=496 is extraordinarily large for $0^{th}$ and $1^{st}$ orders at 1.43 and 2.65, respectively. A second maximum of the $0^{th}$ order is also discernable at $p$=744, where the third orders are at 90°. This effect is not as extreme as the peak at 496 nm since lower energies are carried in the higher orders. The $0^{th}$ order enhancement factor is 1.35 at the peak value at 744 nm pitch.

Another interesting feature of these curves are the changes in layout of the $0^{th}$ and $1^{st}$ order curves which change from enhancement to suppression at pitches which correspond exactly to the surface plasmon resonances. Using the calculated $\beta$ for Al, and Equation (3.31), the pitches for resonance can be determined.

$$\beta = m\frac{2\pi}{p} \tag{3.31}$$

Here $\beta$=2.667e-7 $m^{-1}$ giving the grating pitches to couple into SPPs at $p$=471 nm and 707 nm for m=2 and 3, respectively. These points are exactly where the curves in Figure III.37 intersect.

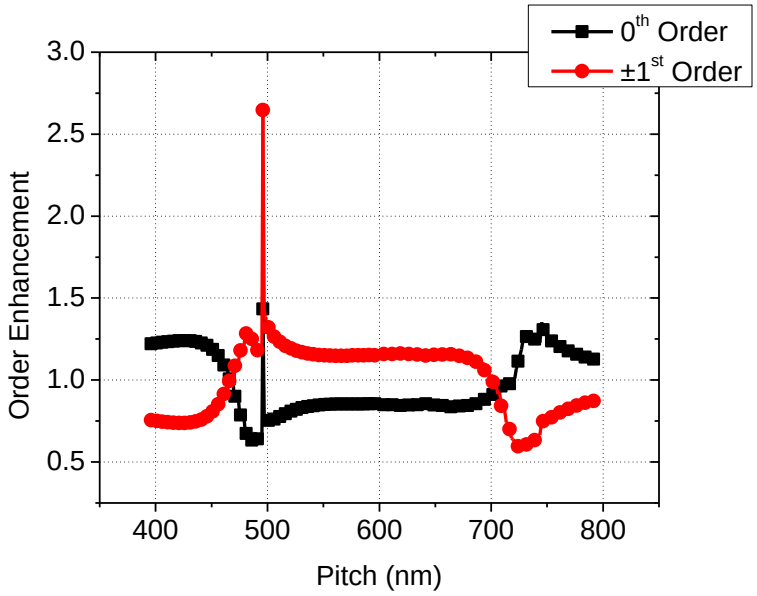


**Figure III.37: Diffraction order enhancement factor for N=1, *a*=124 nm, *h*=30 nm, *w*=180 nm, *t*=90 nm Al absorber. Bottom-side EWAFs through pitch.**

Perhaps the most interesting region in Figure III.37 is in the flat regions between the SPP resonances. Here the curves are nearly flat, with a steady diffraction order enhancement of approximately 1.16 and 0.85 for $1^{st}$ and $0^{th}$ orders, respectively. This is the ideal situation, where the $0^{th}$ order is suppressed and the $1^{st}$ order is made stronger by the grooves. The magnitude of the changes in the primary orders is also significant enough to affect aerial image quality. The analysis at TE polarization was repeated, but only small effects in the enhancement curves were observed. With the crossover points being at SPP resonances and no effects at all being observed under TE illumination, SPPs definitely play a role in the physics of EWAFs. Since Al is a reasonably good conductor at DUV wavelengths, it makes it an ideal absorber to study these phenomena.

The performance of these features was studied across a range of illumination angles to quantify performance in a projection tool. This is important because even at

near-coherent limits, a reticle will always be illuminated by light from a cone of angles. For this task, the central pitch of $p=d$=600 nm was further investigated. Over a range of 12.6°, from -6.3° to 6.3°, the diffraction order enhancements are very predictable and reasonably stable. However, as the plane wave illumination tilts, higher orders will be at grazing incidence with the absorber bottom. This is shown in Figure III.38 near ±9.1°. Approaching this point, the near 90° orders will begin to interact with bottom surface grooves and contribute to an effect similar to the optical coupling peak observed in Figure III.37. In general, the closer the transmitting feature pitch is to having a grazing order, the smaller the stable region of $\pm 1^{st}$ order enhancement is over angle. In the case of $p$=600 nm, the 6.3° edge of the enhancement curve corresponds to a $\sigma$=0.71 for an NA=0.93. Therefore, over the entire cone of illumination, if conventional illumination is used, the $\pm 1^{st}$ orders will be amplified, while the $0^{th}$ order will be suppressed by factors of at least 1.16 and 0.85, respectively.

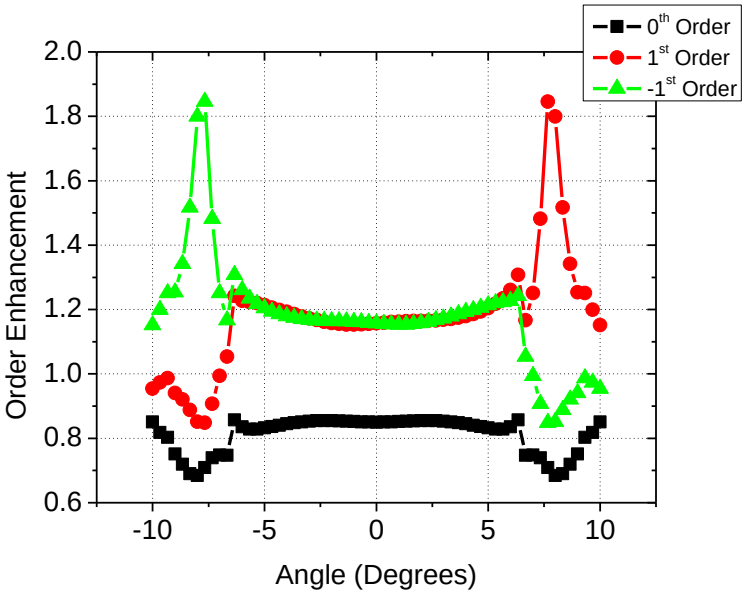


**Figure III.38: *p*=600 nm features from Figure III.37 simulated through incident angle from -10° to 10°. Angles represented are inside the fused silica mask substrate.**

The enhancement factor for such a *p*=600 nm structure can also be visualized via a dispersion relation [14]. Figure III.39 shows two such plots. The plot on the left-hand side illustrates the Degree of Enhancement (DoE) plotted vs. in-plane wave vector for incident light, $k_x$, and photon energy ranging from 4.13 eV to 6.20 eV (300 nm to 200 nm). For reference, $\lambda$=248 nm corresponds to ≈5 eV. DoE is defined as:

$$\text{DoE}=\frac{\left|E_0^{\text{EWAF}}\right|^2-\left|E_0^{\text{ref}}\right|^2}{\left|E_0^{\text{EWAF}}\right|^2+\left|E_0^{\text{ref}}\right|^2} \tag{3.32}$$

In Equation (3.32), the squared magnitudes of the electric fields for 0th order light are compared between designs with and without bottom EWAF grooves. This metric is similar to the enhancement factor used above, but it is centered about zero. In Figure III.39, the conditions where this particular *p*=600 nm layout supports grazing incidence diffracted orders as well as SPP resonance is also shown overlaid on the plots. A black

outline indicates regions where the 0th order goes through a DoE of zero, going from suppression to enhancement.

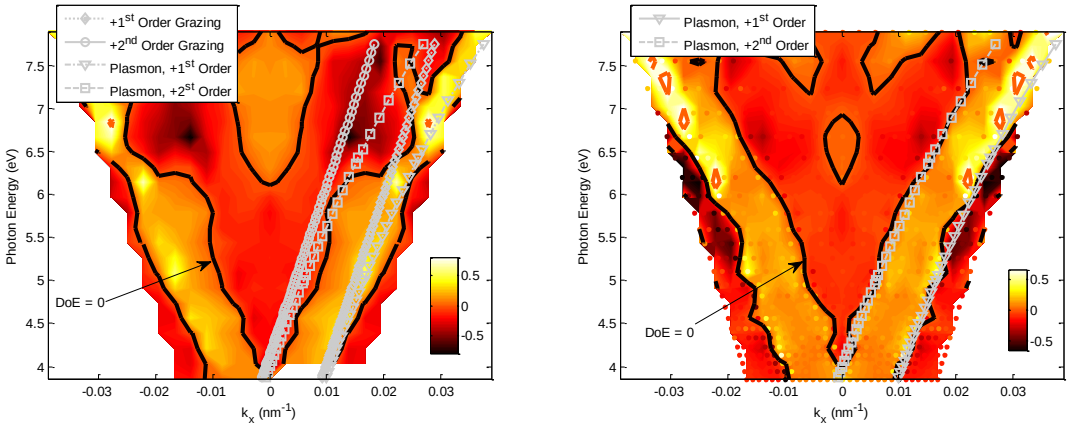


**Figure III.39: Left: Degree of Enhancement (DoE) for *p*=*d*=600 nm grating with square bottom EWAF features. Right: DoE for *p*=*d*=600 nm grating with sinusoidal bottom EWAF features [14].**

The left-hand figure is for the 30 nm depth, square profile bottom surface grating studied so far. In general, the highlighted regions of DoE=0 coincide with the SPP resonances. However, the right-hand side figure illustrates an identical pattern, except the EWAF case uses a sinusoidal bottom surface profile with a period of 300 nm and 15 nm amplitude, such that the total displacement of the bottom surface is similar to the 30 nm square groove. In this case, the sinusoidal profile almost exactly corresponds to the SPP resonance for this grating over a large wavelength range. The similarities in these two plots suggest that for the square groove case at $\lambda$=248 nm, the SPP resonance supported by the gratings is the demarcation point between enhancement and suppression in the 0th and 1st orders. For the square groove case, however, higher harmonics that compose the EWAF profile also contribute effects that cause the curves to deviate slightly from this relationship. The dependence on the bottom surface grating also suggests that the EWAFs

function as a grating, rather than as individual scatterers of the evanescent orders supported by the plane waves.

### (iii) Far-Field Image

Bottom-surface EWAFs can adjust the balance of energy in the diffracted orders, but until this point only the reticle has been considered. The final image of the photomask is formed in the image plane, conjugate to the object plane where the reticle sits. Projection lithographic enhancement techniques must therefore consider the projection tool and its influence on the final intensity profile delivered to the photoresist. In this section, the diffracted orders from the reticle are captured by the objective lens and transferred to the imaging medium where they can be analyzed.

The 600 nm pitch reticle with 180 nm CD and N=1 assist feature/pitch was simulated across several imaging system configurations to test its ability to improve the aerial image. Details of the lithography simulation code are included in Section C above. Three system configurations are explored using $\lambda$=248 nm with TM polarization: NA=0.93, $\sigma$=0.8; NA=0.99, $\sigma$=0.7; and NA=1.2, $\sigma$=0.55. A line source is used for illumination, such that plane waves impinging on the mask will always be TM polarized and reside in the plane of incidence. This source is illustrated in Figure III.40. The imaging stack used for this investigation is presented in Table III.3. The BARC thickness was optimized for each system configuration, and was always ≈62 nm.

| Material | n | k | Thickness (nm) |
|---|---|---|---|
| **$H_2O$** | 1.373 | 0 | -- |
| **Topcoat** | 1.54 | 0 | 30 nm |
| **Resist** | 1.69 | 0.04 | 150 nm |
| **BARC** | 1.48 | 0.43 | 62 nm |
| **Silicon** | 1.57 | 3.57 | -- |

**Table III.3: Film stack used for far-field imaging. Material indices are taken from the $\lambda$=248 nm materials database used in [77].**

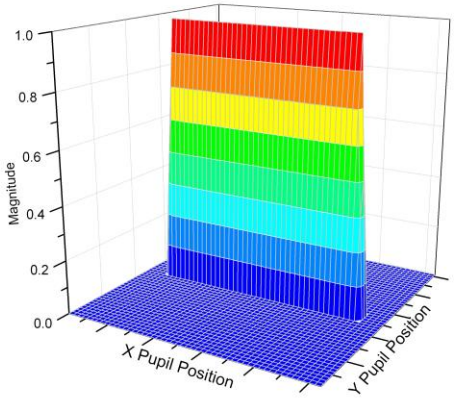


**Figure III.40: Illustration of the line source used for imaging EWAF reticles.**

The first configuration, NA=0.93, $\sigma$=0.8, was chosen to explore the imaging limits for this generation of tool. The source shown in Figure III.40 was divided into 31 discrete plane waves to give dense sampling of the illumination angles involved. In the first configuration, sampling across the pupil is at 0.45° intervals. Figure III.41 shows resist intensity x-sections and best focus cutlines for the 0.93 NA, 0.8 $\sigma$ configuration. At best focus, the reference case (without EWAFs) had a low contrast of 0.089, while the EWAF inclusive case had a slightly higher contrast of 0.091. NILS values were 0.127 and 0.130, respectively. The improvement in both image contrast and NILS as a result of the addition of EWAFs was approximately 2%. These contrast and NILS values are low because diffracted order capture is only happening at the edges of the pupil, at $\sigma$ settings

of 0.78, corresponding to an angle (in glass) of ≈7°. Furthermore, when the EWAFs are added to the mask, at this collection angle the 1st order's enhancement factor is near unity. This manifests itself as a very low change in contrast and NILS. Through a large range of the input plane waves, only the 0th order is being collected by the lens, which serves only to add intensity to the image.

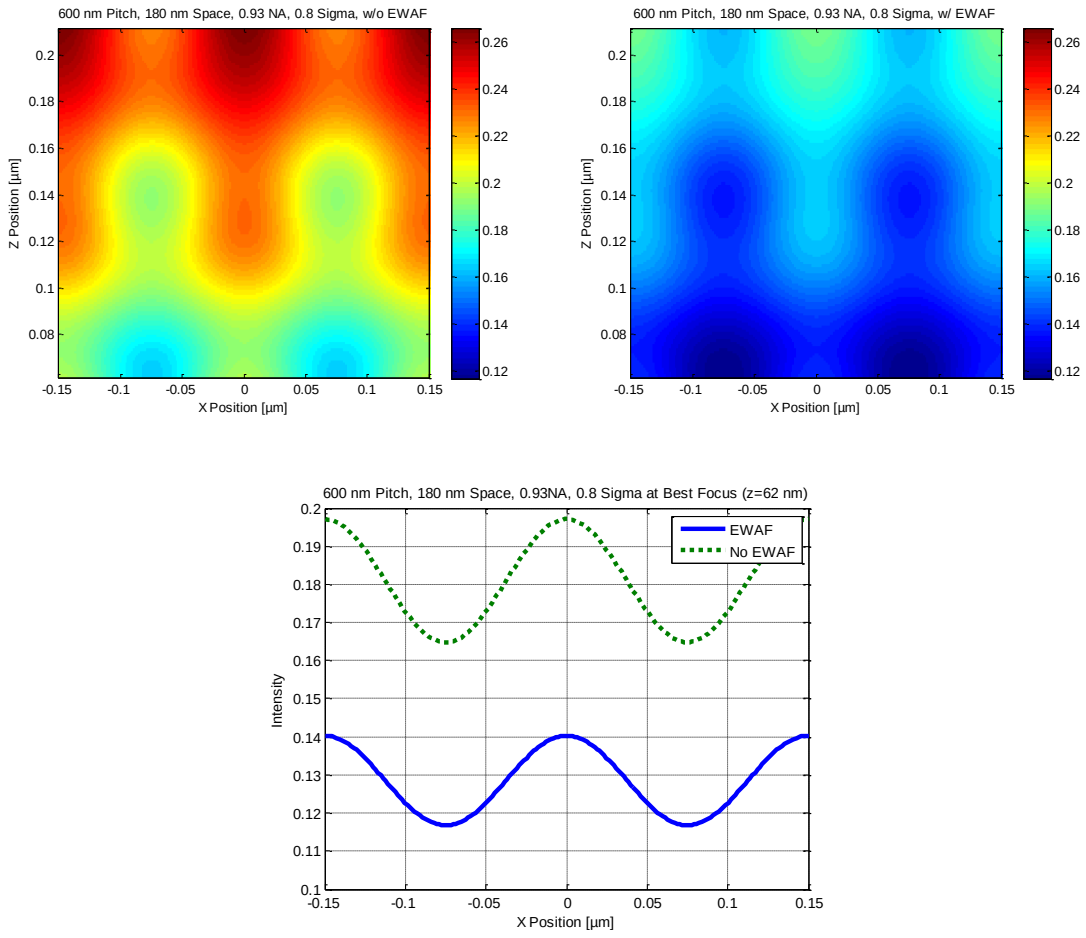


**Figure III.41: Top: X-section intensity plots of resist in the *x*-*z* plane. Best focus is at *z*=62 nm. Bottom: Cutline of the top plots at best focus. Imaging System: $\lambda$=248 nm, NA=0.93, $\sigma$=0.8.**

However, over the entire range of σ settings used for the input illumination, the 0th order is reduced. This is seen in Figure III.41 as the drop in intensity values in both the x-

section intensity plots and the cutline plot. Although imaging is occurring near the edges of the pupil in this case, the ±1st imaging enhancement factor is near 1. In Figure III.42, the angle in glass where 1st order collection begins (for negative angles of incidence) is marked.

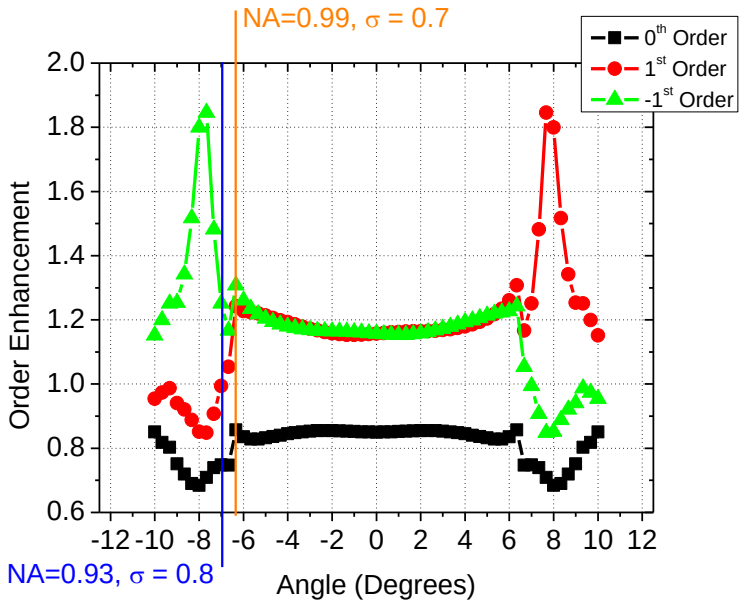


**Figure III.42: Diffraction order enhancement vs. incoming plane wave angle in $SiO_2$. Mask side angles corresponding to various NA and $\sigma$ settings are marked.**

In the next case, NA=0.99, $\sigma$=0.7, the imaging system was tuned using Figure III.42. In this case, imaging order capture was designed to begin at 6.3° where the 1st order enhancement factor is 1.24. The Rayleigh criterion for partial coherence is:

$$p_{\min} = \frac{\lambda}{\mathrm{NA}_o\left(\sigma+1\right)} \tag{3.33}$$

where $\sigma$=$\mathrm{NA}_c$/$\mathrm{NA}_o$. Here $\mathrm{NA}_c$ is known from the desired imaging collection angle, as well as the minimum pitch, $p_{\min}$ and illumination wavelength, $\lambda$. Equation

**Error! Reference source not found.** yields an $NA_o$=0.99 when the 6.3° illumination angle above is used with $\lambda$=248 nm and $p_{min}$=150 nm (on-wafer dimensions). The 1st order collection angle for this second system is also marked on Figure III.42 for comparison.

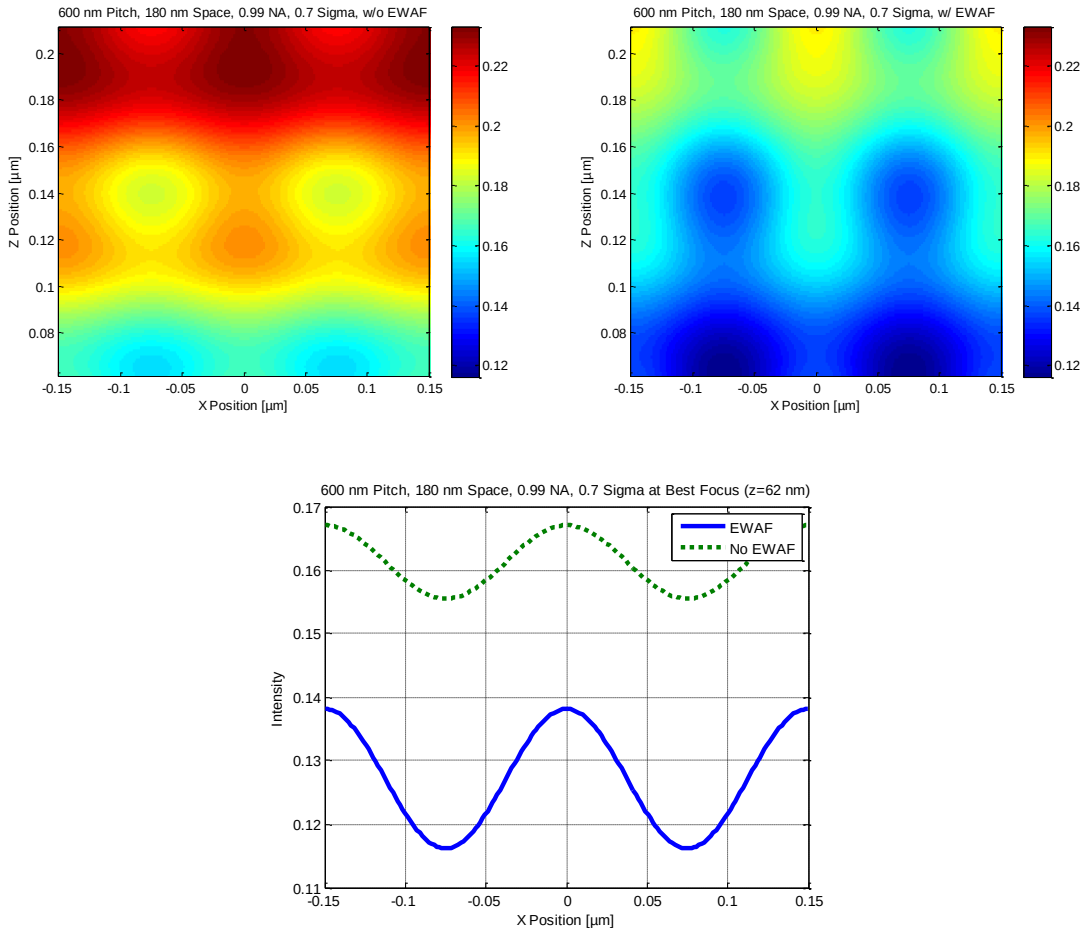


**Figure III.43: Top: X-section intensity plots of resist in the *x*-*z* plane. Best focus is at *z*=62 nm. Bottom: Cutline of the top plots at best focus. Imaging System: $\lambda$=248 nm, NA=0.99, $\sigma$=0.7.**

Results for the NA=0.99 exposure configuration are shown in Figure III.43. In this case, the evanescent wave assist features visibly reduce the background intensity of the image and clearly increase the image contrast, as seen in the cutline plot above. At best focus,

the reference case had a contrast of 0.036 and a NILS of 0.053. The design including bottom-surface EWAFs had a contrast of 0.086 and a NILS of 0.123. These values correspond to a contrast gain of 2.39X and a NILS gain of 2.32X. Although the illumination conditions are specially chosen for collection of diffraction orders where the enhancement factors are largest, this system represents the best-case gains in imaging performance.

The third system studied, NA=1.2, $\sigma$=0.55, represents a more realistic imaging situation. In this configuration, the 600 nm pitch mask will image from $\sigma$=0.55 to $\sigma$=0.32. On Figure III.42, this corresponds to plane wave angles in glass of 6.2° to 3.6°. Cross section plots for these aerial images are shown in Figure III.44.

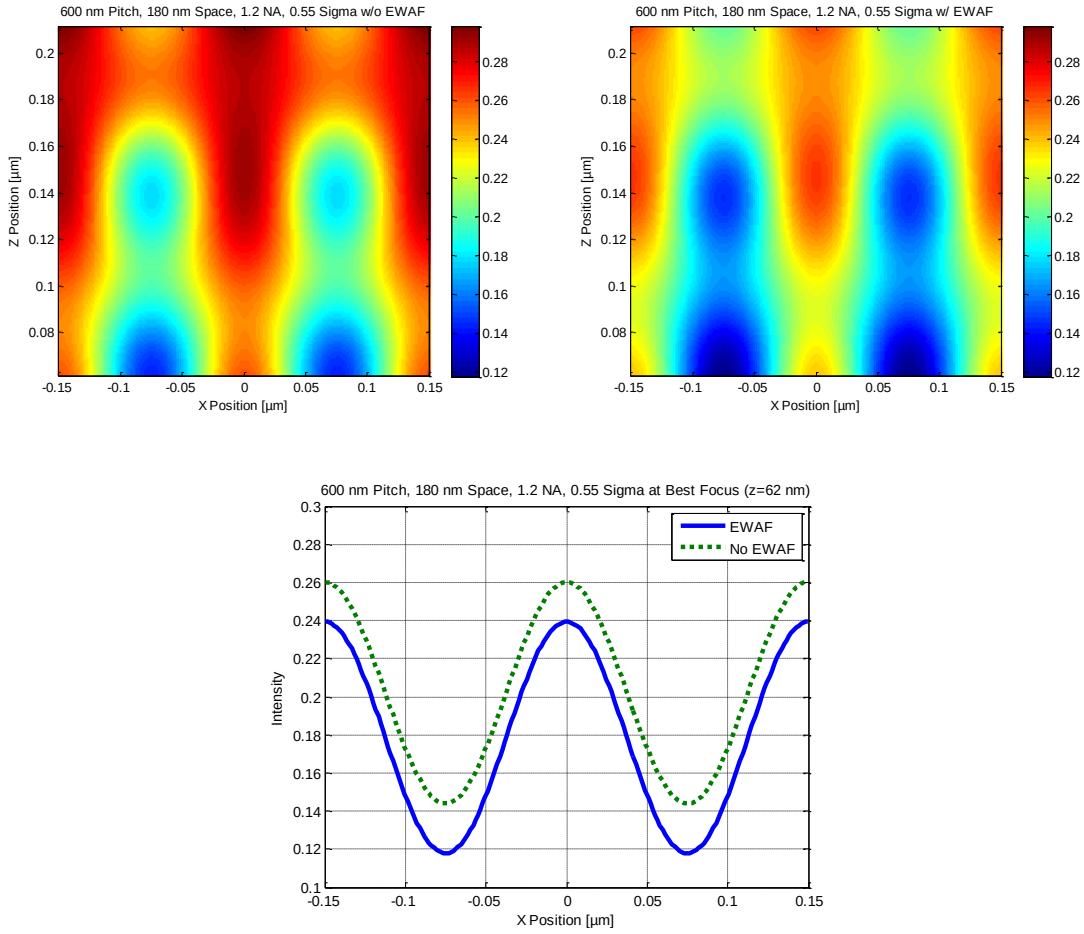


**Figure III.44: Top: X-section intensity plots of resist in the *x-z* plane. Best focus is at *z*=62 nm. Bottom: Cutline of the top plots at best focus. Imaging System: $\lambda$=248 nm, NA=1.2, $\sigma$=0.55.**

The NA=1.2, $\sigma$=0.55 configuration has an image contrast of 0.288 and NILS of 0.368 for the reference case. The EWAF photomask has improved image contrast and NILS of 0.340 and 0.423, respectively. For this imaging system configuration, the EWAFs have caused a contrast gain of 18% and a NILS gain of 15%. The lower contrast and NILS changes occur because at illumination angles where two orders are collected both 1$^{st}$ and 0$^{th}$ order are traversing the pupil at angles and are used to form the aerial image. At these imaging cases, the reduction in 0$^{th}$ order does not improve image contrast because of the imbalance between the two orders. On the other hand, from $\sigma$=0.32 to $\sigma$=0, only the 0$^{th}$

order is collected, and this negatively contributes to the aerial image. By reducing the $0^{th}$ order magnitude of this range of angles, image quality is improved. This is further illustrated by Figure III.45.

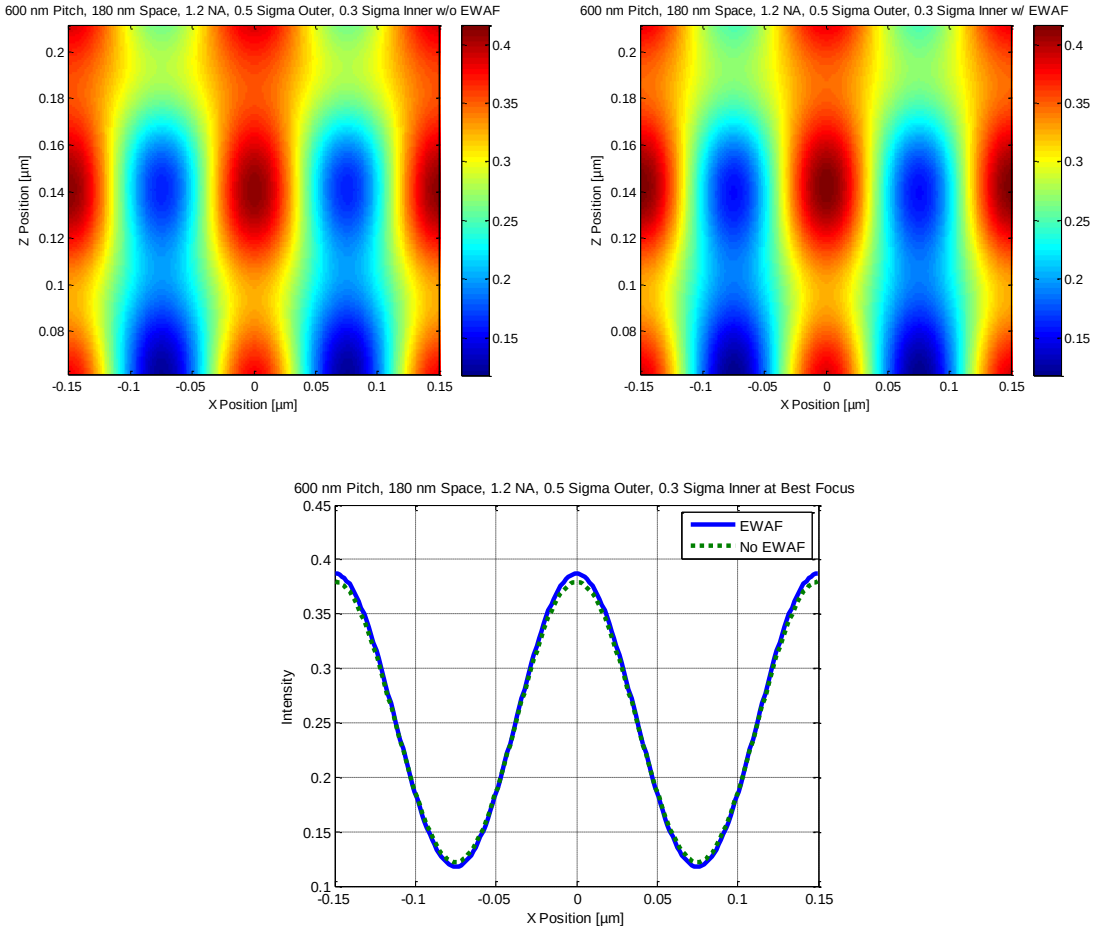


**Figure III.45: Top: X-section intensity plots of resist in the *x*-*z* plane. Best focus is at *z*=62 nm. Bottom: Cutline of the top plots at best focus. Imaging System: $\lambda$=248 nm, NA=1.2, $\sigma_o$=0.5, $\sigma_i$=0.3.**

In this case, as stated above, the changes in diffraction order balance have little effect on the aerial images, and the section of the illumination that contributes to $0^{th}$ order information has been removed. Contrast and NILS in the case with EWAFs is slightly better than the reference case with gains of 3.7% and 2.9%, respectively. It is clear from

the final imaging configurations studied that a primary influence on aerial image improvement from EWAFs is the reduction of $0^{th}$ order in illumination regions where no other orders are collected.

### (iv) Comparison with Alternative Mask Technologies

In Sections G.(i) through G.(iv), EWAFs were studied in a projection lithography system, and have shown the capability to increase image contrast and NILS of a far-field image. Increases in image contrast and NILS are in general desired in all lithographic processes because they lead to higher fidelity patterns, and processes that are more error-tolerant to uncontrollable process variation. As such, there are other techniques, such as Attenuated Phase Shift Masking that use different physical phenomena to achieve similar results. The following section will compare EWAFs and Attenuated Phase Shift Masks across similar pitches, feature sizes, wavelengths, and NAs.

Since EWAFs serve to reduce $0^{th}$ order light used for imaging while simultaneously increasing the $1^{st}$ order, the enhancement effect could be similar to Attenuated Phase Shift Masking (APSM). With Attenuated Phase Shift Masks, an absorber material is used which is partially transmitting while giving a 180° phase shift [7]. The phase-shifted light transmitted through the absorber can then destructively interfere with $0^{th}$ order energy transmitted through the mask. The amount of attenuation can be optimized to give the highest quality aerial image for a particular critical feature. Because of the 0° to 180° phase change at feature edges, the aerial image intensity is forced to go through zero, improving contrast. For the purpose of comparing EWAFs to APSM, the $p$=$d$=600 nm mask used in section G.(iii) was further studied using the NA=1.2, $\sigma$=0.55 imaging system. Using this pattern, the mask attenuation was studied

and found to be ideally 3%. Figure III.46 shows the best-focus cutlines for both binary and 3% APSM. In this case, the use of APSM improves the contrast by 24.9% and the NILS by 21% over the binary case. While performing slightly better than the EWAF reticle, the changes in the image metrics are of similar magnitude. Key differences are in the complexity of the reticle process, however. The APSM reticle features a single lithography step, where the EWAF reticle requires two lithography steps. APSM is also polarization independent, while the EWAFs require TM polarization to function. The APSM, however, may be limited by materials that can be used to deliver the required phase shift and transmission. For instance, at EUV wavelength, phase shifting materials will be difficult to find. In this regard, the EWAFs offer a customizable solution that does not depend on mask material, as long as it is significantly conducting.

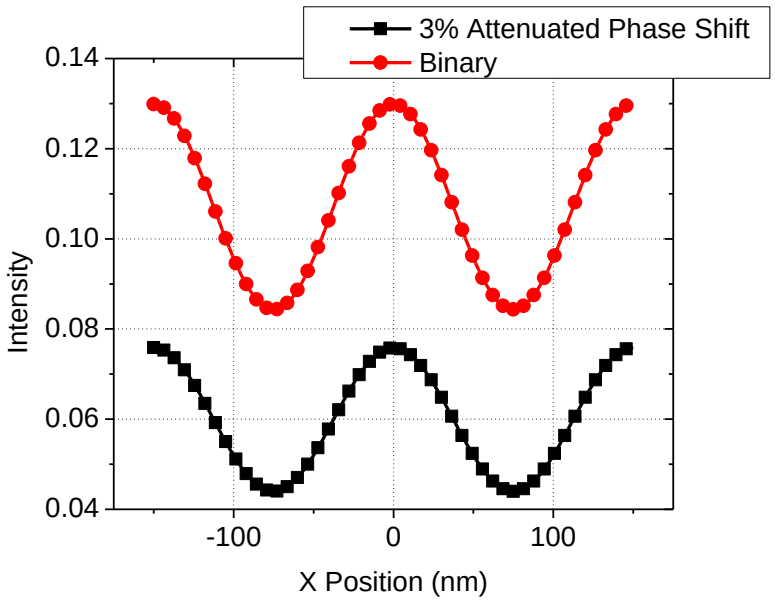


**Figure III.46: Best-focus cutline comparing resist images for p=600 nm mask features as above. 3% APSM is chosen for best contrast improvement over binary.**

### (v) SPP and Enhancement

SPP resonance coincides with cross over points of the diffraction order enhancement factors. The observed amplification/suppression of the $0^{th}$ and $1^{st}$ orders also occurs through a broad range of pitches, and only for TM polarization. To understand the role of polarization and bottom surface profile on the far-field effects, FDTD simulation was used in conjunction with several mask patterns and pitches. Aluminum absorbers with $t$=90 nm were investigated without transmitting features to gauge the material's ability to support SPP and similar field enhancements at interfaces. Full simulation parameters include $\lambda$=250 nm, TM polarization, normal incidence, and periodic boundary conditions. Figure III.47 shows simulation output for a sinusoidal grating with 15 nm amplitude and 236 nm and 242 nm pitches. The $p$=236 nm grating corresponds to SPP resonance while the $p$=242 nm grating represents the primary harmonic of bottom surface profiles of near-resonance designs that still show polarization dependent responses.

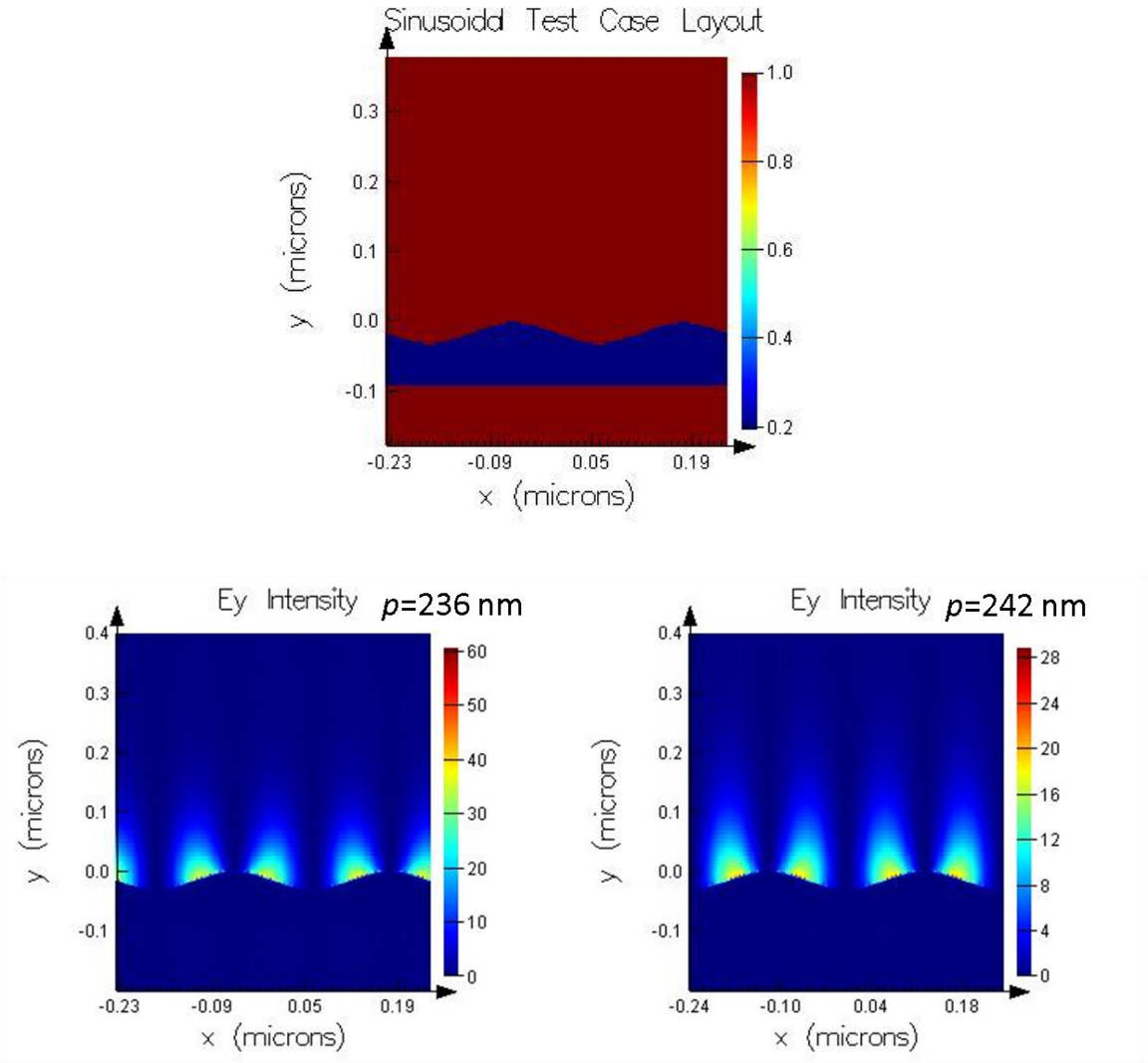


**Figure III.47: $E_y$ intensity for sinusoidal corrugations at indicated pitches under $\lambda$=250 nm, TM polarization.**

The intensity component of the vertical, *y*-direction, electric field is shown, along with scale bars for reference. The *y*-component intensity is particularly interesting because this component is greatly amplified at SPP resonance. Although the fields at *p*=236 nm are more intense in Figure III.47, there is also an intensity enhancement for the off resonance pitch of 242 nm. These simulations can be further extended to square grating designs with the same simulation and pitch parameters.

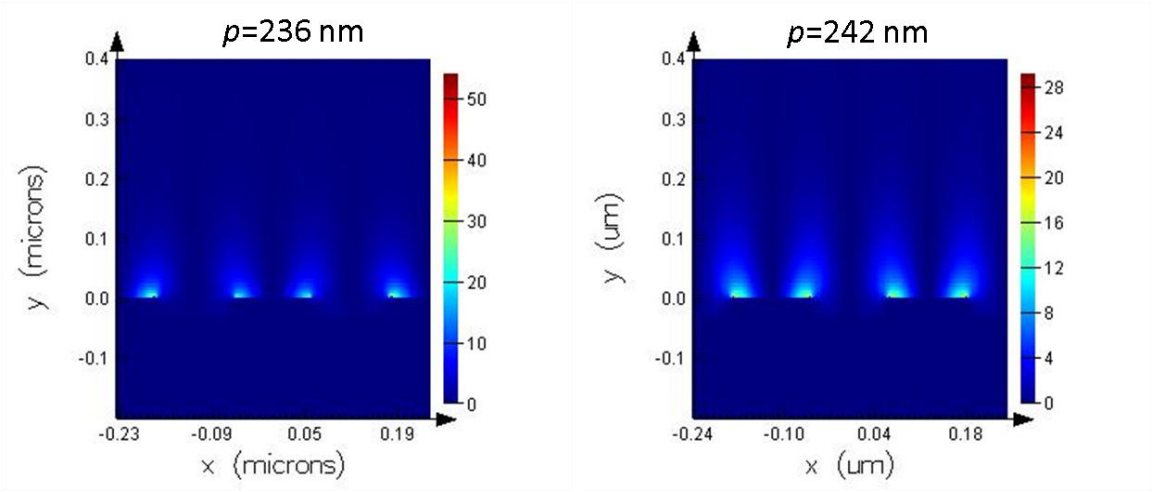


**Figure III.48: $E_y$ intensity for square corrugations at indicated pitches under $\lambda$=250 nm, TM polarization.**

Figure III.48 shows these intensity profiles for square wave surface profiles. While the *y*-component intensity is not as high for the surface waves of either case, even the off resonance case of *p*=242 nm has significant surface wave intensity.

Since Figure III.37 shows significant changes in the diffracted orders through pitch, and crossovers of the curve which roughly coincide with SPP resonance, the *y*-component of the electric field can be studied through pitch to determine if the surface fields are being amplified over the range of pitches. Figure III.49 and Figure III.50 show a square-wave surface profile studied from *d*=235 nm to 469 nm, the range of pitches the surface corrugations occupy in Figure III.37. The groove feature is 30 nm deep (*h*), 124 nm wide (*a*), and the absorber material is Al.

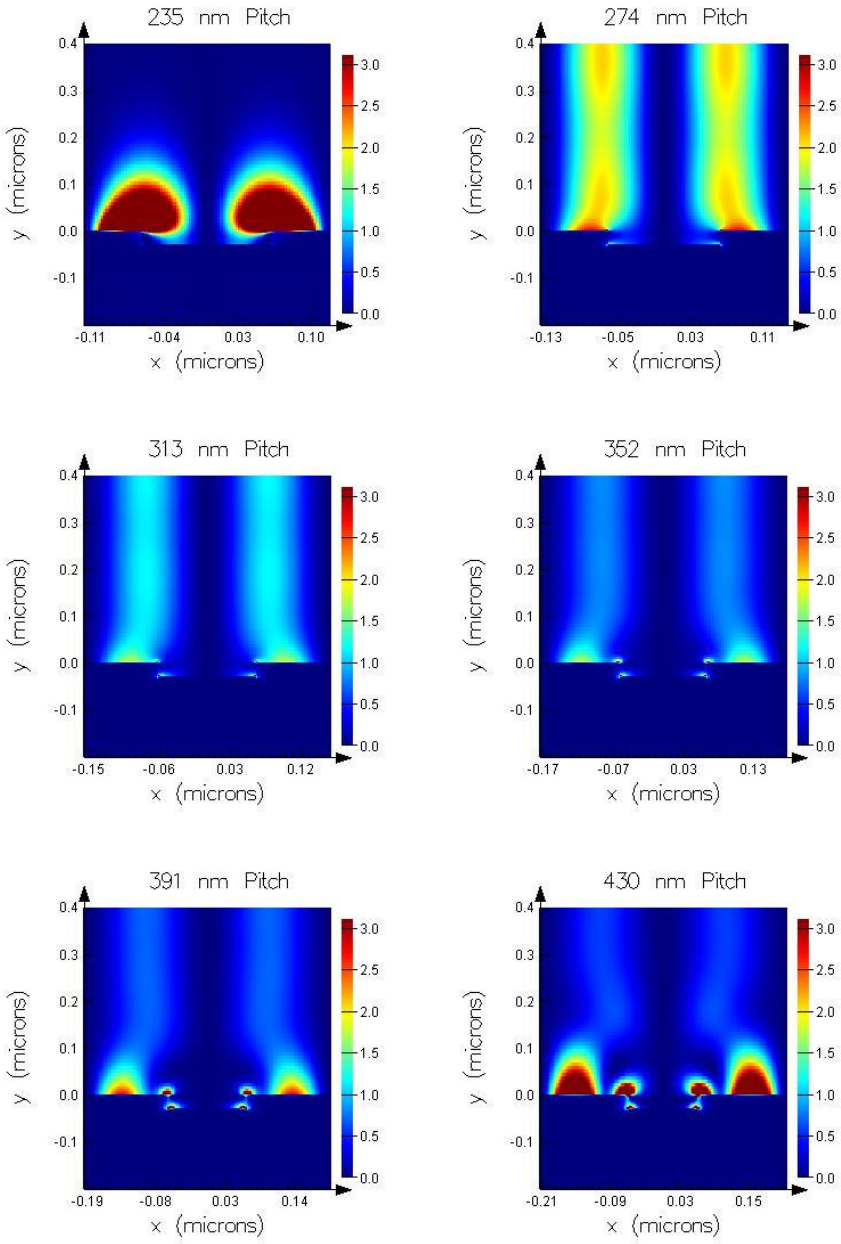


**Figure III.49: Square groove with *a*=124 nm, *h*=30 nm, *d*=235 nm through 430 nm. Intensity of the *y* component *E* field is shown.**

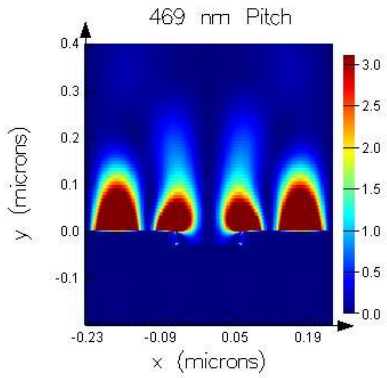


**Figure III.50: Figure III.49 continued. Square groove with *a*=124 nm, *h*=30 nm, *d*=469 nm. Intensity of the *y*-component *E* field is shown.**

Although the *y* component intensities (and therefore fields) are strongest at the two extremes near SPP resonance, the plots indicate that mild *y*-component field amplification is taking place over the entire range of pitches. Although not at resonance, this SPP-like *y*-component field is likely responsible for the observed change in diffracted orders under TM polarization.

The results of the above sections suggest that grating coupling between the transmitting grating and EWAF gratings are primarily responsible for the observed shifts in diffraction order amplitudes. The coupling occurs when the gratings support identical evanescent modes. In the case where the EWAF features are etched into the mask substrate, the refractive index of fused silica must be taken into account, which limits the layouts that can be used. For bottom-surface EWAFs, the gratings can be integer multiples of pitch. Equally important is the field enhancement the conductive absorber generates. Even at non-resonance, field components normal to the surface are amplified. Since these evanescent components have more amplitude, when they are converted back to propagation by the bottom surface grating the resulting orders have more energy, which can then have greater influence on propagating orders emanating from the

transmission grating. This also explains the enhancement's dependence on polarization, since for TE polarization, there is no surface normal component of the electric field, and the net effect of EWAFs is negligible.

In this chapter, specifics of Evanescent Wave Assist Features have been presented. The two main types of layouts studied were presented in schematic, and parameters were assigned to important dimensions, such as EWAF pitch and main feature pitch. The methods used later in the chapter for analysis of EWAFS were presented next. These included details on FDTD simulation of the reticles and a description of why rigorous simulation was necessary. Since EWAFs were used in projection lithography, lithographic simulation was discussed. After the mask output traverses through simulation of the optical system, the converging plane waves were passed into a thin-film stack simulation, which accounted for multiple reflections and polarization effects.

Metrics by which the diffracted orders and aerial images were evaluated have been presented. In particular, these included the diffracted order enhancement factor, the Degree of Enhancement, and also more common aerial image metrics, such as NILS and image contrast. Using these metrics, EWAF features in both 1 and 2-dimensions have been simulated in order to understand the EWAF's physics of operation. By adding the features to appropriately designed photomasks, a 15% reduction in $0^{th}$ order amplitude was shown, along with a simultaneous 16% increase in $1^{st}$ order electric field amplitude. Analyzing these photomasks in a projection lithography application indicates a best-case image contrast and NILS improvement of over 2X. More practical illumination settings at NA=1.2 and $\sigma$=0.55 indicate the features improve image contrast and NILS by 18% and 15%, respectively. Further analysis using DoE and enhancement factors of the diffracted

orders from reticles has shown that conductive absorbers increase the magnitude of observed enhancement. This observed enhancement is highest in magnitude in cases where the EWAFs were fabricated along the air/absorber interface. Surface Plasmons also play a central role in the operation of these structures. Results show that at SPP resonance, DoE changes polarity for $0^{th}$ and $1^{st}$ orders. Further evaluation of corrugated structures using FDTD methods shows that while field amplification is indeed strongest at SPP resonance conditions, fields were amplified though a range of pitches. This electric field amplification and subsequent observed shifts in diffraction order magnitudes when EWAFs were present suggest that this weak resonance plays a central role in the operation of Evanescent Wave Assist Features.

# IV. FABRICATION AND TESTING

This chapter will cover the fabrication and testing of a prototype EWAF mask. Section A introduces the process flow and techniques used for fabrication. Section B introduces the exposure tools built for fabrication and used for the test mask. Section C discusses the critical aluminum etches used to transfer the interference patterns into the metal absorber. Section D discusses the specifics of the fabrication of the prototype and reference masks. Finally, Section E will detail the testing of the prototype and reference masks.

## A. Process Flow

The fabrication process started with a 100 mm diameter, 580 μm thick UV-grade fused silica wafer. The only difference between this substrate and a standard 6”x6”x0.25” mask blank is its thickness and diameter. The thickness difference allows the substrate to be processed in ways that are more compatible with standard silicon based methods. The size differences are not necessarily important because both substrates would have to be cut. A schematic of each step in the process is included in Figure IV.1.

### (i) Dicing and Cleaning

In order to maximize the number of test chips that could be made from the limited amount of wafers, the silica substrates were first diced on a Tempress dicing saw [78]. Prior to dicing, the substrates were coated with Shipley 1813 photoresist at 1000 RPM to protect the top surface during processing. This type of saw uses a diamond impregnated blade and a stream of De-Ionized (DI) water to cool the sample and blade. The 100 mm

wafers were cut into 20 mm × 20 mm pieces, using a standard blade and a slow blade feed setting.

After dicing, the wafers were stripped for 20 minutes in 90 C PRS-2000 to remove the protective photoresist. The pieces were then processed using a modified RCA clean [79], [80] to remove as much contamination as possible. The process' APM and HPM baths were used, while the dilute hydrofluoric (HF) acid step was skipped to avoid etching the substrates.

**(ii) Metallization**

Aluminum was deposited using a Perkin Elmer 4410 RF sputtering system [81]. This type of sputtering system operates by applying a 13.56 MHz RF signal to a capacitively coupled target made of the material to be deposited. RF sputtering offers flexibility in the types of materials that can be deposited. Typical DC bias sputtering can only deposit suitably conductive materials since insulating targets cannot reach required current densities using reasonable applied cathode voltages. However, under the application of an RF signal, the target "self-biases" and behaves similarly in operation to a DC bias sputtering system. This allows the use of insulating materials as targets. Under this steady state, cations bombard the target similarly to a DC bias system [82]. Although RF sputter systems are generally desirable for their ability to sputter insulating materials, they can also sputter conductive materials. In this case, the PE 4410 was chosen because it is a load-locked system, meaning that the sputtering chamber is always under high vacuum, in the low $10^{-7}$ Torr range. This capability allows films to be deposited rapidly by avoiding the typically several hour pumping time after loading the tool. Purity of the deposited Al should also be higher, since the chamber vacuum remains lower at all times,

and also because the PE 4410 is among the highest vacuum tools in the SMFL. The PE 4410 is also a sputter-down tool, meaning that the sputter target is suspended above the substrates. Pieces may simply be laid on the chuck without needing to be taped or otherwise held in place. Although deposition rates are slower in the PE 4410 compared to other sputtering tools available in the SMFL, this is an advantage in this case because the film thickness required is small, making the deposition more repeatable.

The desired Al thickness was 90 nm and was characterized using a Tencor P-2 profilometer in high sensitivity mode. Film thickness was also verified during other measurements in a Scanning Electron Microscope (SEM). Clean samples were loaded into the 4410 and allowed to pump until a base pressure of 3.8e-7 Torr for maximum film purity. Sputtering conditions were previously optimized for this low thickness to ensure acceptable film quality. The samples were sputtered at 400 W RF at 3 mT process pressure and a flow of 25 sccm of Ar. Table rotation of 300 was used to get more controllable deposition rates on these samples. The sputter time was approximately 13 minutes to achieve the 90 nm target Al thickness. Along with the cleaned diced fused silica pieces, a large amount of cleaved Si pieces were also loaded for process testing purposes. The same run was used for both types of samples to eliminate any variation in deposited Al in the test pieces.

### (iii) First Layer Lithography

Interference lithography was used to define the surface relief features required on the EWAF reticle. Interference lithography is introduced as a process step here, but is presented more completely in Section B of this chapter. These surface-relief features were defined first since their small size may make them more sensitive to reflections

caused by surface topography. A bench-top interference tool was used, which will be described in Section B. This tool has the advantage that its NA can be customized to match exact exposure requirements and a uniform exposure spot of approximately 6 mm diameter can be made. The first exposure was done at approximately 0.40 NA, with an intended pitch of 242 nm. To address alignment issues, a jig was made to hold the sample in the same position during both exposures.

#### (iv) Surface-Relief Feature Etch

The features defined in the first exposure are transferred into the underlying Al layer using Reactive Ion Etch (RIE). In this type of etching, reactive etching species are created in a plasma. The chuck holding the sample has a DC bias such that ions in the plasma are attracted to the sample and contribute to material removal [83]. The LAM Research 4600 Rainbow is used for Al etching [84]. The first lithography step defines the bottom-surface relief (air/absorber interface) features on the absorber shown in the bottom part of Figure III.2. In this case, etch rates were calculated using dummy test pieces that were destructively analyzed. Actual device pieces used etch times bracketed from these test etches. Details of process recipes and experiments will be presented in Section C.

#### (v) $O_2$ Plasma Clean

After pattern transfer, the remaining photoresist and BARC from the 1$^{st}$ layer etch was stripped in the Trion Minilock using an $O_2$ plasma [85]. The process recipe used 20 sccm $O_2$, 150 W forward RF power at 150 mT, and a processing time of 180 seconds. The pieces were stripped one at a time using a milled carrier wafer to adapt the tool for processing the small samples.

### (vi) Second Layer Lithography

Interference lithography was again used to define the main features of the pattern in the second and final imaging step. These features were patterned at an NA of ≈0.20, corresponding to printed patters of 484 nm. The patterns of the second exposure are intended to be exact multiples of the first layer so that some grooves will be exposed and then etched away. The bench-top interference lithography tool was used in an iterative process for this layer definition. Several test exposures were performed, then measured, and the NA of the tool was then adjusted until the correct pitch was achieved. Samples were carefully aligned to the jig to minimize misalignment between the two exposures.

### (vii) Transmitting Feature Etch

The 484 nm features were transferred down to the substrate, through the 90 nm thick Al layer. This second layer etch time was adjusted for time, as well as chemistry to achieve a higher etch rate and the anisotropy required for good pattern transfer. The details for the second etch will also be described in Section C.

### (viii) Final $O_2$ Plasma Clean

The Trion Minilock with $O_2$ plasma was again used to remove remnants of photoresist and BARC used in the second etch. An identical recipe was used to the first cleaning step.

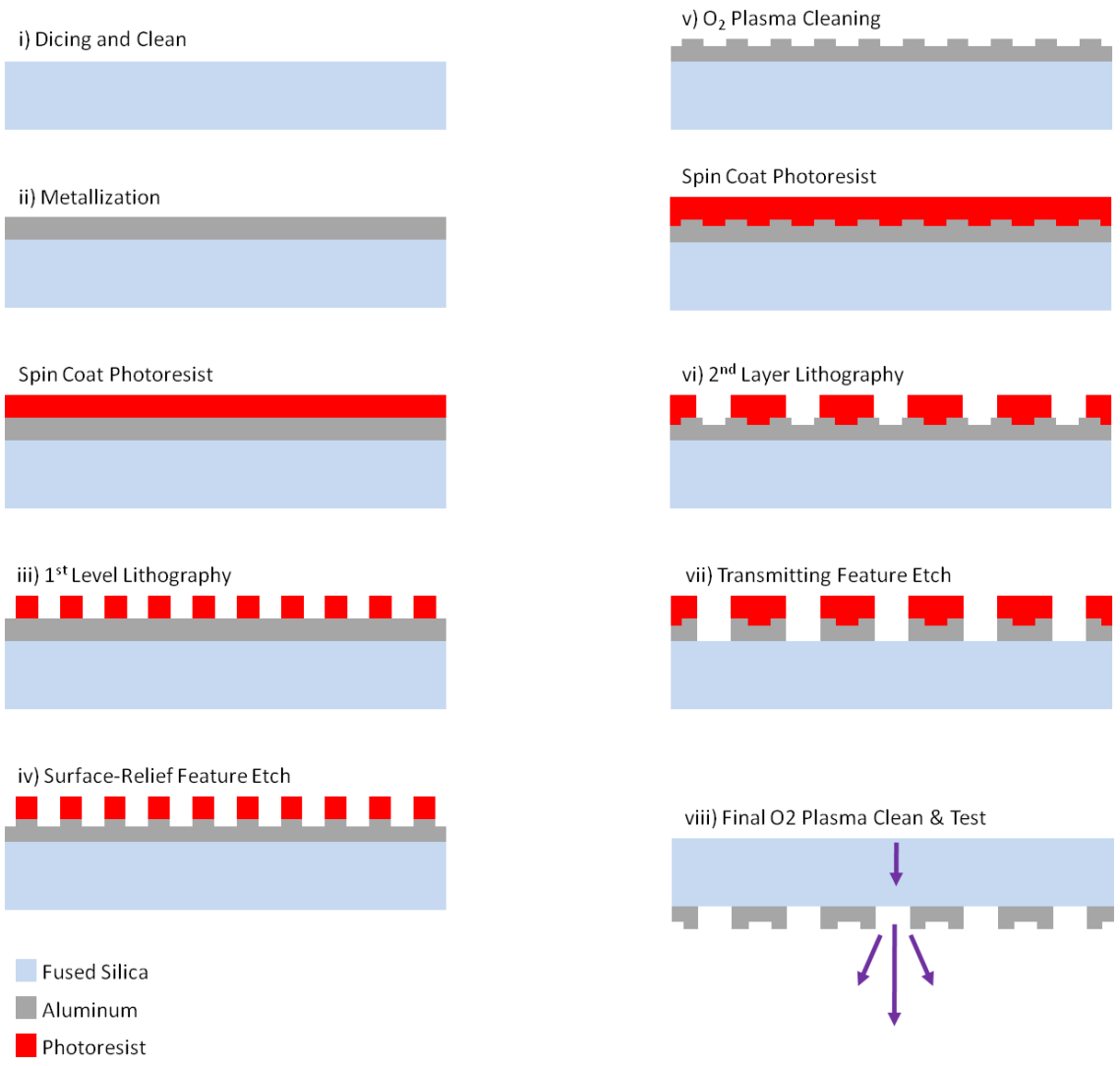


**Figure IV.1: Schematic of the process flow used to fabricate EWAF devices. Reference devices are identical with steps (iii), (iv), and (v) omitted.**

### B. Interference Lithography

Interference lithography is an important research tool that has been successfully used to explore material capabilities and screen new materials, test the limits of optical lithography, and evaluate novel photoresists and immersion fluids [86-88], [72]. In this work, interference lithography has been used to pattern working EWAF devices. This section will detail the lithographic processes used.

The devices were patterned using the bench-top interference tool shown in Figure IV.2 [86].

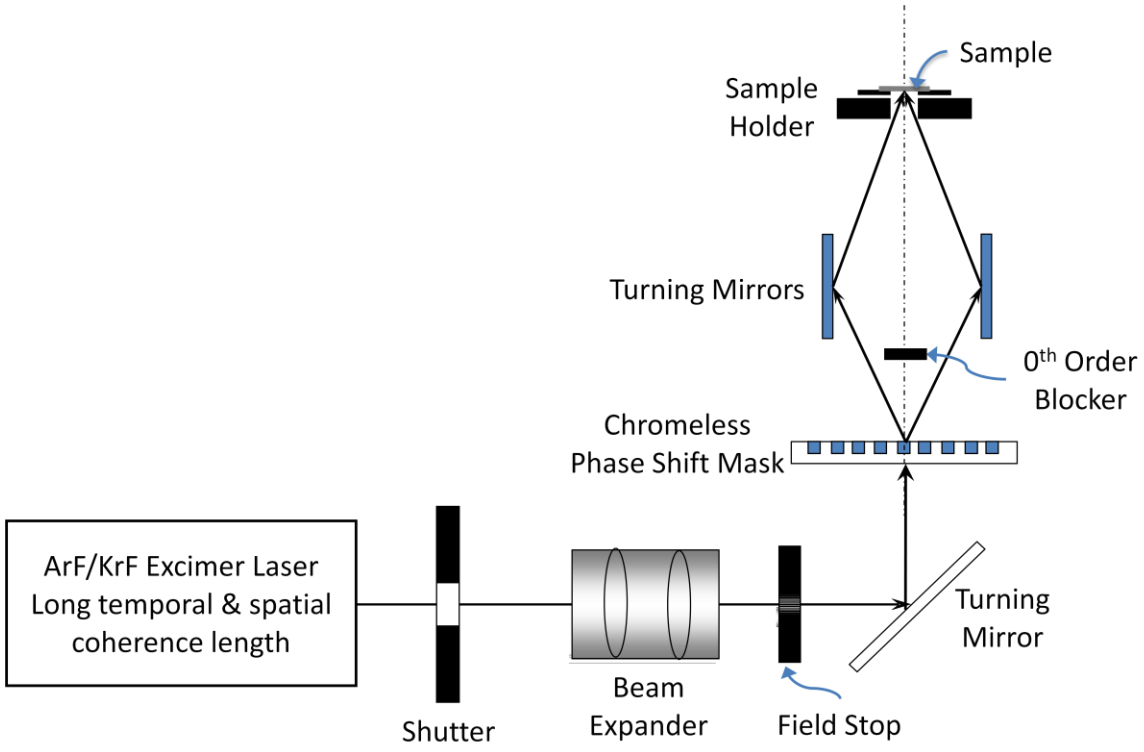


**Figure IV.2: Schematic of the bench-top interferometer used for lithography [86].**

The highest resolution exposure performed for EWAF fabrication was at 0.40 NA. A new sample holder was required for holding the sample, since all other versions of this particular setup have used a prism or half-ball. The sample holder is shown in Figure IV.3 below in more detail.

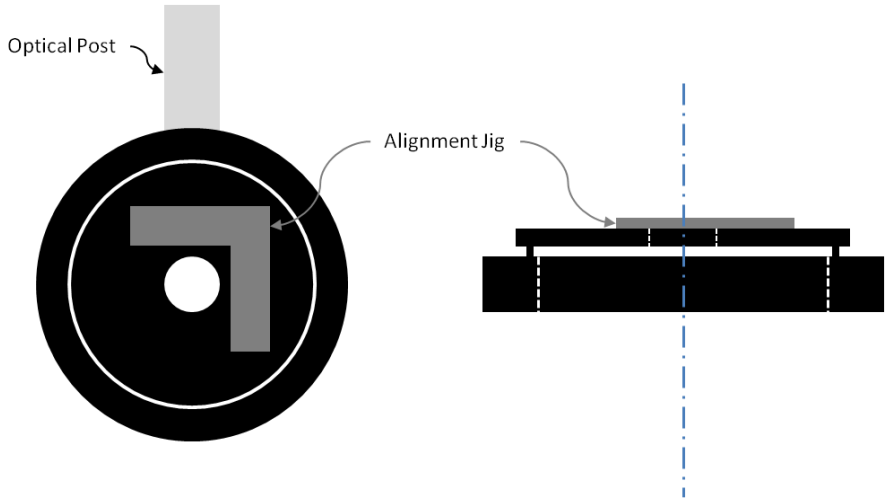


**Figure IV.3: Sample holder used for low-NA lithography.**

This sample holder was modified from that used to accommodate the half-ball, however an extra plate is added. The sample was inverted and aligned against this plate, using the right angle of the alignment jig. The angles used for exposure can be calculated using [89]:

$$p = \frac{\lambda}{2n_{\text{medium}} \sin\theta} \tag{4.1}$$

For this case, no immersion medium was used, and $n_{\text{medium}}$=1. Assuming a mirror spacing of 4" center-to-center, the distance from mirror center to optical axis (assuming kinematic mounts) is 2". The half-angle described by this right triangle is the NA of the exposure. At 0.40 NA (242 nm) this corresponds to an angle of ≈23.5°. The *z* distance from mirror centers to sample along the optical axis is 4.599" in this case. If the exposure is adjusted to be 1 nm larger in pitch, the corresponding *z* distance is 4.622". The *z* difference between these two sample exposure heights is 0.584 mm. The resolution of the Newport 462 series micrometer stage that adjusts the sample *z* height is 1 μm when the vernier scale is used, well within the sensitivity this exposure step requires for nm level pitch

control. The second exposure step was performed at approximately 0.20 NA. This corresponds to a desired printed pitch of 484 nm. If the analysis above is repeated, the exposure height required is 11.5", and the height control necessary to control pitch to the nm level is now 0.54 mm. This is also well within the accuracy of the micrometer stage.

The pieces were tested on a Woollam Variable Angle Spectroscopic Ellipsometer (VASE). This type of ellipsometer uses multiple wavelengths of linearly polarized light, and scans the wavelengths over many angles of incidence to find nulls in a detected intensity. By analyzing the nulls of the reflected elliptically polarized light from the sample, $\psi$ and $\Delta$ values can be determined over angle and wavelength. This allows the ellipsometer to simultaneously determine film thickness and refractive index. In this work, the VASE is used in scatterometer mode. Under this mode of operation, the source polarization and wavelength can be selected and the sample held at a fixed angle, while the detector is swept over a cone of angles. The intensity and angular direction of diffraction orders can be detected in this way.

Since the source is approximately 5 mm in diameter, it is important that the dose be as uniform as possible over the exposure spot to minimize linewidth variation. This is normally accomplished with spatial filtering using a singlet and a pinhole. In this case the spatial filtering setup was not used because of the increase in exposure time, complexity, and real-estate requirements of the system. A test exposure near the desired pitch is shown in Figure IV.4. This confirms that the uniformity of the field is not adversely affected by the omission of the spatial filter.

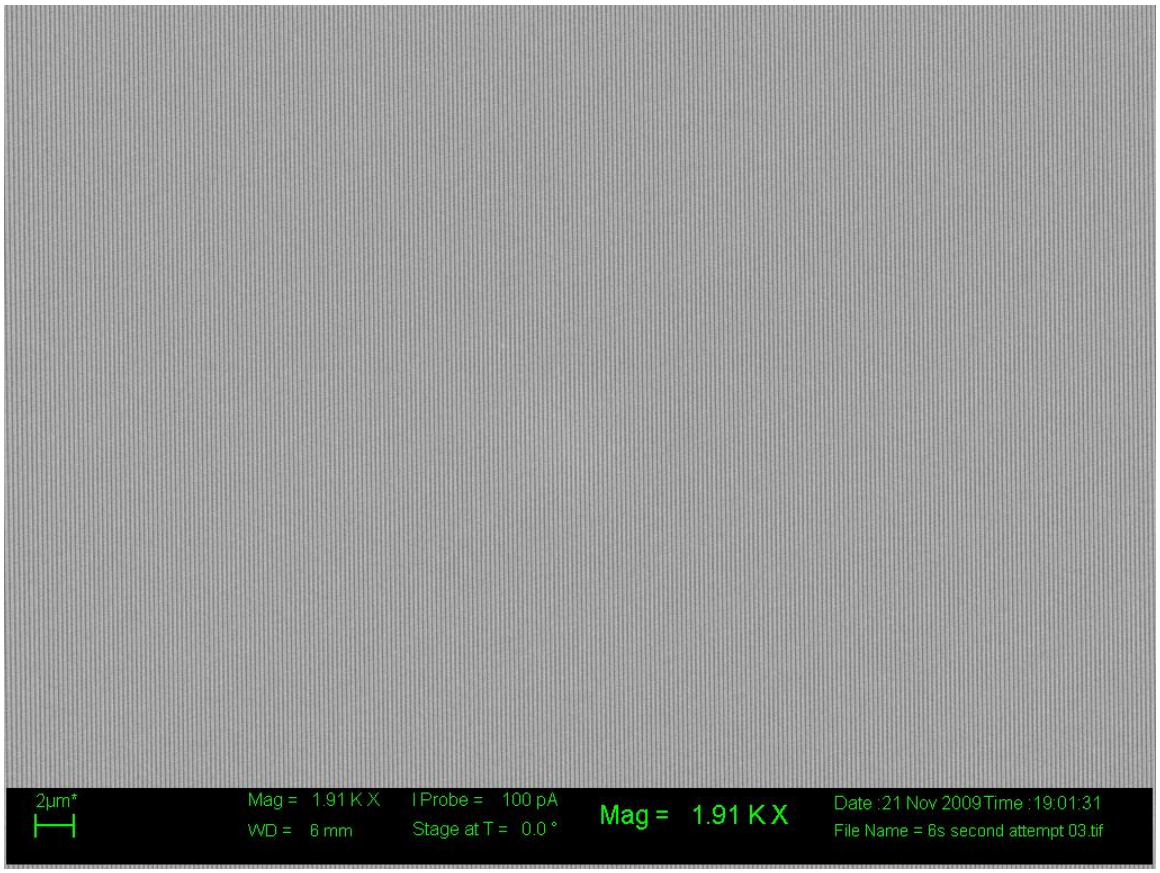


**Figure IV.4: Test exposure on at *p*=236 nm showing good field uniformity. Exposure time is six seconds.**

The patterns must also be transferred to the underlying Al layer, which presents a challenge since Al is highly reflective. This reflectivity is usually minimized using an organic Bottom Anti-Reflective Coating (BARC). Typical RIE recipes may use small amounts of $O_2$ in the plasma to help break through organic BARCs quickly and begin etching of the desired material. In the case of Al, however, oxygen cannot be used since it will readily oxidize the film and make removal difficult. To minimize the amount of BARC left in the developed spaces, a dilute BARC was made using Propylene Glycol Monomethyl Ether Acetate (PGMEA). This yields a coat of approximately 30 nm at 3400 RPM and allows coating of the Brewer ARC29A-8 used at the first minimum

reflection thickness. This still allows a reduction in substrate reflection, and is also easier for the etch to penetrate.

The original bench-top exposure tool used standard 25 mm mirrors held in kinematic mounts. At the lower NAs needed to expose suitable geometries for EWAF samples, the mirrors were not large enough and caused beam clipping and loss of field. New mirrors were fabricated using cleaved silicon pieces approximately 2” × 2” affixed to the front surface of the mounts. These were first coated with high quality Al, 90 nm thick, from the CHA flash source evaporator at a base pressure of 1.9e-7 Torr and a planetary rotation of eight [90]. These new mirrors provided the necessary flatness, reflectivity, and size to record high quality, large area interference patterns at low NA.

The 0.40 NA exposures used Dilute Hexamethyldisilazane (HMDS) to achieve better adhesion between BARC and aluminum. Dilute Brewer Science ARC29A-8 was used as an anti-reflective layer, coated to a first minimum thickness of 31 nm. JSR ARX2928, a positive chemically-amplified ArF (193 nm) photoresist, was also used and coated to 139 nm thick. This coating thickness corresponds to an 800 RPM spin speed, the slowest that would still allow a good quality coat. Resist processing details for the 0.40 NA exposure are presented in Table IV.1. The exposure time to print 1:1 duty ratio patterns was 5.5 s. SEM images taken on silicon test pieces for pitch calibration are shown in Figure IV.4, Figure IV.5, and Figure IV.6. These particular test pieces have CHA flash source deposited Al.

| Step | Material | Time | Temperature/Speed |
|---|---|---|---|
| **Dehydrate** | | 120 s | 200° C |
| **Coat** | HMDS | 60 s | 2648 RPM |
| **Activation Bake** | | 60 s | 110° C |
| **BARC Coat** | ARC29A-8 | 60 s | 2648 RPM |
| **BARC Bake** | | 90 s | 200° C |
| **Resist Coat** | ARX2928 | 60 s | 800 RPM |
| **Post Apply Bake** | | 90 s | 110° C |

**Table IV.1: 0.40 NA exposure coating parameters.**

| Step | Material | Time | Temperature |
|---|---|---|---|
| **Post Exposure Bake** | | 90 s | 110° C |
| **Develop** | CD-26 (0.26 N TMAH) | 60 s | |
| **Hardbake** | | 60 s | 120° C |

**Table IV.2: Standard Development Parameters.**

As described in Section A, pitch and CD adjustments were made iteratively. CD and duty ratio was controlled with exposure time and pitch was adjusted by adjusting the *z* exposure height of the sample. Although the larger Al coated Si mirrors were no longer kinematic, existing exposure heights could be calculated from SEM measurements and accurate height could be determined. The height of the desired pitch was then calculated, and the *z* micrometer adjusted by this difference in heights. By repeating this process, the pitch converges to the desired dimension. Fabricated patterns had less than a single nm pitch error as measured by line scans over 10 periods. Measurements of pitch and groove CD are shown below in Figure IV.5 and Figure IV.6, respectively.

The 0.20 NA exposures used a similar coating and exposure process to those listed in Table IV.1 and Table IV.2, with an optimum BARC coat of 31 nm and resist coated to a thickness of approximately 150 nm. Brewer ARC29A-8 and JSR ARF2928

were again used as BARC and photoresist. After several iterations and adjustments, the 484 nm pitch was imaged successfully over the Al layer. These test pieces have Al deposited via RF magnetron sputtering in the PE 4410 using the process described in section A.(ii). A consequence of the RF sputtering and RIE $O_2$ strip steps is a slightly rougher Al than evaporated films. This is visible in the SEM pitch measurement micrographs, Figure IV.7 and Figure IV.8. The visibly rough Al contributes to higher reflection, which then increases line edge roughness, also visible in the micrographs.

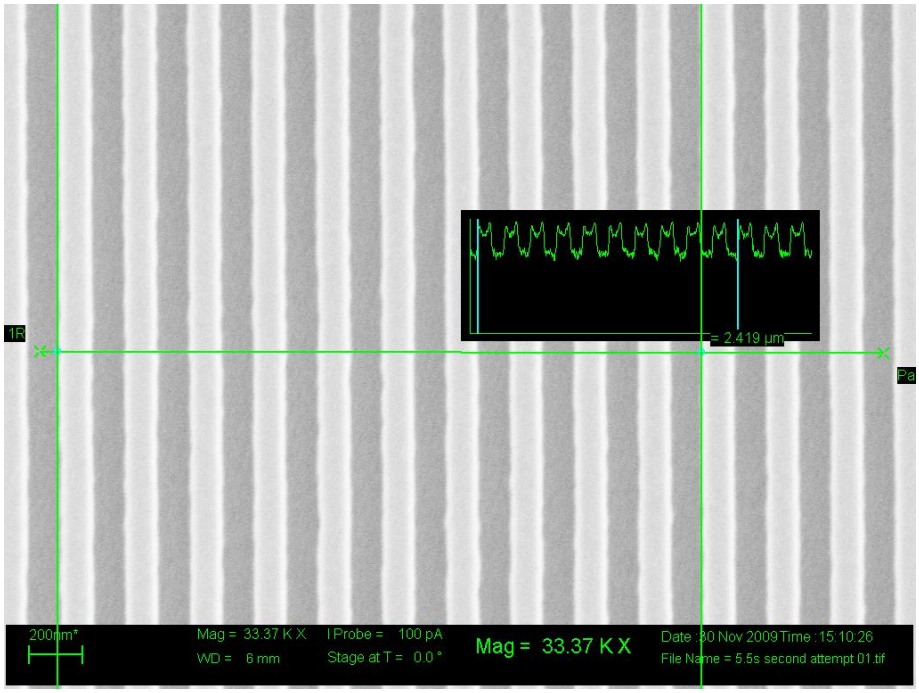


**Figure IV.5: 0.40 NA exposure with pitch measurement over 10 periods. Total pitch is measured by line scan to reduce error. Total Measurement=2.419 µm, Pitch (*d*)=242 nm.**

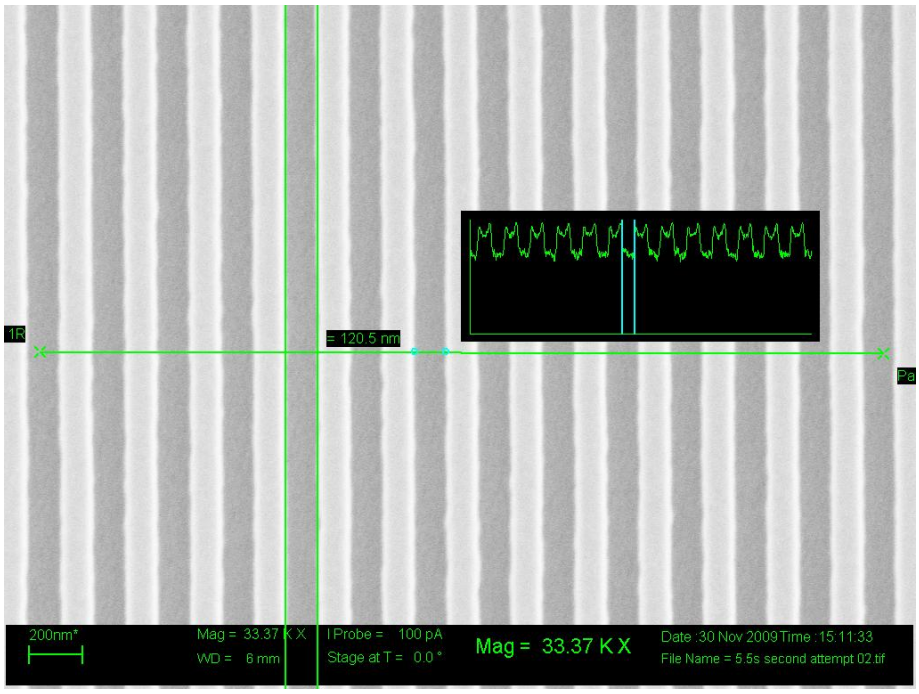


**Figure IV.6: Groove measurement (*a*) of the same exposure as Figure IV.5. *a*=120.5 nm.**

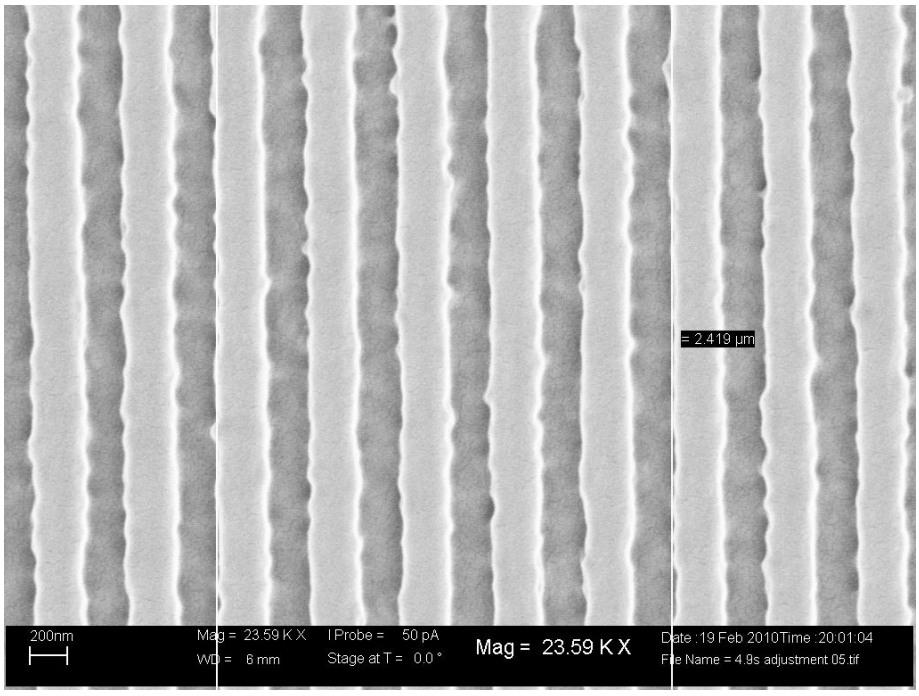


**Figure IV.7: 0.20 NA exposure with pitch measurement over 5 periods. Average pitch calculated over 7 locations is *p*=484 nm.**

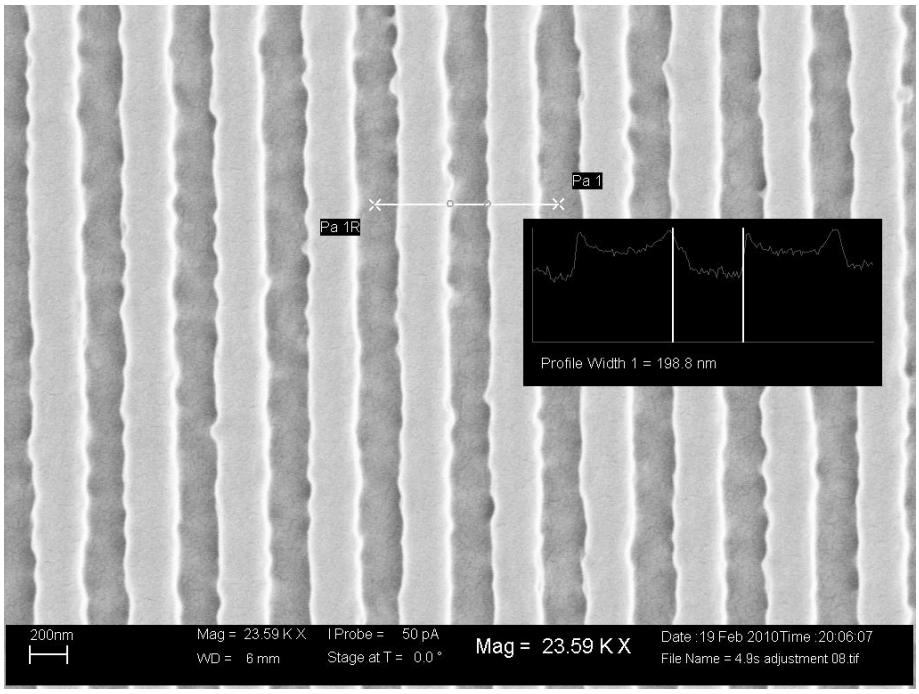


**Figure IV.8: Transmitting slot width (*w*) of Figure IV.7. *w*=199 nm.**

### C. Aluminum Etch

The second major fabrication step is the pattern transfer of the lithography to the underlying aluminum layer. This is accomplished through chlorine-based RIE. The LAM Research 4600 Rainbow chlorine etcher used at the SMFL has several process gases that each serve different purposes. These are listed and described in Table IV.3 [91].

| Gas | MFC Size | Function |
|---|---|---|
| **$BCl_3$** | 100 sccm | Punch through native oxide, ballistic and directional, also getters oxygen from chamber |
| **$Cl_2$** | 200 sccm | Etch Al, isotropic, selective |
| **$O_2$** | 10sccm | Etches organics, removes sidewall polymer |
| **$N_2$** | 200 sccm | Boosts plasma ionization, which increases directionality of etch |
| **$CHCl_3$** | 42 sccm | Forms polymer for sidewall protection |

**Table IV.3: Etch gases, maximum flows, and functions of gases plumbed to the SMFL LAM Research 4600 Rainbow.**

There are several important process factors that influenced recipe selection for this section. Since the samples are pieces that need a carrier wafer, conduction from the chuck through the pieces was low. In order to get significant DC bias on the chuck, relatively high RF power was used. Also, the experimental ARX2928 resist suffers from erosion when exposed to plasmas for long times. The recipes therefore have their etch times at or below 30 s. Oxygen is typically used in RIE to increase removal rates of organic materials such as BARC, in order to expose the intended layer [92]. In the case of Al, however, addition of $O_2$ to the process may form a more durable oxide that is difficult to remove once the exposed BARC is removed. In these processes, a thin BARC is coated to correspond to the first minimum reflection. The resist tolerates this low amount of reflection and image fidelity is not significantly worsened. The thin BARC is then etched using $BCl_3$ at high power. Once the BARC is clear, the $BCl_3$ can penetrate the $Al_2O_3$ layer without contributing to a thicker oxide formation.

The recipe used for transferring the 0.40 NA patterns is shown in Table IV.4.

| Parameter | Step 1 | Step 2 | Step 3 | Step 4 | Step 5 | Step 6 |
|---|---|---|---|---|---|---|
| **Pressure** | 150 mT | 150 mT | 150 mT | 150 mT | 0 mT | 0 mT |
| **RF Bottom** | 0 W | 350 W | 250 W | 250 W | 0 W | 0 W |
| **Gap** | 3 cm | 3 cm | 3 cm | 3 cm | 5.3 cm | 5.3 cm |
| **$N_2$** | 20 sccm | 20 sccm | 10 sccm | 10 sccm | 50 sccm | 50 sccm |
| **$BCl_3$** | 100 sccm | 100 sccm | 97 sccm | 97 sccm | 0 sccm | 0 sccm |
| **$Cl_2$** | 10 sccm | 10 sccm | 33 sccm | 33 sccm | 0 sccm | 0 sccm |
| **$CHCl_3$** | 0 sccm | 0 sccm | 0 sccm | 0 sccm | 0 sccm | 0 sccm |
| **Type** | Stabilize | Time | Time | Over Etch | Time | End |
| **Time** | 60 s | 28 s | 8 s | 5% | 15 s | |

**Table IV.4: 0.40 NA surface relief etch recipe**

Designed experiments were performed for step 2 in order to get a recipe with ideal pattern transfer characteristics. The final recipe's step 2 is rich in $BCl_3$ to allow the etch to go through the BARC and begin to slowly etch the $Al_2O_3$ without removing material quickly. The power is higher in step 2 to get more DC bias between electrodes and give the ions more energy to break through the native oxide. Step 3 then has slightly more $Cl_2$ to chemically etch the Al and give the desired profile. Profiles from cross-sectioned Al-coated Si test pieces are shown in Figure IV.9 and Figure IV.10. These samples had the desired etch depth, $h$=30 nm, however the process did not have good repeatability due to differences between Si and fused silica pieces. For the fused silica pieces, the step 2 etch time was bracketed from 28 to 31 seconds to accommodate this variation and differences in the process conditions between the Si and fused silica chips.

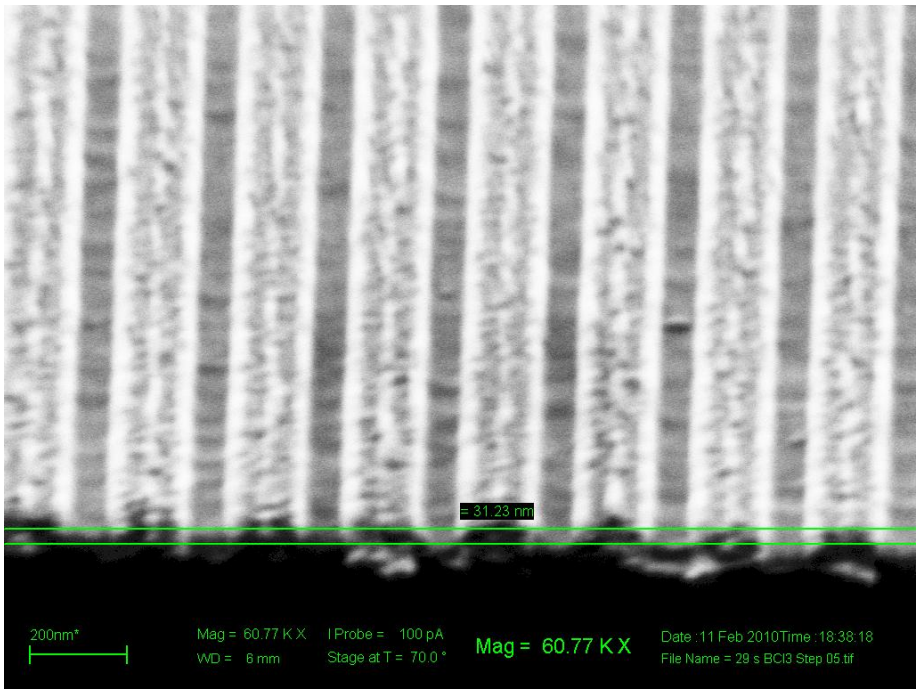


**Figure IV.9: Results from 29 s (step 2) Al etch detailed in Table IV.4. Sample is held at 70°, measured etch depth (*h*) is 33 nm.**

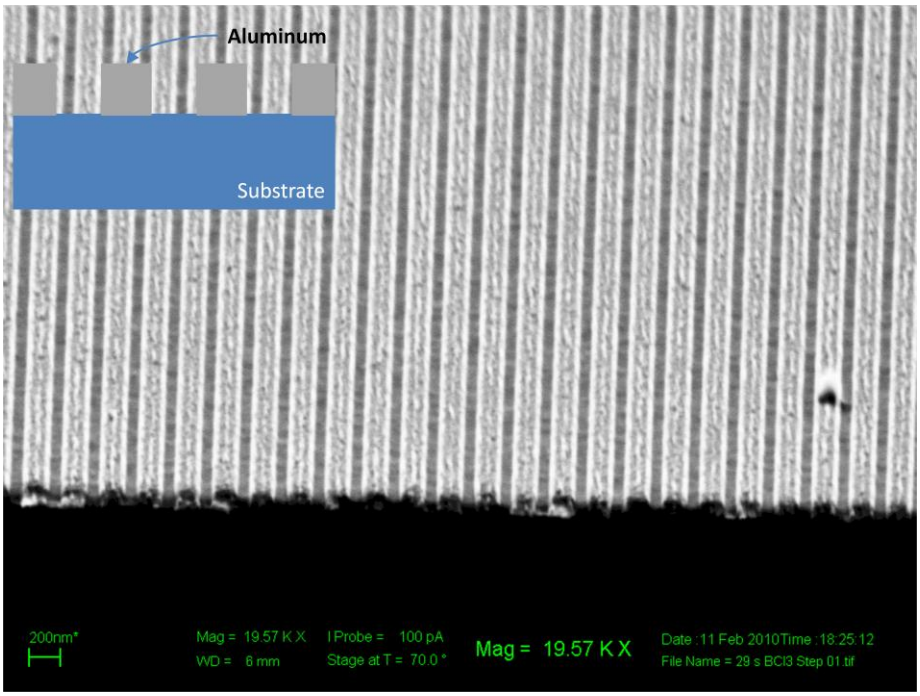


**Figure IV.10: Different view of Figure IV.9 displaying edge profiles. Resist and BARC has been stripped in $O_2$ plasma.**

The recipe used for transferring the 0.20 NA patterns is shown in Table IV.5.

| Parameter | Step 1 | Step 2 | Step 3 | Step 4 | Step 5 | Step 6 |
|---|---|---|---|---|---|---|
| **Pressure** | 150 mT | 150 mT | 150 mT | 0 mT | 0 mT | 0 mT |
| **RF Bottom** | 0 W | 1000 W | 100 W | 0 W | 0 W | 0 W |
| **Gap** | 3 cm | 3 cm | 3 cm | 3 cm | 5.3 cm | 5.3 cm |
| **$N_2$** | 20 sccm | 20 sccm | 40 sccm | 50 sccm | 50 sccm | 50 sccm |
| **$BCl_3$** | 100 sccm | 100 sccm | 50 sccm | 0 sccm | 0 sccm | 0 sccm |
| **$Cl_2$** | 60 sccm | 60 sccm | 60 sccm | 0 sccm | 0 sccm | 0 sccm |
| **$CHCl_3$** | 0 sccm | 0 sccm | 0 sccm | 0 sccm | 0 sccm | 0 sccm |
| **Type** | Stabilize | Time | Time | Time | Time | End |
| **Time** | 60 s | 10 s | 2 s | 1 s | 15 s | |

**Table IV.5: 0.20 NA transmitting feature etch recipe.**

This etch recipe is designed to allow the larger exposed Al spaces to clear rapidly. A high power is used to penetrate the BARC and native oxide quickly, and more $Cl_2$ is used in step 2 for quick etching once the oxide is removed. Step 3 is short and at low power, with a high relative amount of $Cl_2$ to assist in removal of stringers left over between etched lines. Final etched cross-section images are shown in Figure IV.11 Figure IV.12. Although the patterns have transferred to the Al and the remaining Al has the original thickness, the lines have a higher surface roughness and scalloped edges. This is an artifact of the RF sputter deposition and likely worsened by the Trion RIE tool available for $O_2$ plasma stripping. A SEM micrograph of an unpatterned sample deposited in the same run as the etched sample is shown in Figure IV.13 and has similar surface roughness. This surface roughness and its impact on etch quality was not detected until fabrication was nearly complete and all imaging steps were complete. Alternative films deposited via thermal evaporation had lower surface roughness and etched easier, however the thermal evaporation tool could not accommodate small pieces such as the fused silica used here.

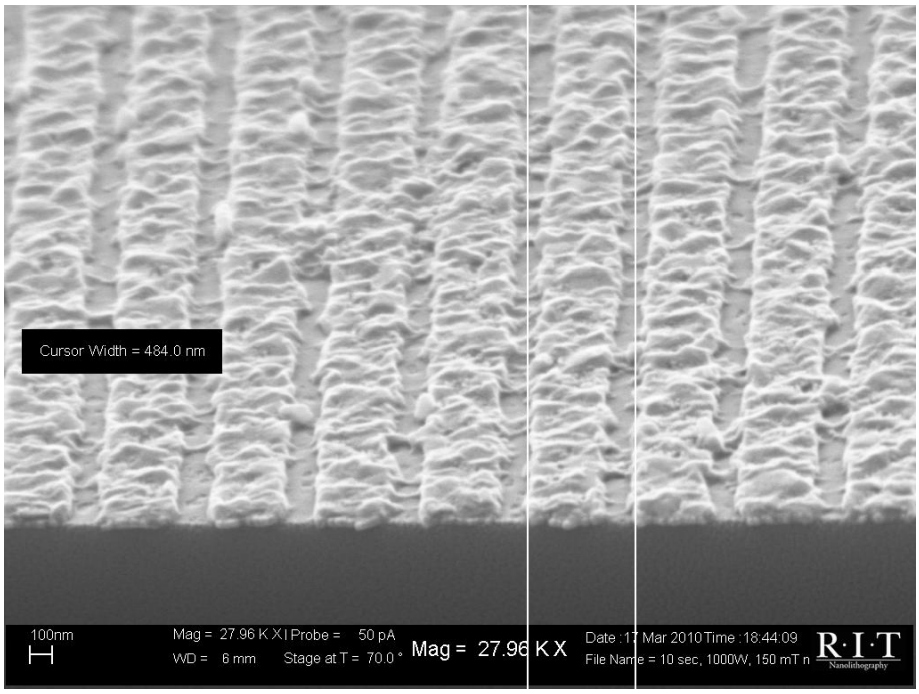


**Figure IV.11: Al etch using the process described in Table IV.5. Substrate is fused silica. Resist and BARC have been stripped.**

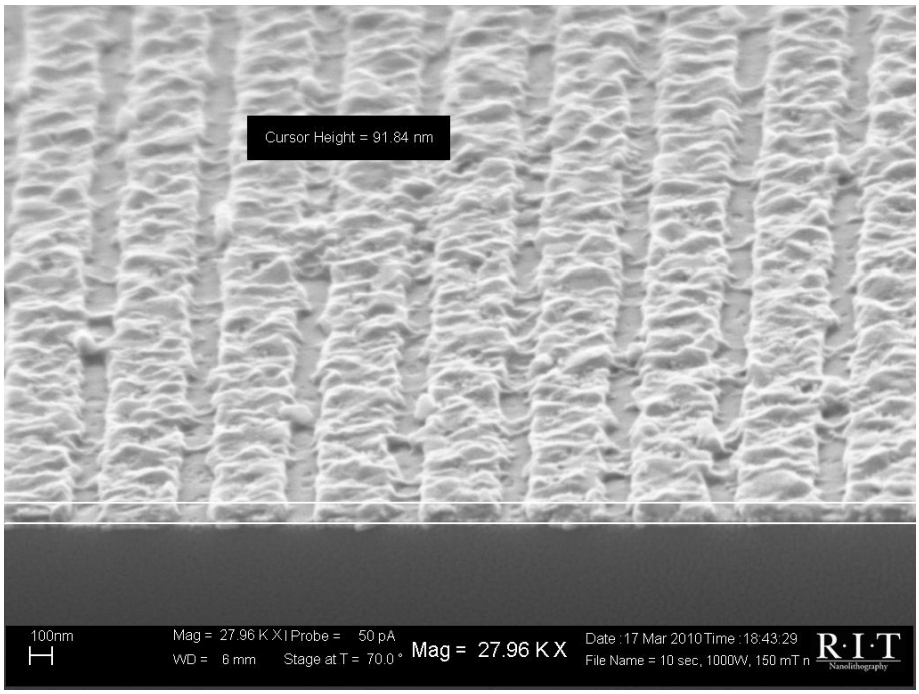


**Figure IV.12: Film thickness measurement on etched Al. The aluminum is noticeably rough due to the RF sputtering process used. This is representative of the reference devices, which do not have EWAF grooves.**

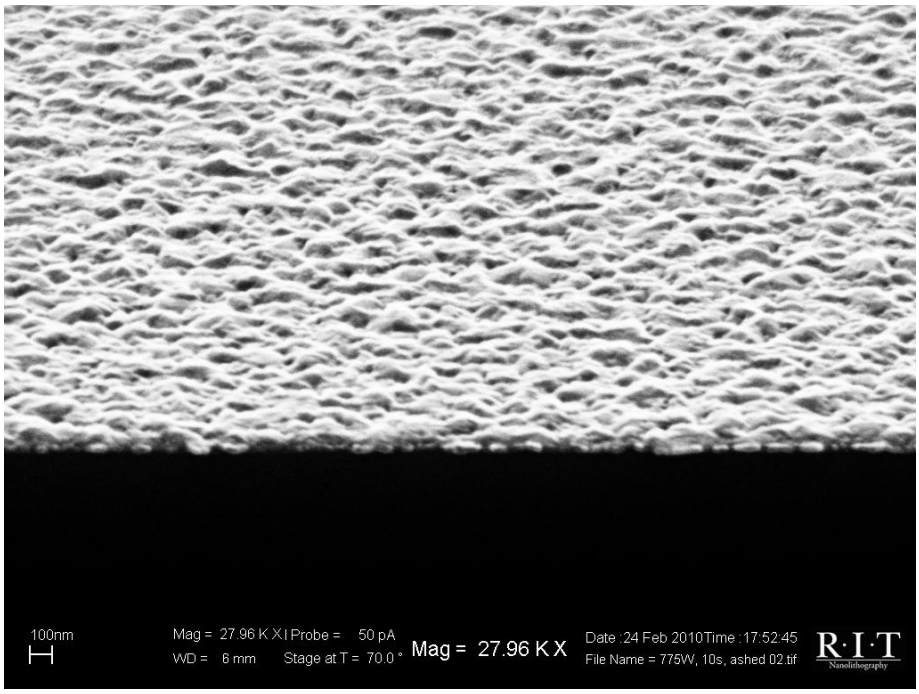


**Figure IV.13: Al from PE4410 sputter tool. Surface roughness has a similar character to that in Figure IV.12.**

### D. Fabricated Devices

The process flow presented in section A was used for fabrication and several test devices were completed. In addition to a reference device, etch time brackets of the 1st RIE step were done in order to accommodate small changes in the etch process as well as provide an opportunity for looking at alignment changes. To minimize variation in these samples, all deposition, cleaning, lithography, and etch steps were performed at the same time over the sample set when possible, and using identical recipes in rapid sequence when not. Figure IV.14 shows a completed EWAF structure. The Al transmission grating is visible and the small linewidth variations due to deposition quality are visible. Also visible is the 1st etch, which has defined the grooves. Angular alignment on this particular sample is good, consistent across the field of view. Etch depth of the EWAF structures is estimated at approximately 30 nm as it was in the etch test samples. SEM micrograph

quality is also slightly lower in Figure IV.14 because the sample was not over-coated with a usual gold layer.

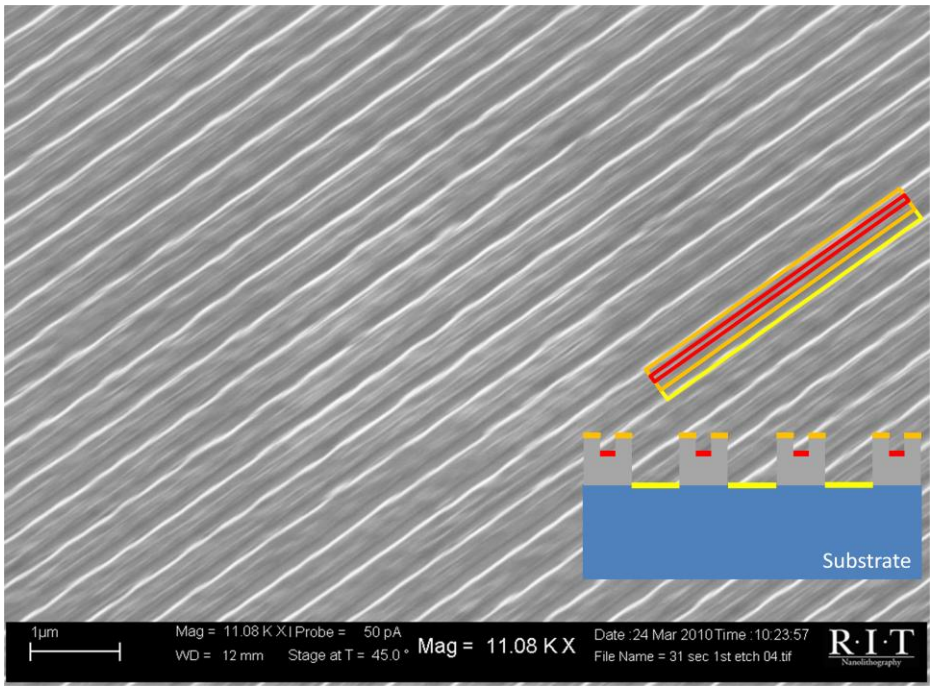


**Figure IV.14: Completed device using a 31 s 1st etch. Note the EWAF groove visible in the center of the Al absorber.**

### E. Testing

The completed EWAF structure was tested along with a reference device using a Woollam VASE in scatterometer mode, as described in Section B. Using this particular mode of operation, the source polarization and wavelength are selectable, as are the angle of incidence of the source on the sample, and the collection angle of the detector. By sweeping the detector over a cone of angles, intensity of the diffracted orders can be verified. Based on the angular position of the diffracted orders, fabrication controls can be verified. The structures were designed for measurement at $\lambda$=248 nm, where the ellipsometer has sufficient intensity for transmission measurements. The ellipsometer features a readily adjustable, accurate monochromator for wavelength selection and the

ability to select TM polarized light. The VASE allows measurements of all diffracted orders by sweeping either the sample or detector to record intensity. The goniometers are accurate to within 0.002°, enabling pitch measurement to within ±0.03 nm [93]. Finally, the measurements are taken using the diffraction orders and in the far field, directly verifying the EWAFs ability to change the aerial image.

Measurements at normal incidence and TM polarization of the EWAF and reference samples are shown in Figure IV.15. In this measurement, the sample and detector are both at 0° while the wavelength is swept. Rotational alignment of the sample is performed by monitoring the signal intensity of an unpolarized 248 nm beam with the detector at the calculated $1^{st}$ order diffraction angle, $\theta$=30.82°. This ensures that the polarization has the intended orientation with respect to plane-of-incidence and the grating lines. A reference scan is also performed before measurement to correct for the intrinsic emission spectra of the lamp. In addition, the noise from the measurement at each wavelength was less than 10% of the signal

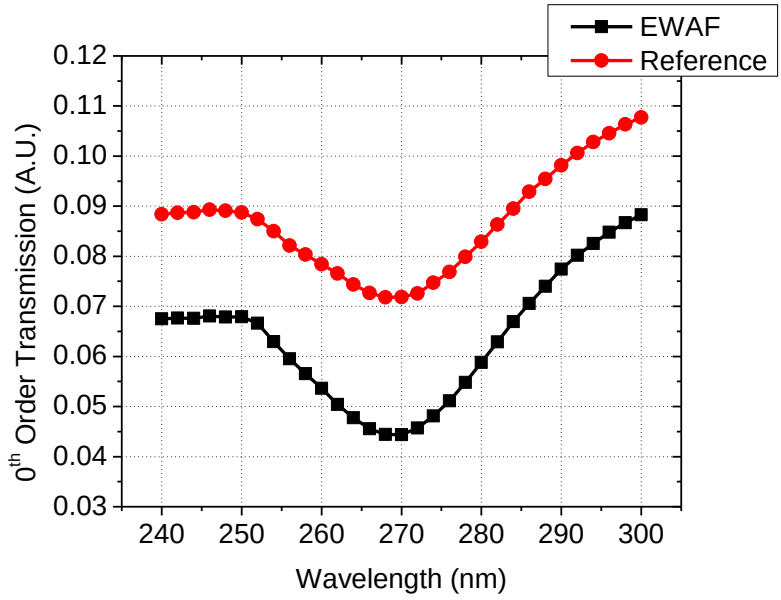


**Figure IV.15: Normal incidence measurements of EWAF and reference samples.**

The sample with EWAFs has a lower zero order transmission than the reference Al transmission grating throughout the measured spectrum. Converting the intensity measurements to electric field magnitudes as simulated indicates that this sample has a zero order enhancement factor of 0.87 at $\lambda$=248 nm. In addition, this sample has a characteristic dip in transmission intensity that represents surface plasmon resonance at 270 nm.

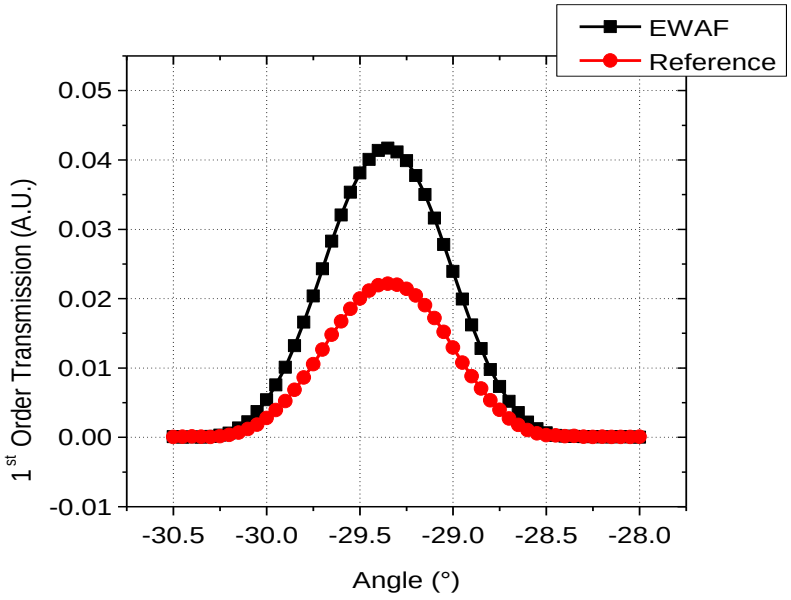


**Figure IV.16: Normal incidence 1st order transmission measured at $\lambda$=248 nm. The detector is swept from -28° to -30.5°.**

The 1st order intensity is measured at normal incidence, with wavelength set to $\lambda$=248 nm. The peak intensity for the 1st order of both the reference and EWAF samples is 29.35° as shown in Figure IV.16. This corresponds to an electric field magnitude enhancement factor of 1.37. Both samples were fabricated to have an intended pitch of 484 nm, which was verified on a SEM. The pitch of the gratings can be checked more accurately by optical measurement. Using Equation (2.21), the grating pitch can be calculated from the 1st order angle. For these samples, the pitch was $p$=506 nm, a difference of 22 nm. The intensity dip in Figure IV.15 can also be further analyzed using the SPP propagation constant, $\beta$ [29].

$$\beta = m\frac{2\pi}{p} \tag{4.2}$$

Using the pitch as measured above, the propagation constant of the grating is 2.4836e7 $m^{-1}$. The propagation constant for an ideal Al grating, calculated by the SPP dispersion

relation Equation (2.51) is 2.445e7 $m^{-1}$. This small difference in the propagation constant is most likely due to naturally forming $Al_2O_3$ on the Al absorber. Using an Effective Medium Approximation (EMA) material composed of 89% Al and 11% $Al_2O_3$ gives a match for the propagation constant [94]. This small amount of aluminum oxide generally agrees with results from samples measured by other researchers via XPS depth profiling, as any exposed Al will readily oxidize when exposed to oxygen [95].

The enhancement factors for $0^{th}$ and $1^{st}$ orders are slightly different from those predicted by simulation in the previous chapter. The simulation indicates enhancement factors should be 0.67 and 1.23 for the $0^{th}$ and $1^{st}$ orders at $p$=484 nm. At the actual 506 nm pitch of the fabricated grating, the enhancement factors should be 0.76 and 1.26 for the $0^{th}$ and $1^{st}$ orders, respectively. As measured via scatterometry, the enhancement factors are 0.87 and 1.37 for $0^{th}$ and $1^{st}$ order. The upward shift in both of these values can be explained by considering the alignment of the two layers and the influences of EWAF profile. Further analysis of Figure IV.14 using offline measurement software indicates that although the layers are aligned well angularly, there is an approximate 19 nm misalignment in the lateral direction [96]. These measurements and a detailed inlay are included in Figure IV.17.

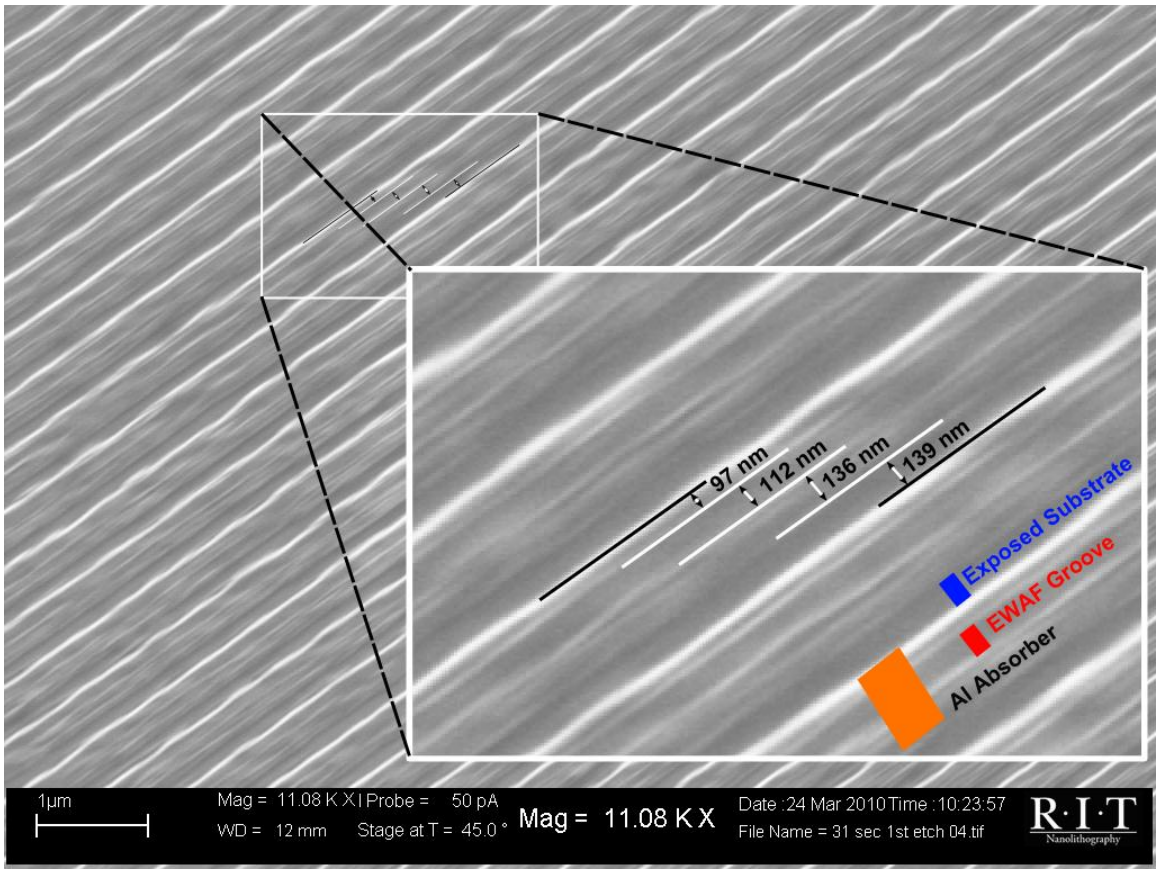


**Figure IV.17: SEM measurement with inlay showing detailed measurements of EWAF groove in relation to transmitting features.**

Scaling for the discrepancy between SEM and ellipsometer, the alignment offset is ≈20 nm. Both the EWAFs and transmitting features are sized differently from simulation. EWAFs are approximately 12 nm smaller, while the transmitting slots are approximately 41 nm smaller. These differences are the result of small dose differences between the test pieces used for dose calibration, as well as etch process differences between the silicon test pieces used for etch recipe setup and the silica pieces. The 41 nm main feature CD shift is not critical, since the enhancement factors are determined by comparing to a reference sample exposed and etched under the same conditions. In other words, the transmitting slots being compared have the same CD.

Using a Fourier cosine series to represent the bottom surface corrugation, *f(x)* in this case, the effect of misalignments and groove profile can be quantified. Since the grooves are an even function, the square profile can be decomposed into cosinusoidal components by [97]:

$$a_n = \frac{2}{l}\int_0^l f(x)\cos\frac{n\pi x}{l}dx \tag{4.3}$$

$$f(x) = \frac{a_0}{2} + \sum_{n=1}^{\infty}\left(a_n \cos\frac{n\pi x}{l}\right) \tag{4.4}$$

In Equations (4.3) and (4.4), *f(x)* represents the original bottom surface profile and l represents half the period of the function *f(x)*, centered about $x$=0. By retaining various terms of the Fourier series, the groove's profile can be studied as it changes from sinusoidal to square. Figure IV.18 shows a 506 nm pitch main pattern with a bottom-surface corrugation with a 253 nm period, similar to the fabricated EWAF structures. The curves plotted are the $0^{th}$ term, $0^{th}$ + $1^{st}$ term, $0^{th}$, $1^{st}$, and $3^{rd}$, and $0^{th}$ through $25^{th}$ terms. By the time 25 terms are included in the series, the profile has a recognizable square profile.

In Figure IV.19 and Figure IV.20, these four decompositions of the square groove are used to investigate the effects of layer misalignment and bottom-surface profile on diffracted order enhancement factor. In Figure IV.19a, the enhancement factors follow an approximately sinusoidal relationship as inter-layer alignment is changed. In Figure IV.19b, the sine profile begins to degrade as the groove starts to resemble more of a square shape. These distortions continue as more terms are added to the Fourier series. Figure IV.20d shows the 25 term series, which is almost square in profile. The sinusoidal

shape of the diffracted order enhancement profiles is distorted in this case, but for the $0^{th}$ order the trend is still visible. As the profile becomes square, the enhancement factors also grow in magnitude as higher harmonics are added. The lowest enhancement factors are at the n=1 series and the magnitude of the enhancement and suppression steadily grows as more harmonics are added. In Figure IV.20d, the point on the curves in which the enhancement factors most closely correspond to measured data is marked. At this -20 nm layer offset, the order enhancement is 0.85 and 1.33 for the $0^{th}$ and $+1^{st}$ orders, respectively. This agrees with measurements from the Woollam ellipsometer within 2.3% error for the $0^{th}$ order and 2.9% error for the $1^{st}$ order. These discrepancies can likely be resolved by using a full square wave bottom-surface corrugation in simulation.

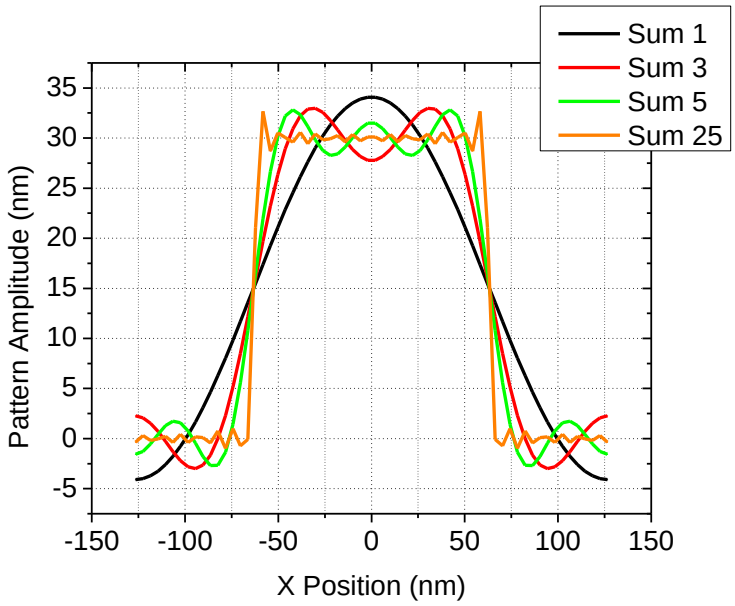


**Figure IV.18: Fourier series representation of bottom-surface EWAFs. Zero through 25 terms are shown.**

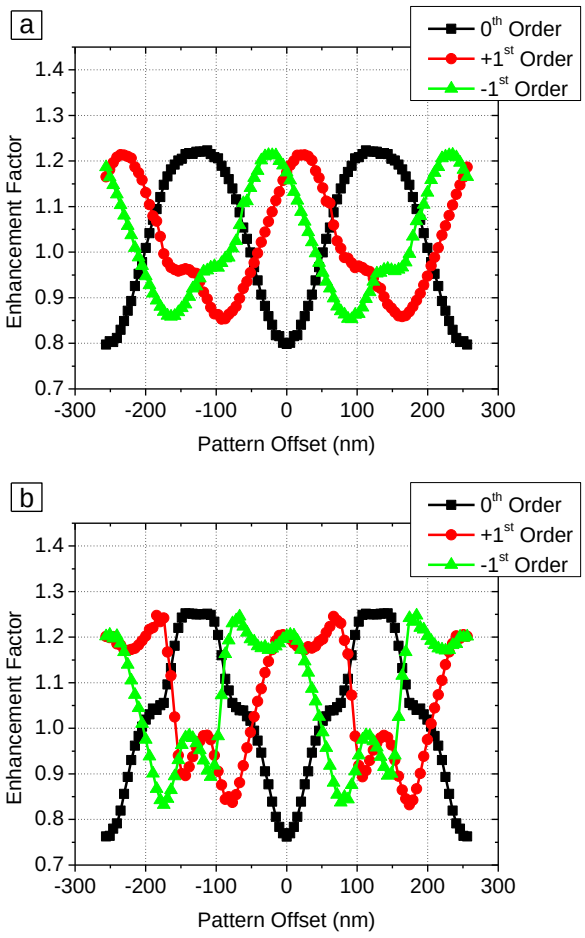


**Figure IV.19: 506 nm pitch pattern with bottom corrugation of the (a) fundamental sinusoidal harmonic and (b) including terms 0, 1 and 3 of the fourier cosine series. The corrugations are laterally offset from the main pattern by the distance indicated.**

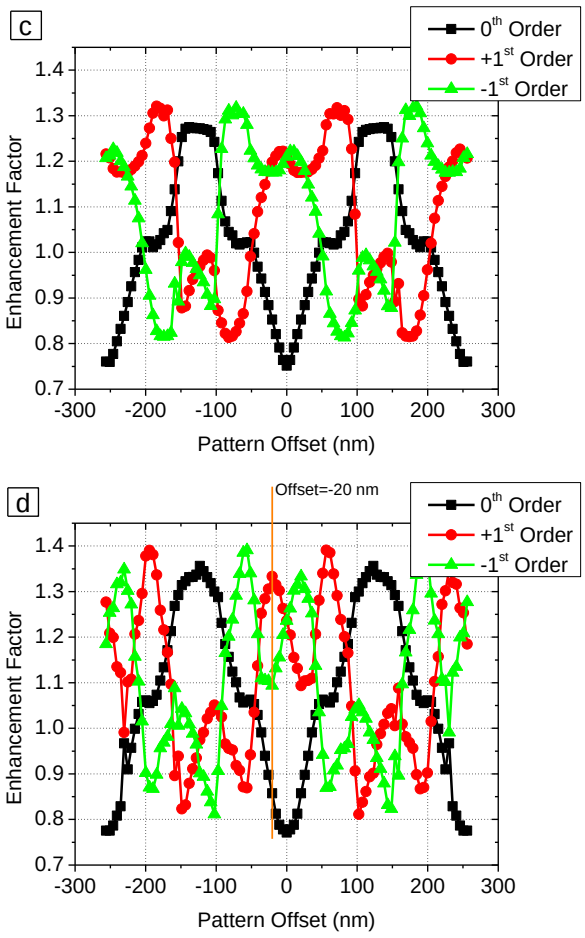


**Figure IV.20: 506 nm pitch pattern with bottom corrugation of the (c) 0, 1, 3, and 5 terms of the fourier cosine series and (d) terms 0, through 25 of the fourier cosine series. The corrugations are laterally offset from the main pattern by the distance indicated.**

The alignment offsets between simulation and measured micrographs agree, especially when the SEM measurements are scaled to the pitch as measured by ellipsometer.

In this section, the process flow and techniques used for fabricating an EWAF reticle were presented. Detailed descriptions of wafer dicing, cleaning steps, lithography, and RIE were presented, along with process recipes. The measured results of fabricating a test EWAF sample and reference sample were presented, and compared back to simulations preformed in Chapter III. Interference lithography on a custom-built tool was

used to fabricate the two-image layer test pieces. Samples were characterized using a VASE in scatterometry mode. This allowed both the range of illumination wavelength and detection angle to be varied, providing spectroscopic measurements of the $0^{th}$ order and through angle measurements of $1^{st}$ order at $\lambda$=248 nm. The fabricated samples were found to have enhancement factors of 0.87 and 1.37 for $0^{th}$ and $1^{st}$ diffraction orders, respectively. This is in contrast to simulated ideal enhancement factors of 0.67 and 1.26 at the same conditions. By further analyzing the angle of the $1^{st}$ diffraction order, the grating pitch was determined to be $p$=506 nm, a 22 nm difference from design. A 19 nm inter-layer lateral alignment offset was also detected during SEM measurement. Accounting for this measured offset and pitch deviation yields enhancement factors for the fabricated EWAF samples that agree with simulation to within approximately 3%. In summary, EWAF devices that agree with simulation were fabricated, further validating the models and findings discussed in Chapter III.

# V. CONCLUSION

In this thesis, the concept of evanescent wave assist features has been developed, explored, and presented. Continuous scaling of devices in order to keep pace with Moore's law forces lithography to become increasingly innovative. The ITRS roadmap indicates that until the 32 nm technology node, there will be no planned wavelength shrinks or next generation immersion fluids. Since it is unlikely that EUV lithography will be ready for introduction at 32 nm, it has larger a probability for introduction at 22 nm or 16 nm nodes [12]. Optical lithography, therefore, will have to meet increasingly challenging needs until at least 2017 at the earliest. In order to push resolution limits for further scaling in the absence of near-term wavelength shrinks, alternative mask materials, layouts, and illumination shaping are used. These are commonly grouped together and referred to as RET. These techniques include Alternative Phase Shift Masking, Attenuated Phase Shift Masking, Chromeless Phase Shift Masking, illumination optimization such as off-axis illumination and partial coherence, as well as others. Using partially coherent light for illumination is common practice and extends the resolution limit for a given system by spreading diffraction orders across the pupil. A downside of this extended resolution is a drop in image contrast due to incomplete diffracted order collection. EWAFs are one way to increase a feature's image contrast and NILS by including local, buried, opaque features in a layout. This increase in contrast counteracts the loss of modulation due to illumination compromises that may need to be made for global best imaging on a full-chip layout. This type of ultimate image

enhancement technique will prove useful as lithography scales to its ultimate limits near the 16 nm node, where every optimization available will be important.

EWAFs operate in the near-field region, converting these fields to propagating components that affect aerial image quality. An introduction and study of key work is presented in Chapter II. Several key papers on anomalous transmission introduce the role of near-fields in observed transmission in the far-field. Corrugations and holes were demonstrated as a means to convert between evanescent and propagating components. Surface Plasmon Polaritons were introduced as a special means of amplifying normal field components by coupling the electric field to charge oscillations of a conductor's electron cloud. Finally, studies were presented where corrugations on opposite sides of a surface couple energy to each other.

EWAFS were further defined in Chapter III, along with numerical investigative techniques used to understand their operation. The FDTD routine is introduced in the scope of these simulations, and the projection simulator and thin-film stack modules are introduced. Enhancement Factor is presented as a metric for quantifying changes in diffracted orders caused by addition of EWAFs to a design. Image contrast and NILS are also defined for aerial images projected into photoresist. EWAFs applied to both 2-D and 1-D designs are studied. In the case of contacts, these top-surface EWAFs etched into the mask substrate caused an unpolarized illumination contrast gain of 27% over a binary mask. Further study using 1-D features was used to investigate the physics of the observed enhancement. Using these layouts, image contrast and NILS enhancements of over 2X were observed for highly optimized imaging conditions. More typical illumination resulted in an 18% and 15% improvement in image contrast and NILS,

respectively. The mask was then simulated and compared to an identical case using APSM. While APSM has slightly higher values for image contrast and NILS improvement, both APSM and EWAF deliver similar results using different principles. All experiments suggest the method of operation for EWAFs involves grating coupling of supported orders from transmitting mask features to the milled EWAFs in the absorber or mask substrate. Further, SPP resonance is an important part of their operation because TM polarized light creates a field enhancement of normal components to the mask surface, even off-resonance. This field amplification enables the coupled, frustrated fields to have more energy and affect final intensities of transmitted orders.

This work is significant in that it is the first study where corrugations and slot arrays have been applied to projection lithography applications. Further, while most studies to date have concentrated on silver or gold metals and wavelengths ranging from UV to near IR, this work has demonstrated that aluminum can support resonance at DUV (248 nm and 193 nm) wavelengths. Studies to date have focused on combinations of isolated sub-wavelength holes in proximity to each other, single holes or slits surrounded by many periodic corrugations, and top and bottom surface reflection gratings on either side of an absorbing material. This work is the first study of periodic transmitting features in conjunction with periodic so-called EWAF grooves that are non-transmitting. Another unique aspect of this work is that in all cases studied, including the fabrication test vehicle, the transmitting features and EWAF corrugations were never significantly sub-wavelength. In fact, the simulated transmitting slot CD was $0.73\lambda$ and the EWAF width was $0.5\lambda$. Typical feature sizes are usually closer to $0.1\lambda$ to be considered sub-wavelength. The features providing all enhancement effects discussed in this work are

close to wavelength sized. Finally, this work discusses novel applications of SPPs to photomask applications in the scope of projection lithography. In this context, the SPPs serve to modulate existing diffracted orders, instead of providing fundamentally increased resolution. These orders, which have been modified through interactions with near-fields, are then introduced to an optical reduction system. The use of near-field features in combination with far-field imaging tools like projection optics is also novel in the scope of projection lithography.

In order to validate the numerical investigation, a sample EWAF layout was fabricated at RIT SMFL using interference lithography. An interferometer was modified for low-NA operation, and pitch and CD information were calibrated using scanning electron microscopy. The fabricated test piece, compared to an identical reference piece, demonstrated diffracted order enhancement factors of 0.87 and 1.37 for $0^{th}$ and $1^{st}$ orders, respectively. While these features are slightly different from simulated enhancement factors, the differences can be explained by considering an SEM measured approximately 19 nm alignment offset between layers. When scaled to pitch as measured via ellipsometer, the alignment offset agrees with enhancement factors simulated for misaligned lithography layers. The agreement of numerical methods and fabricated samples lends credibility to the simulations. The impact of the shape of the bottom layer on enhancement factor was also studied using a Fourier series decomposition of the bottom groove. The enhancement factors in general have a sinusoidal profile that varies with misalignment, however higher harmonics contribute extra features to the enhancement curves of both $0^{th}$ and $1^{st}$ orders. Using a 25 term Fourier series approximation to the square profile of the EWAFs, diffracted order enhancement factors

for both $0^{th}$ and $1^{st}$ orders agree with measured values within 2.9% at a 20 nm simulated alignment offset.

In summary, when simulated in the context of a projection lithography system, reticles containing EWAFs have demonstrated an over 2X improvement in contrast and NILS under highly optimized conditions which place imaging orders at the extreme edges of the lens pupil. More typical conditions yield contrast and NILS improvements of 18% and 15%, respectively. While these numbers compare favorably with attenuated phase shift masking, they represent the important milestone of the demonstration of wavefront engineering in the near-field and its subsequent use to affect a useful change in a lithographic far-field aerial image.

# VI. APPENDIX A: ENERGY FLOW AT TIR ACROSS INTERFACES

It can be rigorously shown that the evanescent field will not carry energy across a boundary by taking the time-average energy flow, given by the Poynting vector. This is defined as:

$$\vec{S} = \frac{c}{4\pi}\left(\vec{E} \times \vec{H}\right) \tag{6.1}$$

From this point, we will closely follow the proof presented in Born & Wolf [98]. The electric and magnetic fields, transmitted across the boundary are given as:

$$\begin{aligned} E_{tx} &= -T_{\|} \cos\theta_t e^{-i\tau_t} \\ E_{ty} &= T_{\perp} e^{-i\tau_t} \\ E_{tz} &= T_{\|} \sin\theta_t e^{-i\tau_t} \end{aligned} \tag{6.2}$$

$$\begin{aligned} H_{tx} &= -T_{\perp} \cos\theta_t \sqrt{\varepsilon_2} e^{-i\tau_t} \\ H_{ty} &= -T_{\|} \sqrt{\varepsilon_2} e^{-i\tau_t} \\ H_{tz} &= T_{\perp} \sin\theta_t \sqrt{\varepsilon_2} e^{-i\tau_t} \end{aligned} \tag{6.3}$$

In Equations (6.2) and (6.3), $T_{\|}$ and $T_{\perp}$ indicate the complex amplitudes of the transmitted fields. The *x*, *y*, and *z* subscripts for each field component refer to the right-handed coordinate system shown in Figure VI.1. Equation (6.1) can be manipulated to give the *z* component of the Poynting vector, the flow of power across the material interface.

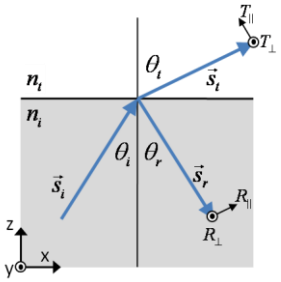


**Figure VI.1: Poynting vectors and complex amplitudes, *R* and *T*.**

$$S_{tz} = \frac{c}{4\pi}\left(E_{tx}H_{ty} - E_{ty}H_{tx}\right) \tag{6.4}$$

Since the energy flow is a real quantity, the complex amplitudes must converted to real values. The *E* and *H* fields become:

$$E_{tx} = \frac{-1}{2}\left(T_{\parallel}\cos\theta_t e^{-i\tau_t} + T_{\parallel}^{*}\cos^{*}\theta_t e^{+i\tau_t}\right)$$

$$E_{tx} = \frac{-1}{2}\left(T_{\parallel}\left(i\sqrt{\frac{\sin^2\theta_i}{\left(\frac{n_t}{n_i}\right)^2} - 1}\right)e^{-i\tau_t} + T_{\parallel}^{*}\left(-i\sqrt{\frac{\sin^2\theta_i}{\left(\frac{n_t}{n_i}\right)^2} - 1}\right)\theta_t e^{+i\tau_t}\right) \tag{6.5}$$

$$E_{tx} = \frac{-i}{2}\sqrt{\frac{\sin^2\theta_i}{\left(\frac{n_t}{n_i}\right)^2} - 1}\left(T_{\parallel}e^{-i\tau_t} - T_{\parallel}^{*}\theta_t e^{+i\tau_t}\right)$$

$$H_{ty} = \frac{-1}{2}\left(T_{\parallel}\sqrt{\varepsilon_2}e^{-i\tau_t} + T_{\parallel}^{*}\sqrt{\varepsilon_2}e^{+i\tau_t}\right)$$

$$H_{ty} = \frac{-1}{2}\sqrt{\varepsilon_2}\left(T_{\parallel}e^{-i\tau_t} + T_{\parallel}^{*}e^{+i\tau_t}\right) \tag{6.6}$$

The product of (6.5) and (6.6) becomes:

$$E_{tx}H_{ty} = \frac{i}{4}\sqrt{\frac{\sin^2\theta_i}{\left(\frac{n_t}{n_i}\right)^2} - 1}\sqrt{\varepsilon_2}\left(T_{\parallel}e^{-i\tau_t} - T_{\parallel}^{*}e^{+i\tau_t}\right)\left(T_{\parallel}e^{-i\tau_t} + T_{\parallel}^{*}e^{+i\tau_t}\right)$$

$$E_{tx}H_{ty} = \frac{i}{4}\sqrt{\frac{\sin^2\theta_i}{\left(\frac{n_t}{n_i}\right)^2} - 1}\sqrt{\varepsilon_2}\left(T_{\parallel}^{2}e^{-2i\tau_t} - T_{\parallel}^{*2}e^{+2i\tau_t}\right) \tag{6.7}$$

Integrating (6.7) and averaging over time yields:

$$\frac{1}{2t'}\int_{-t'}^{t'} E_{tx}H_{ty}dt = \frac{1}{2t'}\int_{-t'}^{t'}\left(T_{\parallel}^{2}e^{-2i\tau_t} - T_{\parallel}^{*2}e^{+2i\tau_t}\right)dt$$

$$\frac{1}{2t'}\int_{-t'}^{t'} E_{tx}H_{ty}dt = \frac{1}{2t'}\int_{-t'}^{t'}\left(T_{\parallel}^{2}e^{-2i\omega t}\exp\left[+2i\frac{\omega x\sin\theta_i}{\frac{n_t}{n_i}v_2}\right] - T_{\parallel}^{*2}e^{+2i\omega t}\exp\left[-2i\frac{\omega x\sin\theta_i}{\frac{n_t}{n_i}v_2}\right]\right)dt$$

$$\frac{1}{2t'}\int_{-t'}^{t'} E_{tx}H_{ty}dt = \frac{1}{2t'}\left[T_{\parallel}^{2}\exp\left[+2i\frac{\omega x\sin\theta_i}{\frac{n_t}{n_i}v_2}\right]\int_{-t'}^{t'}e^{-2i\omega t}dt - T_{\parallel}^{*2}\exp\left[-2i\frac{\omega x\sin\theta_i}{\frac{n_t}{n_i}v_2}\right]\int_{-t'}^{t'}e^{+2i\omega t}dt\right]$$

$$\frac{1}{2t'}\int_{-t'}^{t'} E_{tx}H_{ty}dt = \frac{1}{2t'}\left[T_{\parallel}^{2}\exp\left[+2i\frac{\omega x\sin\theta_i}{\frac{n_t}{n_i}v_2}\right]\left.\frac{e^{-2i\omega t}}{-2i\omega}\right|_{-t'}^{t'} - T_{\parallel}^{*2}\exp\left[-2i\frac{\omega x\sin\theta_i}{\frac{n_t}{n_i}v_2}\right]\left.\frac{e^{+2i\omega t}}{2i\omega}\right|_{-t'}^{t'}\right]$$

$$\frac{1}{2t'}\int_{-t'}^{t'} E_{tx}H_{ty}dt = \frac{1}{2t'}\left[T_{\parallel}^{2}\exp\left[+2i\frac{\omega x\sin\theta_i}{\frac{n_t}{n_i}v_2}\right]\left(\frac{e^{+2i\omega t'} - e^{-2i\omega t'}}{2i\omega}\right) - T_{\parallel}^{*2}\exp\left[-2i\frac{\omega x\sin\theta_i}{\frac{n_t}{n_i}v_2}\right]\left(\frac{e^{+2i\omega t'} - e^{-2i\omega t'}}{2i\omega}\right)\right] \tag{6.8}$$

$$= \frac{1}{2t'}\left[ T_{\parallel}^{2} \exp\left[ +2i \frac{\omega x \sin\theta_i}{\frac{n_t}{n_i} v_2} \right] \left( \frac{\sin(2\omega t')}{\omega} \right) - T_{\parallel}^{*2} \exp\left[ -2i \frac{\omega x \sin\theta_i}{\frac{n_t}{n_i} v_2} \right] \left( \frac{\sin(2\omega t')}{\omega} \right) \right]$$

$$= \left[ T_{\parallel}^{2} \exp\left[ +2i \frac{\omega x \sin\theta_i}{\frac{n_t}{n_i} v_2} \right] - T_{\parallel}^{*2} \exp\left[ -2i \frac{\omega x \sin\theta_i}{\frac{n_t}{n_i} v_2} \right] \right] \frac{1}{2t'} \frac{\sin(2\omega t')}{\omega}$$

Finally, substituting for the temporal period, $T = 2\pi/\omega$, the equation can be condensed to:

$$\frac{1}{2t'} \int_{-t'}^{t'} E_{tx} H_{ty} dt = \left[ T_{\parallel}^{2} \exp\left[ +2i \frac{\omega x \sin\theta_i}{\frac{n_t}{n_i} v_2} \right] - T_{\parallel}^{*2} \exp\left[ -2i \frac{\omega x \sin\theta_i}{\frac{n_t}{n_i} v_2} \right] \right] \frac{1}{2t'} \frac{\sin(2\omega t')}{\omega}$$

$$\frac{1}{2t'} \int_{-t'}^{t'} E_{tx} H_{ty} dt = \left[ T_{\parallel}^{2} \exp\left[ +2i \frac{\omega x \sin\theta_i}{\frac{n_t}{n_i} v_2} \right] - T_{\parallel}^{*2} \exp\left[ -2i \frac{\omega x \sin\theta_i}{\frac{n_t}{n_i} v_2} \right] \right] \frac{1}{2t'} \frac{\sin(2\omega t')T}{2\pi} \quad (6.9)$$

$$\frac{1}{2t'} \int_{-t'}^{t'} E_{tx} H_{ty} dt = \left[ T_{\parallel}^{2} \exp\left[ +2i \frac{\omega x \sin\theta_i}{\frac{n_t}{n_i} v_2} \right] - T_{\parallel}^{*2} \exp\left[ -2i \frac{\omega x \sin\theta_i}{\frac{n_t}{n_i} v_2} \right] \right] \frac{\sin(2\omega t')}{4\pi} \frac{T}{t'}$$

Since the integration length was specified to be much larger than *T*, the final term in the equation dominates and drives the result to zero. Since both $E_{ty}$ and $H_{tx}$ have the same form, their result is identical after integration. The *z* component of the Poynting vector therefore is zero, meaning on a time average scale much larger than the period of the wave considered, no energy flows across the interface.

# VII. APPENDIX B: MATLAB SIMULATION ALGORITHM

### A. LSF Script

```
Define sigma settings (dipole)

Set number of simulation source points

Define NA

Define M (magnification)


Load starting layout file

Read n of fused silica (account for refraction in glass)

Calculate illumination angles in glass


For each sampled sigma point:

   select the source

   change the illumination angle to the element in the for
loop

   display a status message

   run the FDTD simulation

   if converged

      exit early


   extract near fields for simulation
```

```
   extract frequency, simulation pitch
   convert near fields into far field data in cylindrical
      coordinates
   store data as Er, Et, and Ey


   save                                lambda,k,NA,illumination
angle,Er,Et,Ey,magnification,and
      simulation pitch data in matlab format
```

### B. MATLAB Script "EWAFSim"

```
Define wafer immersion media
Define film stack indices and thicknesses


Scan an input directory and create a list of mask
simulation
   files


Scan input directory to load files with mask simulation
data (1
   for each angle)


For each input file:


   calculate direction cosine for all diffracted orders
```

```
   account for magnification
   recalculate the angle of diffracted orders at wafer level
   filter diffracted orders based on NA



   apply radiometric correction


   determine direction cosine of each diffraction order in
each
      film


   calculate the transmission & reflection amplitude
coefficients
      via MacLeod's method


   correct for induced spherical aberration in the resist
stack
   Determine x and z components of E field


   Calculate E reflected and impinging from each film
interface
   initialize aerial image domain


   For each z image space coordinate
```

```
     determine what film the z location corresponds to
     set refractive index and direction cosine of orders

     for each x image space coordinate
        calculate the phase of each incident order
        calculate the phase of each reflected order
        sum the complex Ex field plus any accumulated phase
from
           the translation from phase reference point over
all
           imaging orders
        sum the complex Ez field plus any accumulated phase
from
           the translation from phase reference point over
all
           imaging orders
   record the intensity image as squared mag Ex + squared
mag Ez
   pare down the stack to get cross section image only in
resist
   record best focus image cutline

sum the individual coherent resist images to get final
image
```

```
extract best focus cutline


plot results
```

# VIII. REFERENCES


[1] J. Kilby, "Invention of the Integrated Circuit," *IEEE Transaction on Electron Devices*, vol. 23, no. 7, pp. 648-654, Jul. 1967.

[2] P. Van Zant, "The Semiconductor Industry," in *Microchip Fabrication*, 3rd ed., New York: McGraw-Hill, 1997.

[3] G. E. Moore, "Cramming more components onto integrated circuits," *Electronics*, vol. 38, no. 8, pp. 114-117, 1965.

[4] M. Rothschild, "A Roadmap for Optical Lithography," *Optics & Photonics News*, vol. 21, no. 6, pp. 27-31, Jun-2010.

[5] Wikipedia Contributors, "Transistor Count," *Wikipedia, The Free Encyclopedia*, 04-May-2010. [Online]. Available: http://en.wikipedia.org/wiki/Transistor_count. [Accessed: 03-Jun-2010].

[6] K. Ronse, "Optical lithography--a historical perspective," *Comptes Rendus Physique*, vol. 7, no. 8, pp. 844-857, Oct. 2006.

[7] B. W. Smith, "Optics for Photolithography," in *Microlithography: science and technology*, J. R. Sheats and B. W. Smith, Eds. New York: Marcel Dekker, 1998, pp. 171-270.

[8] C. A. Mack, *Fundamental Principles of Optical Lithography: The Science of Microfabrication*. Chichester, West Sussex, England: Wiley, 2007.

[9] J. R. Sheats and B. W. Smith, Eds., *Microlithography: science and technology*. New York: Marcel Dekker, 1998.

[10] R. L. Easton, "Optical Imaging Systems as Filters," in *Linear Mathematics with Applications to Imaging*, vol. 2, 2 vols., Unpublished, 2005.

[11] B. W. Smith, "Resist Processing," in *Microlithography: science and technology*, J. R. Sheats and B. W. Smith, Eds. New York: Marcel Dekker, 1998, pp. 515-565.

[12] ITRS, "International Technology Roadmap for Semiconductors (ITRS) 2009 Edition: Lithography," *2009 Edition ITRS Lithography Roadmap*, 2009. [Online]. Available: http://www.itrs.net/Links/2009ITRS/2009Chapters_2009Tables/2009_Litho.pdf.

[13] B. W. Smith and D. E. Ewbank, "OPC and image optimization using localized frequency analysis," in *Proceedings of SPIE*, vol. 4691, pp. 148-157, 2002.

[14] N. V. Lafferty and B. W. Smith, *Diffracted Order Modulation using a Two-Layer Grating (Unpublished)*. Rochester, NY: Rochester Institute of Technology, 2010, p. 11.

[15] N. V. Lafferty, J. Zhou, and B. W. Smith, "Mask enhancement using an evanescent wave effect," in *Proceedings of SPIE*, vol. 6520, pp. 652041-652041-8, 2007.

[16] S. I. Newton, *Opticks*. New York: Dover, 1979.

[17] F. de Fornel, *Evanescent Waves: From Newtonian Optics to Atomic Optics*, 1st ed. Berlin: Springer, 2001.

[18] E. Hecht, "The Propagation of Light," in *Optics*, 3rd ed., New York: Addison-Wesley, 1998.

[19] M. Born and E. Wolf, "Basic Properties of the Electromagnetic Field," in *Principles of Optics*, 7th ed., Cambridge: Cambridge University Press, 1999.

[20] J. Y. Han, "Multi-Touch Sensing through Frustrated Total Internal Reflection," *FTIR Touch Sensing*, 14-Jun-2010. [Online]. Available: http://cs.nyu.edu/~jhan/ftirsense/index.html. [Accessed: 14-Jun-2010].

[21] M. Lipson, "SEM pictures (top view) of a ring resonator based on the slot waveguide," *Cornell Nanophotonics Group*, 14-Jun-2010. [Online]. Available: http://nanophotonics.ece.cornell.edu/research.html. [Accessed: 14-Jun-2010].

[22] M. W. Kowarz, "Homogeneous and evanescent contributions in scalar near-field diffraction," *Applied Optics*, vol. 34, no. 17, pp. 3055-3063, Jun. 1995.

[23] M. Kowarz, "Diffraction Effects in the Near Field," Ph.D. Thesis, University of Rochester, 1995.

[24] D. Melville and R. Blaikie, "Super-resolution imaging through a planar silver layer," *Optics Express*, vol. 13, no. 6, pp. 2127-2134, Mar. 2005.

[25] E. G. Loewen and E. Popov, *Diffraction gratings and applications*. New York: CRC Press, 1997.

[26] H. Raether, *Surface plasmons on smooth and rough surfaces and on gratings*. Berlin: Springer-Verlag, 1988.

[27] A. Giannattasio, I. R. Hooper, and W. L. Barnes, “Dependence on surface profile in grating-assisted coupling of light to surface plasmon-polaritons,” *Optics Communications*, vol. 261, no. 2, pp. 291-295, May. 2006.

[28] Y. Leviatan, “Electromagnetic coupling between two half-space regions separated by two slot-perforated parallel conducting screens,” *IEEE Transactions on Microwave Theory and Techniques*, vol. 36, no. 1, pp. 44-52, 1988.

[29] S. A. Maier, *Plasmonics: Fundamentals and Applications*, 1st ed. New York: Springer, 2007.

[30] T. Thio, K. M. Pellerin, R. A. Linke, H. J. Lezec, and T. W. Ebbesen, “Enhanced light transmission through a single subwavelength aperture,” *Optics Letters*, vol. 26, no. 24, pp. 1972-1974, Dec. 2001.

[31] A. V. Zayats, I. I. Smolyaninov, and A. A. Maradudin, “Nano-optics of surface plasmon polaritons,” *Physics Reports*, vol. 408, no. 3, pp. 131-314, Mar. 2005.

[32] H. A. Bethe, “Theory of Diffraction by Small Holes,” *Physical Review*, vol. 66, no. 7, p. 163, Oct. 1944.

[33] T. Thio, “A Bright Future for Subwavelength Light Sources,” *American Scientist*, vol. 94, no. 1, pp. 40-47, 2006.

[34] T. W. Ebbesen, H. J. Lezec, H. F. Ghaemi, T. Thio, and P. A. Wolff, “Extraordinary optical transmission through sub-wavelength hole arrays,” *Nature*, vol. 391, no. 6668, pp. 667–669, 1998.

[35] T. J. Kim, T. Thio, T. W. Ebbesen, D. E. Grupp, and H. J. Lezec, “Control of optical transmission through metals perforated with subwavelength hole arrays,” *Optics Letters*, vol. 24, no. 4, pp. 256-258, Feb. 1999.

[36] R. W. Wood, “Anomalous Diffraction Gratings,” *Physical Review*, vol. 48, no. 12, pp. 928-936, Dec. 1935.

[37] A. Hessel and A. A. Oliner, “A New Theory of Wood's Anomalies on Optical Gratings,” *Applied Optics*, vol. 4, no. 10, pp. 1275-1297, Oct. 1965.

[38] H. F. Ghaemi, T. Thio, D. E. Grupp, T. W. Ebbesen, and H. J. Lezec, “Surface plasmons enhance optical transmission through subwavelength holes,” *Physical Review B*, vol. 58, no. 11, p. 6779, 1998.

[39] H. Lezec and T. Thio, “Diffracted evanescent wave model for enhanced and suppressed optical transmission through subwavelength hole arrays,” *Optics Express*, vol. 12, no. 16, pp. 3629-3651, 2004.

[40] G. Gay, O. Alloschery, B. Viaris de Lesegno, C. O 'Dwyer, J. Weiner, and H. J. Lezec, "The optical response of nanostructured surfaces and the composite diffracted evanescent wave model," *Nature Physics*, vol. 2, no. 4, pp. 262-267, Apr. 2006.

[41] F. J. Garcia-Vidal, S. G. Rodrigo, and L. Martin-Moreno, "Foundations of the composite diffracted evanescent wave model," *Nature Physics*, vol. 2, no. 12, p. 790, Dec. 2006.

[42] J. Weiner and H. J. Lezec, "Reply: Foundations of the composite diffracted evanescent wave model," *Nature Physics*, vol. 2, no. 12, pp. 791-791, Dec. 2006.

[43] P. Lalanne and J. P. Hugonin, "Interaction between optical nano-objects at metallo-dielectric interfaces," *Nature Physics*, vol. 2, no. 8, pp. 551-556, 2006.

[44] L. Chen, J. T. Robinson, and M. Lipson, "Role of radiation and surface plasmon polaritons in the optical interactions between a nano-slit and a nano-groove on a metal surface," *Optics Express*, vol. 14, no. 26, pp. 12629-12636, Dec. 2006.

[45] W. L. Barnes, W. A. Murray, J. Dintinger, E. Devaux, and T. W. Ebbesen, "Surface Plasmon Polaritons and Their Role in the Enhanced Transmission of Light through Periodic Arrays of Subwavelength Holes in a Metal Film," *Physical Review Letters*, vol. 92, no. 10, p. 107401, Mar. 2004.

[46] E. Devaux, T. W. Ebbesen, J. Weeber, and A. Dereux, "Launching and decoupling surface plasmons via micro-gratings," *Applied Physics Letters*, vol. 83, no. 24, p. 4936, 2003.

[47] J. A. Porto, F. J. Garcia-Vidal, and J. B. Pendry, "Transmission Resonances on Metallic Gratings with Very Narrow Slits," *Physical Review Letters*, vol. 83, no. 14, p. 2845, Oct. 1999.

[48] Q. Cao and P. Lalanne, "Negative Role of Surface Plasmons in the Transmission of Metallic Gratings with Very Narrow Slits," *Physical Review Letters*, vol. 88, no. 5, p. 057403, Jan. 2002.

[49] F. J. Garcia-Vidal, L. Martín-Moreno, and J. B. Pendry, "Surfaces with holes in them: new plasmonic metamaterials," *Journal of Optics A: Pure and Applied Optics*, vol. 7, no. 2, pp. S97-S101, Feb. 2005.

[50] J. B. Pendry, L. Martin-Moreno, and F. J. Garcia-Vidal, "Mimicking Surface Plasmons with Structured Surfaces," *Science*, vol. 305, no. 5685, pp. 847-848, Aug. 2004.

[51] L. Salomon, F. Grillot, A. V. Zayats, and F. de Fornel, "Near-Field Distribution of Optical Transmission of Periodic Subwavelength Holes in a Metal Film," *Physical Review Letters*, vol. 86, no. 6, p. 1110, Feb. 2001.

[52] S. Chang, S. Gray, and G. Schatz, "Surface plasmon generation and light transmission by isolated nanoholes and arrays of nanoholes in thin metal films," *Optics Express*, vol. 13, no. 8, pp. 3150-3165, Apr. 2005.

[53] P. D. Flammer, I. C. Schick, R. T. Collins, and R. E. Hollingsworth, "Interference and resonant cavity effects explain enhanced transmission throughsubwavelength apertures in thin metal films," *Optics Express*, vol. 15, no. 13, pp. 7984-7993, Jun. 2007.

[54] P. D. Flammer et al., "Theoretical study of enhanced transmission through subwavelength linear apertures flanked by periodic corrugations," in *Proceedings of SPIE*, vol. 6323, pp. 63231Z-10, 2006.

[55] J. D. Joannopoulos and J. N. Winn, *Photonic crystals: molding the flow of light*, 2nd ed. New Jersey: Princeton University Press, 2008.

[56] K. Fong and P. M. Hui, "Coupling of waveguide and surface modes in enhanced transmission through stacking gratings," *Applied Physics Letters*, vol. 89, no. 9, pp. 091101-3, 2006.

[57] H. B. Chan et al., "Optical transmission through double-layer metallic subwavelength slit arrays," *Optics Letters*, vol. 31, no. 4, pp. 516-518, Feb. 2006.

[58] A. Estroff, Y. Fan, A. Bourov, and B. Smith, "Mask-induced polarization effects at high numerical aperture," *Journal of Microlithography, Microfabrication, and Microsystems*, vol. 4, no. 3, p. 031107, 2005.

[59] J. W. Goodman, *Introduction to Fourier Optics*, 3rd ed. Englewood, CO: Roberts & Company, 2005.

[60] *See for example GSOLVER*. Grating Solver Development Company, Inc., 2010.

[61] T. V. Pistor, *EM-Suite*. Panoramic Technology, Inc., 2007.

[62] *FDTD Solutions*. Lumerical Solutions, Inc.

[63] *See for example COMSOL Multiphysics*. COMSOL, 2010.

[64] *JCMsuite*. JCMwave Corporation.

[65] "FDTD Solutions Online Help," *Lumerical*, 15-Jul-2010. [Online]. Available: http://www.lumerical.com/fdtd_online_help/fdtd_online_help_summary.php.

[66] A. Taflove and S. C. Hagness, *Computational Electrodynamics: The Finite-Difference Time-Domain Method*, 3rd ed. Norwood, MA: Artech House Publishers, 2005.

[67] T. V. Pistor, "Electromagnetic Simulation and Modeling with Applications in Lithography," Ph.D. Thesis, University of California at Berkeley, 2001.

[68] K. S. Yee, "Numerical solution of initial boundary value problems involving maxwell's equations in isotropic media," *Antennas and Propagation, IEEE Transactions on*, vol. 14, no. 3, pp. 302-307, 1966.

[69] D. Flagello, B. Geh, S. Hansen, and M. Totzeck, "Polarization effects associated with hyper-numerical-aperture (>1) lithography," *Journal of Microlithography, Microfabrication, and Microsystems*, vol. 4, no. 3, p. 031104, 2005.

[70] H. A. Macleod, *Thin-Film Optical Filters*, American ed. New York: American Elsevier Pub. Co, 1969.

[71] D. G. Flagello, T. Milster, and A. E. Rosenbluth, "Theory of high-NA imaging in homogeneous thin films," *Journal of the Optical Society of America A*, vol. 13, no. 1, pp. 53-64, Jan. 1996.

[72] Y. Fan, "Pushing the Limits of Hyper-NA Optical Lithography," Ph.D. Thesis, Rochester Institute of Technology, 2005.

[73] B. W. Smith, Y. Fan, J. Zhou, N. V. Lafferty, and A. Estroff, "Evanescent wave imaging in optical lithography," in *Proceedings of SPIE*, vol. 6154, pp. 61540A-61540A-9, 2006.

[74] B. W. Smith, L. V. Zavyalova, and A. Estroff, "Benefiting from polarization effects on high-NA imaging," in *Proceedings of SPIE*, vol. 5377, pp. 68-79, 2004.

[75] "Optical Properties of Thin Films," *RIT Nanolithography Research Labs*. [Online]. Available: http://www.rit.edu/lithography/thinfilms/thinfilms/thinfilms.html.

[76] M. Yoshizawa, V. Philipsen, and L. H. A. Leunissen, "Impact of the absorber thickness variation on the imaging performance of ArF immersion lithography," in *Proceedings of SPIE*, vol. 5853, pp. 243-251, 2005.

[77] *PROLITH*. KLA Tencor, 2008.

[78] SMFL, "Tempress Dicing Saw," *SMFL Wiki*, 29-Jul-2010. [Online]. Available: http://wiki.smfl.rit.edu/index.php/Tempress_Dicing_Saw. [Accessed: 29-Jul-2010].

[79] SMFL, "RCA Clean," *SMFL Wiki*, 29-Jul-2010. [Online]. Available: http://wiki.smfl.rit.edu/index.php/Definitions#RCA_Clean. [Accessed: 29-Jul-2010].

[80] P. Van Zant, "RCA Clean," in *Microchip Fabrication*, 3rd ed., New York: McGraw-Hill, 1997, pp. 176-177.

[81] SMFL, "PE4410," *SMFL Wiki*, 29-Jul-2010. [Online]. Available: http://wiki.smfl.rit.edu/index.php/PE4400_Sputter. [Accessed: 29-Jul-2010].

[82] M. Ohring, *The Materials Science of Thin Films*. San Diego: Academic Press, 1992.

[83] P. Van Zant, "Reactive Ion Etching," in *Microchip Fabrication*, 3rd ed., New York: McGraw-Hill, 1997, pp. 272-273.

[84] SMFL, "LAM 4600 Al Etcher," *SMFL Wiki*, 29-Jul-2010. [Online]. Available: http://wiki.smfl.rit.edu/index.php/LAM_4600_Al_Etcher. [Accessed: 29-Jul-2010].

[85] SMFL, "Trion Minilock RIE," *SMFL Wiki*, 29-Jul-2010. [Online]. Available: http://wiki.smfl.rit.edu/index.php/Trion_Etcher. [Accessed: 29-Jul-2010].

[86] J. Zhou, "Hyper-NA Imaging in Optical Lithography at Oblique Angles," Ph.D. Thesis, Rochester Institute of Technology, 2008.

[87] M. Trikeriotis et al., "Development of an inorganic photoresist for DUV, EUV, and electron beam imaging," in *Proceedings of SPIE*, vol. 7639, pp. 76390E-10, 2010.

[88] E. C. Piscani, D. Ashworth, J. Byers, C. Van Peski, P. Zimmerman, and B. J. Rice, "Continuing 193nm optical lithography for 32nm imaging and beyond," in *Proceedings of SPIE*, vol. 6924, pp. 69242I-12, 2008.

[89] A. Bourov et al., "Immersion microlithography at 193 nm with a Talbot prism interferometer," in *Proceedings of SPIE*, vol. 5377, pp. 1573-1578, 2004.

[90] SMFL, "CHA Flash Evaporator," *SMFL Wiki*, 29-Jul-2010. [Online]. Available: http://wiki.smfl.rit.edu/index.php/CHA_Flash_Evaporator. [Accessed: 29-Jul-2010].

[91] A. J. van Roosmalen, J. A. G. Baggerman, and S. J. H. Brader, *Dry etching for VLSI*. New York: Springer, 1991.

[92] A. D. Raisanen, "Private Communication," 13-Sep-2009.

[93] J. Zhou, Y. Fan, A. Bourov, and B. W. Smith, "Inorganic immersion fluids for ultrahigh numerical aperture 193 nm lithography," *Applied Optics*, vol. 45, no. 13, pp. 3077-3082, May. 2006.

[94] L. Zavyalova, "Composite Films Modeling," *RIT Nanolithography Research Labs*. [Online]. Available: http://www.rit.edu/kgcoe/microsystems/lithography/thinfilms/cgi-bin/composite.html.

[95] H. Du et al., "Optical properties of ultrathin aluminum films deposited by magnetron sputtering in visible band," *Optical Materials*, vol. 28, no. 8, pp. 944-949, Jun. 2006.

[96] W. Rasband, *ImageJ*. USA: National Institutes of Health, 2010.

[97] M. L. Boas, "Fourier Series," in *Mathematical Methods in the Physical Sciences*, 2nd ed., New York: John Wiley & Sons, 1983, pp. 297-335.

[98] M. Born and E. Wolf, *Principles of Optics: Electromagnetic Theory of Propagation, Interference and Diffraction of Light*, 7th ed. Cambridge University Press, 1999.